DISCLAIMER:

This document does not meet the
current format guidelines of
the Graduate School at
The University of Texas at Austin.

It has been published for
informational use only.

The Dissertation Committee for Ellen Brooke Le
certifies that this is the approved version of the following dissertation:

Data-Driven Reduction Strategies for Bayesian Inverse Problems

Committee:

Tan Bui-Thanh, Co-Supervisor

Quoc P. Nguyen, Co-Supervisor

Omar Ghattas

J. Tinsley Oden

Rachel Ward

Data-Driven Reduction Strategies for Bayesian Inverse Problems

by

Ellen Brooke Le

DISSERTATION

Presented to the Faculty of the Graduate School of

The University of Texas at Austin

in Partial Fulfillment

of the Requirements

for the Degree of

DOCTOR OF PHILOSOPHY

THE UNIVERSITY OF TEXAS AT AUSTIN

May 2018

To Benj

What the mind doesn't understand,
it worships or fears.
Alice Walker

I can see that without being excited,
mathematics can look pointless and cold.
Maryam Mirzakhani, *1977-2017*

Free will, though it makes evil possible, also makes
possible any love or goodness or joy worth having.
C.S. Lewis

Acknowledgments

I am extremely grateful to my ICES supervisor Tan Bui-Thanh, for his support, sharp scientific guidance, and the monumental effort he put into training me since my first year at UT. Under Tan's direction I have grown spiritually and intellectually, far more than I imagined I would during five years (—did I even learn anything in undergrad?). With each year of this PhD, I felt exponentially greater depth of understanding and confidence in my capacity to do creative, valuable work—and if only because, while reading old material or code I had written the previous year, I'd think something like, 'well, this is not technically wrong, but I really had no idea! [to the degree that I have *some* idea now]'. It is a blessing to have this feeling. I am grateful that Tan kept high standards and never gave up on me. I am also grateful to have Tan not only as an academic role model, but as a personal one. People who don't know him might wrongly perceive him as a singularly-minded workaholic researcher, who must be making trade-offs somewhere else in life, but they do not realize that he is an excellent and caring instructor, a devoted husband and father, a talented gardener and karaoke singer, and can do more pull-ups than our entire research group combined (sadly). His achievements are a testament to approaching all of life with energy, conscientiousness, and passion.

I am also indebted to my PGE co-advisor Quoc P. Nguyen for his support, patience, and generosity, and for bringing me up to speed quickly in the world of petroleum and subsurface transport, which was a completely new domain for me. Going on the job market this past year was not easy, but I strongly believe that being able to discuss real world inverse problems in depth, in addition to research, made my application stand out—and for this I am grateful to Dr. Nguyen. Both my advisors were instrumental in providing my uncommon graduate school experience—how many people can say they went to Europe, Australia, and

Canada for the first time during their PhD, to present their research? I recognize this is unusual, and thank both for their generosity and trust in my presentation skills.

I wish to express gratitude to my committee, for the content and shape of this dissertation. With their assistance it has become something I can be proud of. I thank especially Professor J. Tinsley Oden, the person most responsible for developing ICES into the dream team of computational scientists that it is today—the veritable "New York Yankees of researchers," as Benj likes to say. At the time of writing, ICES is the number one ranked program in the world, thanks to Prof. Oden's remarkable direction and pioneering vision. I have already benefited so much from Prof. Oden's work, so I am humbled, honored, and slightly embarrassed by the fact that he read my thesis word for word with a highlighter and managed to find errors that many (smart!) people and passes could not. I acknowledge deep gratitude for his time and dedication to excellence.

I am grateful to my committee members Omar Ghattas and Rachel Ward, who are both superstars in their fields, for taking the time to really understand the methods here, in order to offer their unparalleled insights that shaped the final dissertation for the better. Thank you.

Many thanks to my collaborators: Aaron Myers, Dan O'Malley, Monty Vesselinov, Youzou Lin, and Vishwas Rao, for support, helping me to develop ideas, allowing me to experience the storied lab life at Los Alamos, and to have fun while doing research. Regarding Los Alamos, I thank Dr. Bill Press for turning me into a Bayesian for life, and helping me find last minute housing both for me and my cat. I am grateful to ICES for the generous CSEM Fellowship and TACC for the computing resources and timely help. I thank SIAM, AAAS, and the Sac Bee editors for my summer at the newsdesk, which I did not realize would help so much with writing this dissertation. Heartfelt thanks to my cohort and mentors from EDGE 2011, especially Ami Radunskaya (Dr. Rad) and Rhonda Hughes, for showing that you can be a world-class mathematician and still a genuine heart-on-your-sleeve person who

believes in everyone. You don't know how much strength and inspiration you all gave me! I reach back to that summer so much when I feel like quitting, which has been often. Dr. Caitlin McClune of the University Writing Center has been especially vital in craziness of my final writing days—thank you. I am indebted to the PCL library staff for the silent study where I wrote the majority of this dissertation.

For nourishing my humanity during these past few months of self-imposed isolation in a windowless room, I am lucky to have amazing friends and family. They managed to reach me with everything from texts of motivating gifs to actual gifts (what!). Thank you to my mother and father for overcoming so much, teaching me to love math, and now for the continual reminders to eat vegetables and just be happy. Thank you to my first role model, Maj. Viet Le, for helping me to believe that greatness is in my blood, and trying your best to get me to be good at sports. It made school easier. I thank my dear, accomplished sister Emily Le, my life coach—no doubt I got through many tough times with her tough no-nonsense talk!

I could have never made it without the support from my sweet, intelligent, and wonderful friends for life: Dee Dee White, Hannah Frederick, Jessica Le, Isabelle Atkinson, Sarah Parker, Stacey Burke, Madelyn DeYoung—you guys will actually change the world. I look up to you! Lastly I thank my fiance Benj Wagman, to whom this this thesis is dedicated, for being there one hundred and ten percent for me, throughout all the ups and downs of the past five years, and being the only person to laugh at my jokes. Over the past few months, you have sweetly accepted my descent into madness, and selflessly offered all the support one can offer, even though you have had your own dissertation to contend with. A PhD does not guarantee a good career or life, but it is an important step for both of us. I am grateful for your trust, and feel nothing other than happiness to have you with me on this uncertain journey. I look forward to spending more time with you.

Data-Driven Reduction Strategies for Bayesian Inverse Problems

Publication No. _____

Ellen Brooke Le, Ph.D.
The University of Texas at Austin, 2018

Co-Supervisors: Tan Bui-Thanh
Quoc P. Nguyen

A persistent central challenge in computational science and engineering (CSE), with both national and global security implications, is the efficient solution of large-scale Bayesian inverse problems. These problems range from estimating material parameters in subsurface simulations to estimating phenomenological parameters in climate models. Despite recent progress, our ability to quantify uncertainties and solve large-scale inverse problems lags well behind our ability to develop the governing forward simulations.

Inverse problems present unique computational challenges that are only magnified as we include larger observational data sets and demand higher-resolution parameter estimates. Even with the current state-of-the-art, solving deterministic large-scale inverse problems is prohibitively expensive. Large-scale uncertainty quantification (UQ), cast in the Bayesian inversion framework, is thus rendered intractable. To conquer these challenges, new methods that target the root causes of computational complexity are needed.

In this dissertation, we propose data-driven strategies for overcoming this "curse of dimensionality." First, we address the computational complexity induced in large-scale inverse problems by high-dimensional observational data. We propose a randomized misfit approach

(RMA), which uses random projections—quasi-orthogonal, information-preserving transformations—to map the high-dimensional data-misfit vector to a low-dimensional space. We provide the first theoretical explanation for why randomized misfit methods are successful in practice with a small reduced data-misfit dimension ($n = \mathcal{O}(1)$).

Next, we develop the randomized geostatistical approach (RGA) for Bayesian subsurface inverse problems with high-dimensional data. We show that the RGA is able to resolve transient groundwater inverse problems with noisy observed data dimensions up to 10^7, whereas a comparison method fails due to out-of-memory errors.

Finally, we address the solution of Bayesian inverse problems with spatially localized data. The motivation is CSE applications that would gain from high-fidelity estimation over a smaller data-local domain, versus expensive and uncertain estimation over the full simulation domain. We propose several truncated domain inversion methods using domain decomposition theory to build model-informed artificial boundary conditions. Numerical investigations of MAP estimation and sampling demonstrate improved fidelity and fewer partial differential equation (PDE) solves with our truncated methods.

Table of Contents

Chapter 1

Introduction

This dissertation proposes new data-driven methods towards making state-of-the-art Bayesian inversion and uncertainty quantification (UQ) tractable for large-scale problems: problems of data assimilation and statistical inference, governed by computationally expensive PDE-based models and high-dimensional input parameters. Here, high-dimensional means the dimension is in the hundreds, thousands, or millions. The high dimensionality is typically due to discretization of a spatially distributed heterogeneous parameter in a two- or three-(space)-dimensional model. Computationally expensive means that a single forward simulation takes hours or days to finish, even when optimized for distributed computing on leadership-class supercomputers.

Important large-scale inverse problems exist in numerous different areas of computational science and engineering (CSE). As just *a few* examples of active areas of research, these include:

- Ice sheet modeling: Estimating the phenomenological basal sliding parameter in Antarctic ice sheet models, using remote sensing observations of surface ice flow.
- Bioremediation: Estimating the future spatial distribution of the full chromium plume endangering the Los Alamos, New Mexico water table, using concentration and production data from current localized mitigation efforts at wells.
- Energy independence: Estimating the current spatial distribution of residual oil in a mature West Texas reservoir, using production history data and concentration history

from a partitioning interwell tracer test. This information is critical for thorough risk-assessment of expensive (upwards of several million USD [133]) enhanced oil recovery projects.

- Earth system modeling: Estimating the climate response to regional and cloud-scale input parameters, to advance development of exascale-ready high-resolution simulations of clouds in climate models. This could reduce the largest source of uncertainty in predictions of future climate.

The methods proposed in this dissertation are designed to apply to all of the inverse problems above, as well as others. Fortunately, these different problems possess similar mathematical challenges. They are ill-posed, and governed by computationally expensive-to-solve partial differential equation (PDE) models, heterogeneous high-dimensional parameters, and increasingly, large amounts of observational data.

1.1 Needs and challenges in solving large-scale Bayesian inverse problems

Despite remarkable advancements in the past two decades, current methods for solving Bayesian inverse problems are limited to problems of modest computational complexity and input parameter dimension [2, 4, 25, 59, 124]. Standard Bayesian inversion methods such as Markov Chain Monte Carlo (MCMC) require hundreds of thousands or millions of simulations to converge. Thus, they are prohibitive for large-scale models.

Solving the Bayesian inverse problem is a straightforward approach to uncertainty quantification. The uncertainty in the unknown input parameters is completely described by the posterior probability—the solution of the Bayesian inverse problem. The uncertainty in predictions and quantities of interest is then quantified by propagating the posterior input parameter statistics through the forward model. The difficulty is the acute compu-

tational complexity of solving the Bayesian inverse problems with large-scale models and high-dimensional parameter spaces.

Yet, the need to quantify and reduce the uncertainty in our computational models is urgent. Scientists and policy-makers across the spectrum agree increasingly that predictions must be equipped with quantified uncertainty in order to be of pragmatic, actionable use for decision-makers and CSE stakeholders. For example, despite the recent change in administration, the term "uncertainty" five times in the FY 2018 U.S. Department of Energy (DOE) Budget Request brief—the same number of times that it appeared in the FY 2017 brief (compare this to only one appearance in the FY 2016 brief).

1.1.1 Existing strategies and limitations

Several approaches exist for addressing the computational challenge posed by the large-scale Bayesian inverse problems of interest. The approaches are not necessarily separate, and include:

- Attack the forward solve (simulation) computational cost: Make PDE solvers faster or develop cheaper surrogate models.
- Attack the Bayesian UQ method: Develop viable alternative sampling approaches to standard approaches. Standard vanilla MCMC, Latin Hypercube Sampling (LHS), and polynomial chaos expansion-based sampling are not viable for the large-scale inverse problems of interest due to the computational cost required for convergence to the posterior probability [20, 100]. Or, develop methods to accelerate MCMC convergence while minimizing the number of model evaluations [38].
- Use intrusive or embedded UQ methods: The majority of available UQ tools treat the parameter-to-observable map as a black box. Intrusive or embedded UQ methods, on the other hand, require access to gradients of the underlying forward operator,

motivated by the fact that the output of PDE models is locally smooth. Recently developed intrusive methods exploit the mathematical properties of the parameter-to-observable operator and have been successfully applied to inverse UQ problems with parameter dimensions in the millions [25, 65].

- Develop targeted reduction strategies: Identify mathematical structure components that have the largest impact on the computational cost estimate for solving the Bayesian inverse problem and replace them with goal-oriented, reduced order *components*—this category includes reduced order modeling approaches, but is broader.

The method development approach in this dissertation is best characterized by the last bullet point.

1.1.2 Motivation for developing data-driven reduction strategies

Only compounding difficulties is the demand to resolve Bayesian inverse problems with larger discretized state, parameter, and data dimensions. This is in part due to the big data challenge that is rapidly changing the field of computational science and engineering (CSE), as result of improved measurement technology and ability to store large volumes of data [124]. Thus, another emerging challenge in computational science and engineering is the solution of large-scale statistical inverse problems governed by PDEs that involve large amounts of observational data. Alternatively, although the data may be high-dimensional, it is often still located in and informative for a spatially-concentrated subregion of the full model domain. The data-informed subregion is a lower-dimensional subset of the high-dimensional parameter and state spaces. New inversion methods that target and exploit these emerging data paradigms are needed.

1.2 Dissertation goal

The goal of Bayesian inverse problems is to infer knowledge from data. Progress towards this goal in many large-scale problems is impeded by the computational challenges outlined in section 1.1. Despite the promise of big data and technological advances in data collection and measurement, computational challenges persist, and new strategies are needed [124]. The goal of this dissertation is to develop new, data-driven strategies for efficiently and effectively solving large-scale Bayesian inverse problems—and therefore make the extraction of knowledge from data both timely and tractable.

1.3 Dissertation contributions

The main contributions of this dissertation towards the above stated goal are a method for reducing the computational impact of big data, and a method for reducing the complexity induced by high-dimensional parameter and state spaces in problems with spatially local data. Both reduction strategies are theoretically justified, using large deviation theory and domain decomposition theory, respectively.

Specifically, a theoretical contribution of this dissertation is the first guarantee of validity for the deterministic solution obtained with a randomized misfit, with a small reduced dimension. This provides an explanation for the observed surprising quality of solutions when using a randomized misfit function with a small reduced dimension, which has been noted in other randomized misfit methods. The efficacy of the randomized misfit approach in this dissertation is shown to be the result of the interplay between Morozov's discrepancy principle and random projection theory. As will be shown, the data error and ill-posedness inherent in inverse problems is essential to the success of random projections.

This key contribution is due to the use of large deviation theory to arrive at a practical, statistical characterization of solution convergence. Large deviation techniques form the

basis of random projection theory and analysis of other effective randomized dimension reduction algorithms (e.g. randomized SVD). Here, it is used to show the RMA exploits a "concentration of measure" phenomenon for high-dimensional data. It is shown that for a certain class of distributions, the tail probability of a sample average of misfit estimators decays exponentially, with a rate parameterized by the sample size. This statement is turned into a probabilistic bound on the randomized cost for a fixed data misfit dimension .

Another novel contribution of the approach presented in this dissertation is that it permits the use of many random projections in the literature.

Additionally, from the stochastic formulation of the misfit, a different version of the Johnson-Lindenstrauss embedding theorem [42, 64, 96] is shown. This leads to an insight into why the reduced misfit dimension n is $\mathcal{O}(\varepsilon^{-2})$, where ε is the relative error of the randomized cost function.

The dissertation also demonstrates and shows comparable results for a practical RMA extension to geoscience inverse problems with big geostatistical data [88], called the randomized geostatistical approach (RGA). It extends the widely used Bayesian geostatistical approach (GA) [74], and its extension called the principal component geostatistical approach (PCGA) [73, 84].

The GA is known to be limited to only moderate size problems [73, 84]. Although the PCGA, a randomized approximation of the GA, extends the GA to solve problems with problems with high-dimensional parameter spaces ($\mathcal{O}(10^5) - \mathcal{O}(10^7)$), it is limited to *moderate* data dimensions (($\mathcal{O}(10^4)$) [73, 84]. The RGA extends the GA to inverse problems with problems with high-dimensional ($\mathcal{O}(10^5) - \mathcal{O}(10^7)$) parameter spaces *and* high-dimensional data. The analysis and results presented in this dissertation demonstrate comparable parameter estimation and convergence results as the PCGA in a groundwater inverse problem. However the RGA experiments show a 31 times speed-up. Numerical results in this dissertation also show the RGA is able to solve geostatistical inverse problems with up to observed

data dimensions of up to $\mathcal{O}(10^7)$, whereas PCGA fails due to insufficient memory.

This dissertation also contributes the development of several truncated domain inversion strategies and methods. These methods directly reduce the problematic high-dimensionality of the parameter and state domain by shrinking the model domain, and only inverting for an informed subregion of the model. They exploit an insight that observed data, which is often located in a smaller region than the full model domain, is spatially-limited in parameter information. Using the uncertainty estimation at the maximum a posteriori (MAP) point, and building on domain-decomposition methods and work that uses Dirchlet-to-Neumann (DtN) maps to build mathematically-justified artificial boundary conditions, different model-constrained and low-offline-cost methods are investigated. Results with a distributed thermal conductivity inverse problem demonstrate that truncated inversion can be more efficient and effective. An idea is supported with results from both MAP estimation and sampling experiments, that fidelity in MAP point estimation results could be improved and the posterior can be easier to characterize, by removing high uncertainty regions from the inversion domain. That is, the strategy is effective not only because it reduces high-dimensional state and parameter space, but also because it fundamentally changes the full domain posterior and problem. Given the same amount of computational resources, this means more distributed parameter information can be extracted from the observed data, and therefore fulfills the dissertation goal towards making large-scale Bayesian inversion timely and tractable.

1.4 Dissertation outline

The following chapters develop different reduction strategies for reducing the complexity of solving large-scale Bayesian inverse problems.

The strategies are driven by properties of the data in the problems of interest.

Specifically, each method exploits one of two data paradigms that are commonly observed in the large-scale setting: either the data is high-dimensional, or the data is located in a smaller subregion relative to the full model domain, and contains spatially-limited information about the unknown distributed parameter.

Chapter 3 introduces the randomized misfit approach (RMA) a targeted application of a machine learning tool called a random projection, to reduce the high computational cost of solving big data, high-fidelity physics-based inverse and its analysis. Section 3.6 presents the theoretical analysis for the randomized misfit approach by deriving the large deviation bounds on the objective function error for a broad class of distributions. The reduced misfit dimension is shown to be independent of the original data dimension. This derivation leads to a different proof of a variant of the celebrated Johnson-Lindenstrauss embedding theorem. A statistical Morozov's discrepancy principle, Theorem 2 shows that the effective reduced misfit dimension is also bounded below by the noise in the problem. Therefore, the RMA solution is a guaranteed solution for the original problem with a high user-defined probability. The reduced computational cost in problems with high-dimensional data is assessed in subsection 3.6.3. Section 3.7 summarizes numerical experiments on a model inverse heat conduction problem in one-, two-, and three spatial-dimensions. The RMA solution with different distributions is compared to the solution of the full problem. Numerical support for Theorem 2 is also investigated.

Chapter 4 introduces and motivates the RGA, first briefly introducing the Bayesian geostatistical approach (GA) [74], a widely used geostatistical inversion method, and its extension to large-scale problems with high-dimensional parameter spaces [84] called the principal component geostatistical approach (PCGA) [84].

In section 4.6, it is shown that the RGA can be more effective than the PCGA method when the number of observations is large. In section 4.7, numerical tests of the RGA against PCGA with a big data transient groundwater inverse problem are given.

Chapter 5 examines domain-decomposition methods for large-scale inverse problems, and both model constrained and low-offline cost methods are developed. Numerical results demonstrate higher-fidelity inversion and UQ results with improved computational efficiency by truncating the problem domain.

Chapter 6 briefly discusses ongoing extensions of the methods presented in Chapters 3 to 5. Concluding remarks are also provided to guide future research.

Chapter 2

Inverse problem formulation

This dissertation develops methods towards the efficient solution of large-scale Bayesian inverse problems, which are briefly overviewed in Chapter 1, along with current challenges and existing strategies. The aim of this preliminary chapter is to introduce the mathematical formulation for the abstract Bayesian inverse problem of interest, and thus make the objectives of the dissertation methods concrete. The general notation will remain the same throughout this dissertation, with only a few necessary modifications for different methods and applications. This chapter also introduces a nonlinear inverse problem, the estimation of a distributed coefficient in a linear elliptic PDE. This model problem is the basis for each of the driving examples presented in this dissertation, with method-specific extensions.

2.1 The objective of the inverse problem

The main goal of an *inverse problem* is to infer an unknown input *parameter* $\mathbf{u}$ using indirect observed data $\mathbf{d}$. The parameter cannot by observed directly, for reasons that vary and depend on the application. In PDE-constrained inverse problems, a system of PDEs governs the relationship between the unknown $\mathbf{u}$ and observed noisy $\mathbf{d}$.

The methods developed in this dissertation address computationally prohibitive-to-solve inverse problems—specifically, problems that are large-scale and have spatially-distributed unknown parameters, which are high-dimensional when discretized. Here, large-scale means that a single forward solve can take minutes to hours, even on supercomputers.

Assuming a common Gaussian additive noise model for the observed data:

$$d_j = \mathbf{w}\left(\mathbf{x}_j; \mathbf{u}\right) + \eta_j, \quad j = 1, \ldots, N, \tag{2.1}$$

the inverse problem objective is to reconstruct the distributed parameter $\mathbf{u}$ given N data points d_j. For a given $\mathbf{u}$, a set of discretized states $\mathbf{w}\left(\mathbf{x}_j; \mathbf{u}\right)$ is obtained by evaluating an expensive-to-solve forward model (generally a system of PDEs), and then applying a linear observation operator to match the data locations. The location of an observational data point in an open and bounded spatial domain Ω is denoted by $\mathbf{x}_j$, and η_j is Gaussian random noise with mean 0 and variance σ^2_{noise}.

Concatenating the observations, (2.1) can be rewritten as

$$\mathbf{d} = \mathbf{F}(\mathbf{u}) + \boldsymbol{\eta}, \quad \boldsymbol{\eta} \sim \mathcal{N}(0, \boldsymbol{\Gamma}_{\text{noise}}) \tag{2.2}$$

where

$$\boldsymbol{\Gamma}_{\text{noise}} := \sigma^2_{\text{noise}} \mathbf{I}_N \tag{2.3}$$

and $\mathbf{F}\left(\mathbf{u}\right) := \left[\mathbf{w}\left(\mathbf{x}_1; \mathbf{u}\right), \ldots, \mathbf{w}\left(\mathbf{x}_N; \mathbf{u}\right)\right]^\top$ is the parameter-to-observable map. Thus the model forward problem is to solve (2.4) for the unknown distributed temperature $\mathbf{u}$, given a known distributed log conductivity $\mathbf{u}$.

The model inverse problem is to reconstruct the distributed log conductivity $\mathbf{u}$, given noisy observed measurements $\mathbf{d}$ of temperature $\mathbf{w}$ on Ω.

The parameter-to-observable map $\mathbf{F}(\mathbf{u})$ encodes a single, computationally-expensive solve of the forward model, represented by (2.4) in the given model inverse problem, followed by extraction to the data locations. It is generally a nonlinear map, even when the PDE system is linear in the state [25], as will be the case with the model forward PDE (2.4) used throughout this dissertation.

2.2 Forward model

In formulating an inverse problem, the *forward problem* is the well-posed problem of obtaining the state $\mathbf{w}$ (the *forward solution*), given a parameter $\mathbf{u}$.

The forward problem is governed by the *forward (physics) model* which is generally a system of PDEs.

2.2.1 Model problem: Elliptic forward PDE

The model problem for initial development and testing of methods in this dissertation is the estimation of a distributed coefficient in an elliptic partial differential equation. This Poisson-type problem arises in various inverse applications, such as the steady-state thermal conductivity or groundwater problem, or in finding a membrane with a given spatially-varying stiffness.

For concreteness, consider the forward heat conduction problem on an open bounded domain Ω, governed by

$$\begin{aligned} -\nabla \cdot (e^{\mathbf{u}} \nabla \mathbf{w}) &= f(\mathbf{u}) && \text{in } \Omega \\ -e^{\mathbf{u}} \nabla \mathbf{w} \cdot \mathbf{n} &= \mathrm{Bi}\, \mathbf{w} && \text{on } \partial\Omega^{\mathrm{Bi}} \\ -e^{\mathbf{u}} \nabla \mathbf{w} \cdot \mathbf{n} &= -1 && \text{on } \partial\Omega^{\mathrm{RHS}} \end{aligned} \tag{2.4}$$

where the forward state $\mathbf{w}$ is the spatially distributed temperature on Ω, the material coefficient $\mathbf{u}$ is the logarithm of distributed thermal conductivity on Ω, $\mathbf{n}$ is the unit outward normal on $\partial\Omega = \partial\Omega^{\mathrm{Bi}} \cup \partial\Omega^{\mathrm{RHS}}$, and Bi is the Biot number. The model domain is $\Omega \in \mathbb{R}^n, n = 2, 3$. Here, $\partial\Omega^{\mathrm{RHS}}$ is a portion of the boundary $\partial\Omega$ on which the inflow heat flux is 1. The rest of the boundary, $\partial\Omega^{\mathrm{Bi}}$, is assumed to have Robin boundary condition.

Thus the model forward problem is to solve (2.4) for the unknown distributed temperature $\mathbf{u}$, given a known distributed log conductivity $\mathbf{u}$.

The model inverse problem is to reconstruct the distributed log conductivity $\mathbf{u}$, given noisy observed measurements $\mathbf{d}$ of temperature $\mathbf{w}$ on Ω.

2.3 The deterministic inverse problem

The *deterministic inverse problem* governed by (2.4) is the problem of estimating a *single* unknown log conductivity parameter $\mathbf{u}$ that could have led to the data $\mathbf{d}$.

Unlike the well-posed forward problem, the inverse problem is generally ill-posed; many different spatially-varying log conductivities $\mathbf{u}$ fit the observed data equally well. An intuitive reason is that discrete observations can only contain limited information about an infinite-dimensional parameter. The more complete explanation is that the parameter-to-observable map exhibits rapid spectral decay. This can be numerically observed and has been proven for many practical inverse problems [18, 19, 21].

Therefore, to overcome ill-posedness and solve the deterministic problem, classical inverse problem approaches add a regularization term to the cost functional . The regularization can be thought of as adding additional criteria to the original data-misfit minimization problem, in order to single out one "best" estimate of $\mathbf{u}$.

A standard deterministic Tikhonov approach resolves the ill-conditioning by adding a quadratic term to the cost function, so that the problem may now be formulated as

$$\min_{\mathbf{u}} \mathcal{J}(\mathbf{u}) = \frac{1}{2}\|\mathbf{F}(\mathbf{u}) - \mathbf{d}\|^2_{\mathbf{\Gamma}^{-1}_{\text{noise}}} + \frac{1}{2}\|\mathbf{u} - \mathbf{u}_0\|^2_{\mathbf{C}^{-1}}. \tag{2.5}$$

where $\mathbf{v} = \mathbf{\Gamma}^{\frac{1}{2}}_{\text{noise}}(\mathbf{d} - \mathbf{F}(\mathbf{u}))$ is the (noise-weighted) *data misfit vector*, Euclidean norm in $\mathbb{R}^N$ is denoted by $\|\cdot\|$, and $||\cdot||_{\mathbf{C}^{-1}} = \left|\left|\mathbf{C}^{\frac{1}{2}}\cdot\right|\right|$ is the norm weighted by an appropriately chosen regularization matrix $\mathbf{C}$.

2.4 The Bayesian statistical inverse problem

In this dissertation adopts the framework of the *Bayesian inverse problem*, which seeks a statistical description of all probable parameter fields $\mathbf{u}$ consistent with the observations, rather than a single best $\mathbf{u}$.

That is, the solution of the Bayesian inverse problem is the posterior probability distribution function (pdf) of the unknown parameter, given the observed data.

It requires specification of a likelihood model, which characterizes the probability that the parameter $\mathbf{u}$ could have produced the observed data $\mathbf{d}$. It also requires a prior model, which is problem-dependent and represents a subjective belief regarding the distribution of $\mathbf{u}$.

There are other reasons to prefer a Bayesian approach, in addition to obtaining a distribution of probable $\mathbf{u}$ that could have led to the data One reason is that Bayesian inversion is a systematic yet flexible, and naturally well-posed framework for integrating sources of parameter information from observational data, physics-information (encoded in the model), and the subjective judgment of domain experts (encoded in the prior). To paraphrase succinctly, Bayesian inverse problems seek to *infer knowledge from data*.

2.4.1 Bayesian inverse problems and UQ

Another reason is that Bayesian inversion offers *uncertainty quantification*. That is, the uncertainty in the unknown parameter $\mathbf{u}$ is fully described by the posterior probability distribution. The Bayesian posterior probability distribution accounts for the uncertainties in the observations, the forward model, and the prior knowledge, thus completely quantifying the uncertainty in the unknown parameter $\mathbf{u}$.

Note the single point estimate given by the solution to the deterministic inverse problem (2.5) does not account for the uncertainty in the solution.

To keep the discussion short, the presentation of Bayesian inversion here is finite-dimensional (i.e. after a finite element method (FEM) discretization of the parameter space). However, in the numerical results presented in section 3.7 and section 5.5, discretization is performed rigorously following [23, 135]. Please see [26] for elaboration of the infinite-dimensional framework and the subtle mathematical issues related to the proper choices of

prior and discretization, and [23] for the exact construction used.

The rest of this dissertation refers to $\mathbf{u}$ and $\mathbf{u}$ and their discretized quantities unless specified (here, the nodal values with a finite element discretization).

Thus, our discretized unknown parameter $\mathbf{u}$ is a finite dimensional vector in $\mathbb{R}^P$, where P is the number of FEM mesh points. Since we assume $\mathbf{u}$ is spatially heterogeneous over Ω—similar to large-scale inverse problems of interest—this implies we have a sufficiently high-resolution mesh discretization and therefore P is large. The same mesh is used for the discretized state $u \in \mathbb{R}^P$.

The additive-noise model (2.2) is used to construct the likelihood pdf which is expressed as

$$\pi_{\text{like}}(\mathbf{d}|\mathbf{u}) \propto \exp\left(-\frac{1}{2}\left\|\widehat{\mathbf{d}} - \widehat{\mathbf{F}}(\mathbf{u})\right\|^2\right). \tag{2.6}$$

For concreteness of presentation, for Chapter 3 and Chapter 5 it is postulated that the prior is a Gaussian random field with mean $\overline{\mathbf{u}}$ and a covariance operator $\mathcal{C}$. $\mathbf{\Gamma}_{\text{prior}}$ is the discrete analog of an infinite-dimensional smoothness prior covariance $\mathcal{C}_{\text{prior}}$ that is constructed following [23]. Specifically, $\mathcal{C} = \mathcal{A}^{-2}$, where $\mathcal{A}$ is a Laplacian-like operator with its domain of definition specified by an elliptic PDE, appropriately-chosen boundary conditions, and parameters than can encode spatial correlation and anisotropy information (for specific implementation details see [6, 26]). This choice avoids constructing and inverting a dense covariance matrix and exploits existing fast solvers for elliptic operators. It additionally provides a connection to the Matérn covariance functions used frequently in geostatistics [77, 89, 127] and therefore has a scientific justification.

This choice of this $\mathcal{C}_{\text{prior}}$ is only to ensure basic sanity criteria (e.g. bounded pointwise variance) and well-posedness of the Bayesian inverse problem under the criteria for a trace-class operator in [135], and to be computationally amenable to large-scale problems. The reader is referred to [23, 135] for further discussion.

Note that the square root is not known for arbitrary generalized covariance functions common in geostatistical inverse problems. Thus, Chapter 4 addresses a practical data-driven method amenable for generalized covariance matrices in geostatistical problems.

Thus, given the assumption of a Gaussian prior and the additive noise model (2.2), $\mathbb{R}^D$, the posterior density function (pdf) of $\mathbf{u}$—the solution to the Bayesian inverse problem—is

$$\pi\left(\mathbf{u}|\mathbf{d}\right) \propto \exp\left(-\frac{1}{2}\|\mathbf{F}(\mathbf{u})-\mathbf{d}\|^2_{\mathbf{\Gamma}^{-1}_{\text{noise}}} - \frac{1}{2}\left\|\mathbf{u}-\mathbf{u}_0\right\|^2_{\mathbf{\Gamma}^{-1}_{\text{prior}}}\right) \tag{2.7}$$

where $\mathbf{F}(\mathbf{u}) \in \mathbb{R}^D$ is the parameter-to-observable map and $\mathbf{\Gamma}_{\text{prior}}$ is an appropriately chosen prior covariance matrix.

Unfortunately, there are no closed-form expressions for moments of the posterior in general [40]. Despite the choice of Gaussian prior and noise, the posterior probability need not be Gaussian, due to the nonlinearity of $\mathbf{F}(\mathbf{u})$.

The non-Gaussianity of the posterior poses significant challenges for large-scale inverse problems. First, it is a surface in high-dimensions R^P where P is large (on the order of thousands or millions). Also, the evaluation of each point on this surface requires an expensive forward PDE solve. Thus, standard computational methods for interrogating the posterior, such as vanilla Markov chain Monte Carlo (MCMC)—which can require millions of samples to converge—are not feasible for large-scale problems [25, 38, 65, 148].

2.4.2 The MAP estimation problem

In this light of these computational difficulties, the first step is to compute the *maximum a posteriori* (MAP) point of the posterior. The MAP can be used as the mean of a Gaussian approximation to the posterior. Then, if $\mathbf{F}(\mathbf{u})$ is weakly nonlinear, the Gaussian posterior approximation is completely characterized by the MAP and the approximate co-

variance (computed, e.g. using the method in [47] or [25]), and the Bayesian inverse problem is solved. Even if the Gaussian approximation fails to adequately describe the posterior, however, it can still be used as a proposal distribution in MCMC [25] to speed-up MCMC convergence.

The MAP point of (2.7) is defined as

$$\mathbf{u}^{\text{MAP}} := \arg\min_{\mathbf{u}} J(\mathbf{u}) = \frac{1}{2}\|\mathbf{F}(\mathbf{u}) - \mathbf{d}\|^2_{\mathbf{\Gamma}^{-1}_{\text{noise}}} + \frac{1}{2}\|\mathbf{u} - \mathbf{u}_0\|^2_{\mathbf{\Gamma}^{-1}_{\text{prior}}} . \tag{2.8}$$

Note that (2.8) looks similar to the traditional least squares formulation of deterministic inverse problems. In fact, this is an important insight—the solution to (2.8) is *exactly* the solution of a deterministic inverse problem, where the regularization is the negative log prior in (2.7) and the data misfit is weighted by the inverse noise covariance $\mathbf{\Gamma}^{-1}_{\text{noise}}$. This connection allows the use powerful state-of-the-art gradient-based solvers from large-scale PDE-constrained optimization in the Bayesian inverse problem.

Understanding the MAP point in a Bayesian framework also allows one to account for the subjectivity of choosing a prior. Again, the goal of the Bayesian solution is a statistical description of *all solutions* consistent with the data.

Chapter 3

The randomized misfit approach: A reduction strategy for problems with big data

This chapter is the content of a research publication by the author [83]. It introduces the randomized misfit approach (RMA) for solving large-scale Bayesian inverse problems with high-dimensional observed data (big data). The RMA is designed to reduce the impact of the large data dimension on computational complexity, while sufficiently preserving essential parameter information in noisy data. This chapter is included this dissertation because it demonstrates a data-driven reduction strategy to target a root cause of computational complexity in expensive-to-solve Bayesian inverse problems. The contributions of the author to the multi-authored article included development of the complexity analysis and theory, producing the mathematical proofs, writing the manuscript, and generating the numerical results.

3.1 Motivation for a data-scalable randomized misfit approach

Although the emerging big data paradigm in computational science and engineering offers tremendous potential to increase knowledge about persistently uncertain parameters in large-scale inverse problems, it also promises to increase the current complexity challenges.

The dominant computational cost of inversion methods in the large-scale setting is measured in number of PDE solves. Relative to the cost of a model run, mesh generation and linear algebra costs are considered negligible. Each PDE solve can take minutes to hours, even on modern supercomputers (e.g. [25, 80, 94]). Current methods require repeated

evaluations of an objective functions and its derivative information, resulting in a total cost of hundreds, thousands, or millions of PDE solves for many realistic inverse problems. Thus, even with state-of-the-art methods, the computational cost of solving large-scale Bayesian problems is prohibitive.

New strategies must be developed in order to meet the new data challenges and exploit big data for information about unknown model parameters. The aim of this chapter is to identify the effect of big data on the computational complexity of solving large-scale Bayesian inverse problems, and demonstrate how a randomized misfit approach can address this impact with both theoretical and numerical results.

Note that the idea of randomizing a misfit function is not new. Randomized approximations of misfit functions can be found in methods for seismic inversion [9, 99, 143], in stochastic optimization algorithms such as stochastic gradient descent (see e.g. [46, 131]), and in the sample average approach (SAA) [78, 103, 132].

What is new here is the particular randomized misfit framework and the resulting analysis. The randomized objective function or log posterior is derived by taking the sample average of a stochastic reformulation of the objective function (2.8). This technique is typically justified as a Monte Carlo method, which converges to the original objective function as the number of samples n goes to infinity. However, it is not obvious why the minimizer of this randomized function—the randomized MAP point—should converge to the MAP point of the original problem, or that it should be a valid estimate when $n = \mathcal{O}(1)$. Yet here and in the existing randomized misfit methods mentioned above, it is observed that high-quality randomized MAP estimates can be obtained with small n.

This chapter proves that a connection with random projection theory is the key to understanding why the RMA method results in an acceptable solution for a surprisingly small randomized misfit dimension, and not just in the limit. This is essential in order to

show that the RMA effectively bounds the computational impact of big data in solving large-scale inverse problems. The analysis here could potentially be extended to existing methods that use randomized objective functions, and the next chapter demonstrates an extension to a randomized inversion method for large-scale problems in subsurface hydrogeology.

3.2 Background on random projections for high-dimensional data

Roughly speaking, random projections are "quasi-orthogonal" transformations from high-dimensional spaces to much lower-dimensional spaces that, with high probability, preserve geometric properties such as Euclidean norms, distances, and angles. They are particularly appreciated for possessing such properties *independent of the original data dimension*. The geometric invariance properties are a consequence of the concentration of measure phenomenon in high dimensions. One can check that two high-dimensional random Gaussian vectors on the unit sphere are nearly orthonormal, and that this phenomenon becomes more pronounced as the dimension grows larger.[1]

Here it is shown that for a broad class of distributions, the probability that a sample average falls within a specified ball around its mean grows exponentially high with the sample size. This is due to the power of many independent random projections working together. Random projections provide probabilistic accuracy bounds that are parameterized by the degree of approximation or the dimension of the reduced space. That is, given a tolerance of approximation, one can find the reduced space dimension that will preserve Euclidean norm and vice versa. To assist in the practical use and verification of the RMA method, the numerical examples in section 3.7 use random projections that are implementation-friendly.

An active area of research is developing optimization methods for when the data set does not even fit in memory. The data needs to be subsampled prior to input. It must be

[1](See https://gitlab.com/ellenble/shared/tree/master/RandomProjectionDemo for a demonstration in MATLAB.)

stressed here that this is not the main target of the randomized misfit approach. In the approach presented here, the data vector is not subsampled, but rather the misfit between the model and the data is linearly transformed to a smaller dimension where its geometric properties are preserved. This is equivalent to summing random linear combinations of the misfit components. Note this is not cleaning the data, fusing data points, or choosing a random subset of data to represent the full data set. The entire data set is used. The motivation is that the dominant cost in our problem setting is the number of PDE solves. The misfit vector dimension, as will be shown, is a hard upper bound on a dominant factor of the total complexity, if using a state-of-the-art solver.

Thus the RMA can be used to transform the misfit vector to a smaller dimension, and quantifiably reduce the source of computational complexity in solving big data inverse problems, while guaranteeing the validity of the converged MAP estimate. The computational complexity reduction is discussed in detail in subsection 3.6.3.

The presentation is here is purposefully general and does not assume any particular underlying structure of the observational data, aside from its relationship to parameter space via the parameter-to-observable map and the noise model. Again there is a large body of work in data sampling, compression and/or fusion that exploits known underlying structure of the observational data set, typically for specific inverse problems. These methods are not incompatible with the approach we outline. They could potentially be combined with the method here to provide maximum computational savings.

3.3 Background on randomized methods for solving inverse problems

Since [55], many randomized methods to reduce the computational complexity of large-scale PDE-constrained inverse problems have focused on use of the randomized SVD algorithm of [95]. This algorithm has been used to generate truncated SVD approximations

of the parameter-to-observable operator [6, 34, 65, 150, 151], the regularization operator [73, 84], or the prior-preconditioned Hessian of the objective function [5, 22, 25, 26, 127]. The algorithm uses a random projection matrix to produce a low-rank operator. To our knowledge, only Gaussian distributions are used. The randomized operator is subsequently factored to generate an approximate SVD decomposition for the original operator $\mathcal{A}$. Theoretical results in [95] guarantee the spectral norm accuracy of this approximation is of order $\sigma_{k+1}(\mathcal{A})$ with a very high user-defined probability. Here k is equal to the reduced dimension n plus a small number of oversampling vectors. Subsequently, results known about the accuracy of a deterministic inverse solution (e.g., Proposition 1 in [128], Theorem 1 in [150]) to a problem approximated with a randomized method are derived using this bound from [95]. The bounds assume knowledge of $\sigma_{k+1}(\mathcal{A})$.

Random source encoding or *simultaneous (random) source* methods have been shown to be effective for parameter estimation in PDE-constrained inverse problems with multiple right-hand sides (sources) and corresponding data sets [54, 81, 82, 102, 118, 119, 120, 121, 122, 123, 143]. This problem framework characterizes many inverse problems, including electromagnetic imaging (e.g. [52, 111]), seismic waveform inversion (e.g. [58, 81, 115, 147]), the DC resistivity problem (e.g. [53, 53]), and electromagnetic impedance tomography (e.g. [44] or Sec. 6.3 in [69]). Simultaneous source methods take random linear combinations of s sources to produce $\tilde{s}$ randomly combined sources, where $\tilde{s} \ll s$. The result is a randomized misfit function that requires just $\tilde{s}$ PDE solves to evaluate instead of s PDE solves. The work in [154] shows that source encoding in its stochastic reformulation (and as a stochastic trace estimator method [62]) is equivalent to an application of the random projection defined in [1]. Simultaneous source methods point out that numerical solutions are surprisingly better than the theory predicts with a small number of sources $\tilde{s}$ (e.g. $\tilde{s} \sim \mathcal{O}(1)$) [9, 54, 81, 118, 119, 120, 121, 122, 154].

This chapter extends the above work in several directions. The RMA allows for a

stochastic reformulation of all PDE-constrained inverse problems recast in a constrained least-squares formulation, not just multi-source problems. The analysis of computational efficiency is necessarily different and depends on how the large data dimension affects the optimization. The computational cost reduction for this method is demonstrated, and is shown to be different and more generalizable than the reduction offered by simultaneous source methods.

3.4 A prototype big data Bayesian inverse problem

This reach of this chapter is restricted to MAP computation, a necessary starting point, in order to focus on methodology development in addressing the challenge of big data, i.e., large N. Scalability and efficiency of the method in the Bayesian setting is the focus of ongoing work.

3.5 Randomized misfit approach (RMA): Method derivation

The following is the basic derivation of the randomized misfit approach as a Monte Carlo method (as the number of random realizations n goes to infinity), and the intuition and analysis of its efficacy *for small* n is detailed in the following section.

Let $\mathbf{r} \in R^N$ be a random vector with mean zero and identity covariance, i.e. $\mathbb{E}_{\mathbf{r}}\left[\mathbf{r}\mathbf{r}^\top\right] = \mathbf{I}$ (equivalently, let $\mathbf{r}$ be the vector of N i.i.d. random variables ζ with mean zero and variance 1).

Then the misfit term of (2.8) can be rewritten as:

$$\left\|\widehat{\mathbf{d}} - \widehat{\mathbf{F}}(\mathbf{u})\right\|^2 = \left(\widehat{\mathbf{d}} - \widehat{\mathbf{F}}(\mathbf{u})\right)^\top \mathbb{E}_{\mathbf{r}}\left[\mathbf{r}\mathbf{r}^\top\right]\left(\widehat{\mathbf{d}} - \widehat{\mathbf{F}}(\mathbf{u})\right) = \mathbb{E}_{\mathbf{r}}\left[\mathbf{r}^\top\left(\widehat{\mathbf{d}} - \widehat{\mathbf{F}}(\mathbf{u})\right)\right]^2, \tag{3.1}$$

which allows us to write the objective functional in (2.8) as

$$J(\mathbf{u}) = \frac{1}{2}\mathbb{E}_{\mathbf{r}}\left[\mathbf{r}^\top\left(\widehat{\mathbf{d}} - \widehat{\mathbf{F}}(\mathbf{u})\right)\right]^2 + \frac{1}{2}\left\|\mathbf{u} - \mathbf{u}_0\right\|^2_{\mathbf{C}}. \tag{3.2}$$

We then approximate the expectation $\mathbb{E}_{\mathbf{r}}[\cdot]$ using a Monte Carlo approximation (also known as the Sample Average Approximation (SAA) [103, 132]) with n i.i.d. draws $\{\mathbf{r}_j\}_{j=1}^n$. This leads to the randomized inverse problem

$$\begin{aligned}\min_{\mathbf{u}} \quad J_n(\mathbf{u};\mathbf{r}) &= \frac{1}{2n}\sum_{j=1}^{n}\left[\mathbf{r}_j^\top\left(\widehat{\mathbf{d}}-\widehat{\mathbf{F}}(\mathbf{u})\right)\right]^2+\frac{1}{2}\|\mathbf{u}-\mathbf{u}_0\|_{\mathbf{C}}^2. \\ &= \frac{1}{2}\left\|\tilde{\mathbf{d}}-\tilde{\mathbf{F}}(\mathbf{u})\right\|^2+\frac{1}{2}\|\mathbf{u}-\mathbf{u}_0\|_{\mathbf{C}}^2, \end{aligned} \tag{3.3}$$

where $\tilde{\mathbf{d}} := \frac{1}{\sqrt{n}}[\mathbf{r}_1,\dots,\mathbf{r}_n]^\top\widehat{\mathbf{d}}$, and $\tilde{\mathbf{F}}(\mathbf{u}) := \frac{1}{\sqrt{n}}[\mathbf{r}_1,\dots,\mathbf{r}_n]^\top\widehat{\mathbf{F}}(\mathbf{u}) \in \mathbb{R}^n$. We call $\tilde{\mathbf{d}}-\tilde{\mathbf{F}}(\mathbf{u})$ the *reduced data misfit vector*.

For a *reduced misfit vector dimension* $n \ll N$, we call this randomization the randomized misfit approach (RMA). The new problem (3.3) with fixed i.i.d. realizations $\{\mathbf{r}_j\}_{j=1}^n$ may be solved using any scalable robust optimization algorithm. For the numerical experiments in section 3.7, a globalized inexact Newton-CG implementation [15] is used. The use of a similar mesh-independent Newton-type method is assumed for the discussion of computational complexity in subsection 3.6.3.

We define the RMA MAP point, the MAP point of (3.3), as

$$\mathbf{u}_n^{\mathrm{MAP}} := \arg\min_{\mathbf{u}} J_n(\mathbf{u}), \tag{3.4}$$

the optimal RMA cost as $J_n^\star := J_n\left(\mathbf{u}_n^{\mathrm{MAP}}\right)$, and the optimal true cost as $J^\star := J\left(\mathbf{u}^{\mathrm{MAP}}\right)$. We wish to characterize the errors $|J_n^\star - J^\star|$ and $\left\|\mathbf{u}_n^{\mathrm{MAP}}-\mathbf{u}^{\mathrm{MAP}}\right\|$ for a given reduced misfit dimension n. This is the subject of section 3.6.

3.6 Theoretical analysis of the randomized misfit approach

3.6.1 A guarantee of validity for the RMA solution with small n

For a given $\mathbf{u}$ in parameter space, it is clear that $J_n(\mathbf{u};\mathbf{r})$ in (3.3) is an unbiased estimator of $J(\mathbf{u})$. It is also clear from the Law of Large Numbers that $J_n(\mathbf{u})$ converges

almost surely to its mean $J(\mathbf{u})$. However, demonstrating the efficacy of the randomized misfit approach *with a small number of random realizations* n, lies in exploiting a "concentration of measure" phenomenon in high dimensions. That is, the first step is to quantify convergence of $J_n(\mathbf{u})$ *close to its mean* $J(\mathbf{u})$.

This requires characterizing the exponential decay of the objective function error, which is parameterized by the reduced misfit dimension n.

We first show that errors larger than $\delta/2$, for a given $\delta > 0$, decay with a rate at least as fast as the tail of a centered Gaussian. That is, for some distribution in (3.3) we have

$$\mathbb{P}\left[|J_n(\mathbf{u};\mathbf{r}) - J(\mathbf{u})| > \frac{\delta}{2}\right] \leq e^{-nI(\delta)}, \tag{3.5}$$

where

$$I(\delta) \geq c\frac{\delta^2}{2\theta^2}. \tag{3.6}$$

for some $c > 0$ and some θ.

This rate is sufficient to guarantee the solution attained from the the randomized misfit approach is a discrepancy principle-satisfying solution for the original inverse problem as will be shown in Theorem 2. Inequality (3.5) is equivalent to the statement that $\mathbb{P}\left[|J_n(\mathbf{u};\mathbf{r}) - J(\mathbf{u})| > \frac{\delta}{2}\right]$ satisfies a *large deviation principle* with *large deviation rate function* $I(\delta)$ [139].

The following proposition may be viewed as a special case of Cramér's Theorem, which states that a sample mean of i.i.d. random variables X asymptotically obeys a large deviation principle with rate $I(\delta) = \sup_k \left\{k\delta - \ln \mathbb{E}\left[e^{kX}\right]\right\}$ [139]. However we require the exact non-asymptotic bounds as derived here to show convergence of the RMA for $n = \mathcal{O}(1)$. Recall that a real-valued random variable X is θ-*subgaussian* if there exists some $\theta > 0$ such that for all $t \in \mathbb{R}$, $\mathbb{E}\left[e^{tX}\right] \leq e^{\theta^2 t^2/2}$.

Proposition 1. *The RMA error* $|J_n(\mathbf{u};\mathbf{r}) - J(\mathbf{u})|$ *has a tail probability that decays exponentially in* n *with a nontrivial large deviation rate. Furthermore, if the RMA is constructed with*

$\mathbf{r}$ *such that* $2|J_n(\mathbf{u};\mathbf{r}) - J(\mathbf{u})|$ *is the sample mean of i.i.d.* θ*-subgaussian random variables, then its large deviation rate is bounded below by* $c\frac{\delta^2}{2\theta^2}$ *for some* $c > 0$.

Proof. Given $\mathbf{r}$, define the random variable

$$T(\mathbf{r};\mathbf{u}) := \left[\mathbf{r}^\top\left(\widehat{\mathbf{d}} - \widehat{\mathbf{F}}(\mathbf{u})\right)\right]^2 - \left\|\widehat{\mathbf{d}} - \widehat{\mathbf{F}}(\mathbf{u})\right\|^2. \tag{3.7}$$

By a standard Chernoff bound (see, e.g.[71]), we have that the RMA tail error decays exponentially as

$$\mathbb{P}\left[\frac{1}{n}\sum_{j=1}^{n} T(\mathbf{r}_j;\mathbf{u}) > \delta\right] \leq e^{-nI(\delta)}, \tag{3.8}$$

where $I(\delta) = \max_t \left\{t\delta - \ln \mathbb{E}\left[e^{tT(\mathbf{r};\mathbf{u})}\right]\right\}$ is the large deviation rate.

The second part of the proposition follows with $c = 1$ by bounding $\mathbb{E}\left[e^{tT(\mathbf{r};\mathbf{u})}\right]$ in (3.8) and computing the maximum of $t\delta - \theta^2 t^2/2$. □

A large number of distributions are subgaussian, notably the Gaussian and Rademacher (also referred to as Bernoulli) distributions, and in fact any bounded random variable is subgaussian. One class of subgaussian distributions that provides additional computational efficiency is the following.

Definition 1 (ℓ-percent sparse random variables [86, 96])**.** *Let* $s = \frac{1}{1-\ell}$ *where* $\ell \in [0,1)$ *is the level of sparsity desired. Then*

$$\zeta \quad = \quad \sqrt{s}\begin{cases} +1 & \text{with probability } \frac{1}{2s}, \\ 0 & \text{with probability } \ell = 1 - \frac{1}{s}, \\ -1 & \text{with probability } \frac{1}{2s} \end{cases} \tag{3.9}$$

is a ℓ-percent sparse distribution.

Note that for $\ell = 0$, ζ corresponds to a Rademacher distribution, and that $\ell = 2/3$ corresponds to the *Achlioptas distribution* [1]. By inspection we have that $\mathbb{E}[\zeta] = 0$ and $\mathbb{E}[\zeta^2] = 1$, and thus draws from ζ can be used in the randomized misfit approach.

The distributions arising from Definition 1 are well-suited for the randomized misfit approach. They are easy to implement, and the computation of the randomized misfit vector amounts to only summations and subtractions, adding a further speedup to the method. Increasing from $s = 1$ to $s > 1$ results in a s-fold speedup as only $1/s$ of the data is included. Note the RMA cost can be seen as the sum of n random combinations from the N-dimensional misfit vector. Since each random combination has a different sparsity pattern, we effectively do not exclude any data, yet each computation requires only $1/s$ of the data.

The distributions defined by Definition 1, where $1 \leq s < \infty$, the random variable ζ distributed by Definition 1 have $\mathbb{E}\left[e^{t\zeta}\right] \leq e^{\frac{b^2t^2}{2}}$ with $b = \sqrt{s - 2\ln s}$, $\forall t \in (0, 1]$: Using the inequality $(2k)! \geq 2^k k!$ and the Taylor expansion around 0, for $t \in (0, 1]$

$$\mathbb{E}\left[e^{t\zeta}\right] = \frac{1}{s}\sum_{k=0}^{\infty}\frac{(st^2)^k}{(2k)!} \leq \frac{1}{s}\sum_{k=0}^{\infty}\frac{(st^2)}{2^k k!} = \frac{1}{s}e^{\frac{s}{2}t^2} = e^{-\ln s + \frac{s}{2}t^2} \leq e^{-t^2\ln s + \frac{s}{2}t^2}. \tag{3.10}$$

So, the distributions defined Definition 1 are permitted in the following theorem, which defines the random projections that will lead to a RMA solution with a guarantee of validity.

Theorem 1. *Define* $\mathbf{v} := \widehat{\mathbf{d}} - \widehat{\mathbf{F}}(\mathbf{u}) \in \mathbb{R}^N$. *If* $\mathbf{r}$ *in* (3.7) *has components that are* b*-subgaussian for some* $b \geq 1/\sqrt{2}$, *then the RMA error has a large deviation rate bounded below by* $c\frac{\delta^2}{2\theta^2}$ *for* $\theta = \|\mathbf{v}\|^2/\sqrt{2}$ *and some* $0 < c < \frac{1}{8b^4}$.

Proof. Let $\mathbf{r} \in \mathbb{R}^N$ such that $\mathbf{r}$ has i.i.d. b-subgaussian components r_i, with $b \geq 1/\sqrt{2}$, $\mathbb{E}[r_i] = 0$, and $\mathbb{E}[r_i^2] = 1$. Define $\mathbf{w} = \frac{\mathbf{v}}{\|\mathbf{v}\|}$ and $X = \mathbf{r}^\top\mathbf{w}$. Then

$$\mathbb{E}\left[e^{tT}\right] = e^{-t\|\mathbf{v}\|^2}\mathbb{E}\left[e^{t\|\mathbf{v}\|^2X^2}\right] \qquad \forall t \in \mathbb{R}. \tag{3.11}$$

From [96, Lemma 2.2], $\mathbb{E}[X^2] = 1$ and X is also b-subgaussian. Then, by [64, Remark 5.1], for $0 \leq t \leq \frac{1}{4b^2}$,

$$\mathbb{E}\left[e^{tX^2}\right] \leq \sqrt{2}. \tag{3.12}$$

For $0 < t \leq \frac{1}{4b^2\|\mathbf{v}\|^2}$, we have

$$\begin{aligned}
\mathbb{E}\left[e^{t\|\mathbf{v}\|^2 X^2}\right] &\leq 1 + t\|\mathbf{v}\|^2 + t\|\mathbf{v}\|^4 \frac{\mathbb{E}[X^4]}{2} + \sum_{k=3}^{\infty} \frac{\left(\frac{1}{4b^2}\right)^k \left(4b^2 t\|\mathbf{v}\|^2\right)^k \mathbb{E}\left[X^{2k}\right]}{k!} \\
&\leq 1 + t\|\mathbf{v}\|^2 + t^2\|\mathbf{v}\|^4 \frac{\mathbb{E}[X^4]}{2} + \left(4b^2 t\|\mathbf{v}\|^2\right)^3 \sum_{k=3}^{\infty} \frac{\left(\frac{1}{4b^2}\right)^k \mathbb{E}\left[X^{2k}\right]}{k!} \\
&\leq 1 + t\|\mathbf{v}\|^2 + t^2\|\mathbf{v}\|^4 \frac{\mathbb{E}[X^4]}{2} + \left(4b^2 t\|\mathbf{v}\|^2\right)^3 \mathbb{E}\left[e^{\frac{1}{4b^2}X^2}\right] \\
&\leq 1 + t\|\mathbf{v}\|^2 + t^2\|\mathbf{v}\|^4 \frac{\mathbb{E}[X^4]}{2} + 64\sqrt{2}b^6 t^3\|\mathbf{v}\|^6 \\
&\leq 1 + t\|\mathbf{v}\|^2 + 8b^4 t^2\|\mathbf{v}\|^4 + 64\sqrt{2}b^6 t^3\|\mathbf{v}\|^6 \\
&\leq e^{t\|\mathbf{v}\|^2 + 8b^4 t^2\|\mathbf{v}\|^4 + 64\sqrt{2}b^6 t^3\|\mathbf{v}\|^6},
\end{aligned}$$

using (3.12) in the fourth inequality and [134, p.93] in the fifth inequality. Let $t_\star = \frac{\delta}{8b^4\|\mathbf{v}\|^4 q}$ where $q > 1$. Assuming $\|\mathbf{v}\|^2 \gg \delta$, we have that

$$\mathbb{E}\left[e^{t^\star T}\right] \leq e^{8b^4 t_\star^2\|\mathbf{v}\|^4 + 64\sqrt{2}b^6 t_\star^3\|\mathbf{v}\|^6} = e^{\frac{\delta^2}{8b^4\|\mathbf{v}\|^4 q^2} + \sqrt{2}\frac{\delta^3}{8b^6\|\mathbf{v}\|^6 q^3}}.$$

Then

$$I(\delta) \geq \delta t_\star - \ln \mathbb{E}\left[e^{t_\star T}\right] \geq \left(1 - \frac{1}{q}\right)\frac{\delta^2}{8b^4\|\mathbf{v}\|^4 q} - \sqrt{2}\frac{\delta^3}{8b^6\|\mathbf{v}\|^6 q^3} \geq c\frac{\delta}{\|\mathbf{v}\|^4},$$

where $0 < c < \frac{1}{8b^4}$. Taking $2\theta^2 = \|\mathbf{v}\|^4$ concludes the proof. □

A sharper result can be obtained for RMA constructed with b-subgaussian random variables where $b \leq 1$. Note that this includes the distribution Definition 1 with $s = 1$ (Rademacher) and $s = 3$ (Achlioptas) by the above theorem. Following [64, (5)], let g be a standard Gaussian random variable, independent of all other random variables. Then, we have that for $0 < t < \frac{1}{2\|\mathbf{v}\|^2}$,

$$\mathbb{E}\left[e^{t\|\mathbf{v}\|^2 X}\right] \leq \mathbb{E}_g\left[\prod_i^N e^{b^2 t\|\mathbf{v}\|^2 w_i^2 g^2}\right] \leq \mathbb{E}_g\left[e^{t\|\mathbf{v}\|^2 g^2}\right] = \frac{1}{\sqrt{1 - 2t\|\mathbf{v}\|^2}}. \tag{3.13}$$

So from (3.11) we have that

$$\mathbb{E}\left[e^{tT(\mathbf{u},\mathbf{r})}\right] \leq \frac{e^{-t\|\mathbf{v}\|^2}}{\sqrt{1-2t\|\mathbf{v}\|^2}} = e^{-t\|\mathbf{v}\|^2-\frac{1}{2}\ln\left(1-2t\|\mathbf{v}\|^2\right)}. \tag{3.14}$$

Then

$$t\delta - \ln\left(\mathbb{E}\left[T\left(\mathbf{u},\mathbf{r}\right)\right]\right) \geq t\delta + t\|\mathbf{v}\|^2 + \frac{1}{2}\ln\left(1-2t\|\mathbf{v}\|^2\right) =: f\left(t\right). \tag{3.15}$$

Computing the derivative, we have that $f\left(t\right)$ attains a maximum at

$$t_{\max} = \frac{\delta}{2\left(\|\mathbf{v}\|^4 + \delta\|\mathbf{v}\|^2\right)}. \tag{3.16}$$

Thus, we have

$$\begin{aligned}
\max f\left(t\right) &= \frac{\delta^2}{2\left(\|\mathbf{v}\|^4+\delta\|\mathbf{v}\|^2\right)} + \frac{\delta}{2\left(\|\mathbf{v}\|^2+\delta\right)} + \frac{1}{2}\ln\left(1-\frac{\delta}{\|\mathbf{v}\|^2+\delta}\right) \\
&= \frac{\delta^2}{2\left(\|\mathbf{v}\|^4+\delta\|\mathbf{v}\|^2\right)} - \frac{1}{4}\frac{\delta^2}{\left(\|\mathbf{v}\|^2+\delta\right)^2} - \frac{1}{6}\frac{\delta^3}{\left(\|\mathbf{v}\|^2+\delta\right)^3} - \cdots \\
&= \frac{\delta^2}{4\left(\|\mathbf{v}\|^4+\delta\|\mathbf{v}\|^2\right)} + \frac{1}{4}\left\{\frac{\delta^2}{\left(\|\mathbf{v}\|^4+\delta\|\mathbf{v}\|^2\right)} - \frac{\delta^2}{\left(\|\mathbf{v}\|^2+\delta\right)^2}\right\} \\
&\quad - \frac{1}{6}\frac{\delta^3}{\left(\|\mathbf{v}\|^2+\delta\right)^3} - \cdots \geq c\frac{\delta^2}{\|\mathbf{v}\|^4},
\end{aligned}$$

where we employed the Taylor expansion in the second equality, and in the last inequality c is some constant less than $1/4$. Note that the last inequality holds for $\delta \ll \|\mathbf{v}\|^2$ and taking $2\theta^2 = \|\mathbf{v}\|^4$ concludes the proof.

The next theorem is the main research contribution of this chapter. It guarantees with high probability that the RMA solution will be a solution of the original problem under Morozov's discrepancy principle, for relatively small n.

The theorem requires the following lemma, which defines the

Lemma 1. *Let* $\mathbf{v} := \widehat{\mathbf{d}} - \widehat{\mathbf{F}}\left(\mathbf{u}\right)$. *Suppose that* $\mathbf{r}$ *is distributed such that the large deviation rate of the RMA error is bounded below by* $c\frac{\delta^2}{2\theta^2}$ *for some* $c > 0$ *and* $\theta = \|\mathbf{v}\|^2/\sqrt{2}$. *Given a*

cost distortion tolerance $\varepsilon > 0$ *and a* failure rate $\beta > 0$*, let*

$$n \geq \frac{\beta}{c\varepsilon^2}. \tag{3.17}$$

Then with probability at least $1 - e^{-\beta}$*,*

$$(1-\varepsilon)\left\|\mathbf{v}\right\|^2 \leq \frac{1}{n}\sum_{j=1}^{n}\left(\mathbf{r}_j^\top \mathbf{v}\right)^2 \leq (1+\varepsilon)\left\|\mathbf{v}\right\|^2, \tag{3.18}$$

and hence,

$$(1-\varepsilon)\, J\left(\mathbf{u}\right) \leq J_n\left(\mathbf{u};\mathbf{r}\right) \leq (1+\varepsilon)\, J\left(\mathbf{u}\right). \tag{3.19}$$

Proof. The proof follows from setting $\delta = \varepsilon \left\|\mathbf{v}\right\|^2$ in (3.5). □

This lemma demonstrates a remarkable fact that with n i.i.d. draws one can reduce the data misfit dimension from N to n while bearing a relative error of $\varepsilon = \mathcal{O}\left(1/\sqrt{n}\right)$ in the cost function, where the reduced dimension n is independent of the dimension N of the data. This idea is the basis for data-reduction techniques via variants of the Johnson-Lindenstrauss Lemma in existing work with random projections (see e.g. [48, 60, 91]). With the connection through the randomized misfit approach, the ubiquitous N-independent Monte Carlo factor $\varepsilon = \mathcal{O}\left(1/\sqrt{n}\right)$ in Johnson-Lindenstrauss literature can thus be understood by reframing the application of a random projection as a Monte Carlo method in the form of (3.18).

Unlike other applications of the Monte Carlo method, e.g. Markov chain Monte Carlo, in which n must be large to be successful, n can be moderate or small for inverse problems, depending on the noise $\boldsymbol{\eta}$ in (2.2). In the following theorem we show this is possible via Morozov's discrepancy principle [101]. To avoid over-fitting the noise, from (2.1) one seeks a MAP point $\mathbf{u}^{\mathrm{MAP}}$ such that $\left|d_j - \mathbf{w}\left(\mathbf{x}_j;\mathbf{u}^{\mathrm{MAP}}\right)\right| \approx \sigma$, i.e. $\left\|\widehat{\mathbf{d}} - \widehat{\mathbf{F}}\left(\mathbf{u}^{\mathrm{MAP}}\right)\right\|^2 \approx N$. We say that an inverse solution $\mathbf{u}^{\mathrm{MAP}}$ satisfies Morozov's discrepancy principle with parameter τ if

$$\left\|\widehat{\mathbf{d}} - \widehat{\mathbf{F}}\left(\mathbf{u}^{\mathrm{MAP}}\right)\right\|^2 = \tau N \tag{3.20}$$

for some $\tau \approx 1$.

Theorem 2 (Statistical Morozov's discrepancy principle)**.** *Suppose that the conditions of Lemma 1 are met. If* $\mathbf{u}_n^{MAP}$ *is a discrepancy principle-satisfying solution for the RMA cost, i.e.,*

$$\mathcal{J}_n\left(\mathbf{u}_n^{MAP}, \mathbf{r}\right) := \frac{1}{n}\sum_{j=1}^{n}\left[\mathbf{r}_j^\top\left(\widehat{\mathbf{d}} - \widehat{\mathbf{F}}\left(\mathbf{u}_n^{MAP}\right)\right)\right]^2 = \tau' N \tag{3.21}$$

for some $\tau' \approx 1$*, then with probability at least* $1 - e^{-\beta}$*,* $\mathbf{u}_n^{MAP}$ *is also a solution for the original problem that satisfies Morozov's discrepancy principle with parameter* τ*, i.e.*

$$\mathcal{J}\left(\mathbf{u}_n^{MAP}\right) := \left\|\widehat{\mathbf{d}} - \widehat{\mathbf{F}}\left(\mathbf{u}_n^{MAP}\right)\right\|^2 = \tau N. \tag{3.22}$$

for $\tau \in \left[\frac{\tau'}{1+\varepsilon}, \frac{\tau'}{1-\varepsilon}\right]$.

Proof. The claim is a direct consequence of (3.18). □

3.6.2 Other theoretical results

We are now in the position to show a different proof of the Johnson-Lindenstrauss embedding theorem using a stochastic programming derivation of the RMA. Following [129], we define a map $\mathcal{S}$ from $\mathbb{R}^n$ to $\mathbb{R}^N$, where $n \ll N$, to be a Johnson-Lindenstrauss transform (JLT) if

$$(1-\varepsilon)\|\mathbf{v}\|^2 \leq \|\mathcal{S}\mathbf{v}\|^2 \leq (1+\varepsilon)\|\mathbf{v}\|^2, \tag{3.23}$$

holds with some probability $p = p(n, \varepsilon)$, where $\varepsilon > 0$.

Theorem 3 (Johnson-Lindenstrauss embedding theorem [42, 64, 96])**.** *Suppose that* $\mathbf{r}$ *is distributed such that the large deviation rate of the RMA error is bounded below by* $c\frac{\delta^2}{2\theta^2}$ *for some* $c > 0$ *and some* θ*. Let* $0 < \varepsilon < 1$*,* $\mathbf{v}_i \in \mathbb{R}^N, i = 1, \ldots, m$*, and* $n = \mathcal{O}(\varepsilon^{-2}\ln m)$*. Then there exists a map* $\mathcal{F} : \mathbb{R}^N \to \mathbb{R}^n$ *such that*

$$(1-\varepsilon)\|\mathbf{v}_i - \mathbf{v}_j\|^2 \leq \|\mathcal{F}(\mathbf{v}_i) - \mathcal{F}(\mathbf{v}_j)\|^2 \leq (1+\varepsilon)\|\mathbf{v}_i - \mathbf{v}_j\|^2 \quad \forall i, j. \tag{3.24}$$

Proof. The conditions of Lemma 1 hold, thus for a given $\mathbf{v} \in \mathbb{R}^N$, note that (3.18) is equivalent to

$$(1-\varepsilon)\left\|\mathbf{v}\right\|^2 \leq \left\|\mathbf{\Sigma v}\right\|^2 \leq (1+\varepsilon)\left\|\mathbf{v}\right\|^2, \tag{3.25}$$

where

$$\mathbf{\Sigma} := \frac{1}{\sqrt{n}}\left[\mathbf{r}_1, \ldots, \mathbf{r}_n\right]^\top. \tag{3.26}$$

Define $\mathcal{F}(\mathbf{v}) := \mathbf{\Sigma v}$. Inequality (3.24) is then a direct consequence of (3.25) for a pair $(\mathbf{v}_i, \mathbf{v}_j)$ with probability at least $1 - e^{-\frac{c}{2}n\varepsilon^2}$. Using an union bound over all pairs, claim (3.24) holds for any pair with probability at least $1 - m^{-\alpha}$ if $n \geq c\frac{(2+\alpha)}{\varepsilon^2}\ln m$. □

As discussed above, $J_n(\mathbf{u};\mathbf{r})$ is an unbiased estimator of $J(\mathbf{u})$. It is therefore reasonable to expect that $J_n^\star := \min_{\mathbf{u}} J_n(\mathbf{u};\mathbf{r})$ converges to $J^\star := \min_{\mathbf{u}} J(\mathbf{u})$. The following result [132, Propositions 5.2 and 5.6] states that under mild conditions $J_n^\star$ in fact converges to $J^\star$. It is not unbiased, but is however downward biased.

Proposition 2. *Assume that $J_n(\mathbf{u};\mathbf{r})$ converges to $J(\mathbf{u})$ with probability 1 uniformly in $\mathbf{u}$, then $J_n^\star$ converges to $J^\star$ with probability 1. Furthermore, it holds that*

$$\mathbb{E}\left[J_n^\star\right] \leq \mathbb{E}\left[J_{n+1}^\star\right] \leq J^\star, \tag{3.27}$$

that is, $J_n^\star$ is a downward-biased estimator *of $J^\star$.*

Stochastic programming theory gives a stronger characterization of this convergence. One can show that $\mathbf{u}_n^{\mathrm{MAP}}$ converges weakly to $\mathbf{u}^{\mathrm{MAP}}$ with an $n^{-\frac{1}{2}}$ rate. If $J(\mathbf{u})$ is convex with finite value, then $\mathbf{u}_n^{\mathrm{MAP}} = \mathbf{u}^{\mathrm{MAP}}$ with probability exponentially converging to 1. See Chapter 5 in [132] for details. For a linear forward map $\mathbf{F}(\mathbf{u}) = \mathbf{Fu}$, that is, $J(\mathbf{u})$ is quadratic, we can derive a bound on the solution error using the spectral norm of $\mathbf{F}$.

Theorem 4. *Suppose the conditions of Lemma 1 hold. Let $m := \operatorname{rank}(\widehat{\mathbf{F}})$. Then*

i) $(1-\varepsilon)J^\star \leq J_n^\star \leq (1+\varepsilon)J^\star$, *and*

ii) if $\mathbf{F}$ *is linear, then with probability at least* $1 - m^{-\alpha}$

$$\left\|\mathbf{u}_n^{MAP} - \mathbf{u}^{MAP}\right\| \leq \frac{\varepsilon}{\sigma_{\min}^2(\mathbf{G})}\left(\left\|\widehat{\mathbf{F}}\right\|\left\|\mathbf{u}^{MAP}\right\| + \left\|\widehat{\mathbf{d}}\right\|\right)\left\|\widehat{\mathbf{F}}\right\|, \tag{3.28}$$

where $\mathbf{G} := \left(\widehat{\mathbf{F}}^\top \boldsymbol{\Sigma}\boldsymbol{\Sigma}^\top \widehat{\mathbf{F}} + \mathbf{C}^{-1}\right)^{\frac{1}{2}}$, *and* $n = \mathcal{O}\left(\varepsilon^{-2}(2+\alpha)\ln m\right)$.

Proof. The first assertion follows from (3.19) and the definition of $\mathbf{u}_n^{\mathrm{MAP}}$ (3.4), indeed

$$J_n^\star = J_n\left(\mathbf{u}_n^{\mathrm{MAP}}\right) \leq J\left(\mathbf{u}^{\mathrm{MAP}}\right) \leq (1+\varepsilon)\, J\left(\mathbf{u}^{\mathrm{MAP}}\right) = (1+\varepsilon)\, J^\star, \tag{3.29}$$

and the other direction is similar. For the second assertion, note that $\mathbf{u}^{\mathrm{MAP}}$ and $\mathbf{u}_n^{\mathrm{MAP}}$ are solutions of the following first optimality conditions

$$\left(\widehat{\mathbf{F}}^\top \widehat{\mathbf{F}} + \mathbf{C}^{-1}\right)\mathbf{u}^\star = \widehat{\mathbf{F}}^\top \widehat{\mathbf{d}} + \mathbf{C}^{-1}\mathbf{u}_0, \tag{3.30a}$$

$$\left(\widehat{\mathbf{F}}^\top \boldsymbol{\Sigma}\boldsymbol{\Sigma}^\top \widehat{\mathbf{F}} + \mathbf{C}^{-1}\right)\mathbf{u}_n^{\mathrm{MAP}} = \widehat{\mathbf{F}}^\top \boldsymbol{\Sigma}\boldsymbol{\Sigma}^\top \widehat{\mathbf{d}} + \mathbf{C}^{-1}\mathbf{u}_0. \tag{3.30b}$$

Define $\mathbf{s}\Delta := \mathbf{u}^{\mathrm{MAP}} - \mathbf{u}_n^{\mathrm{MAP}}$. An algebraic manipulation of (3.30) gives

$$\left(\widehat{\mathbf{F}}^\top \boldsymbol{\Sigma}\boldsymbol{\Sigma}^\top \widehat{\mathbf{F}} + \mathbf{C}^{-1}\right)\mathbf{s}\Delta = \left(\widehat{\mathbf{F}}^\top \boldsymbol{\Sigma}\boldsymbol{\Sigma}^\top \widehat{\mathbf{F}} - \widehat{\mathbf{F}}^\top \widehat{\mathbf{F}}\right)\mathbf{u}^{\mathrm{MAP}} + \widehat{\mathbf{F}}^\top \widehat{\mathbf{d}} - \widehat{\mathbf{F}}^\top \boldsymbol{\Sigma}\boldsymbol{\Sigma}^\top \widehat{\mathbf{d}}. \tag{3.31}$$

Taking the inner product of both sides with $\mathbf{s}\Delta$ we have

$$\left\langle \mathbf{s}\Delta, \left(\widehat{\mathbf{F}}^T \boldsymbol{\Sigma}\boldsymbol{\Sigma}^T \widehat{\mathbf{F}} + \mathbf{C}^{-1}\right)\mathbf{s}\Delta\right\rangle = \left\langle \widehat{\mathbf{F}}\mathbf{s}\Delta, \boldsymbol{\Sigma}\boldsymbol{\Sigma}^T \widehat{\mathbf{F}}\mathbf{u}^\star - \widehat{\mathbf{F}}\mathbf{u}^\star\right\rangle + \left\langle \widehat{\mathbf{F}}\mathbf{s}\Delta, \widehat{\mathbf{d}} - \boldsymbol{\Sigma}\boldsymbol{\Sigma}^T \widehat{\mathbf{d}}\right\rangle. \tag{3.32}$$

Then we can bound the left-hand side of (3.32):

$$\left\langle \mathbf{s}\Delta, \left(\widehat{\mathbf{F}}^\top \boldsymbol{\Sigma}\boldsymbol{\Sigma}^\top \widehat{\mathbf{F}} + \mathbf{C}^{-1}\right)\mathbf{s}\Delta\right\rangle \geq \sigma_{\min}^2(\mathbf{G})\,\mathbf{s}\Delta^2. \tag{3.33}$$

To bound terms on right hand side of (3.32), we need the following straightforward variant of (3.25), i.e. $\forall \mathbf{v} \in \mathbb{R}^N$ and $n = \mathcal{O}\left(\varepsilon^{-2}\right)$:

$$\left\|\boldsymbol{\Sigma}\boldsymbol{\Sigma}^\top \mathbf{v} - \mathbf{v}\right\| \leq \varepsilon \left\|\mathbf{v}\right\|. \tag{3.34}$$

Using the Cauchy-Schwarz inequality we have

$$\left\langle \widehat{\mathbf{F}}\mathbf{s}\Delta, \boldsymbol{\Sigma}\boldsymbol{\Sigma}^T\widehat{\mathbf{F}}\mathbf{u}^\star - \widehat{\mathbf{F}}\mathbf{u}^\star \right\rangle \leq \varepsilon \left\|\widehat{\mathbf{F}}\right\|^2 \|\mathbf{s}\Delta\| \|\mathbf{u}^\star\|, \tag{3.35a}$$

$$\left\langle \widehat{\mathbf{F}}\mathbf{s}\Delta, \widehat{\mathbf{d}} - \boldsymbol{\Sigma}\boldsymbol{\Sigma}^T\widehat{\mathbf{d}} \right\rangle \leq \varepsilon \left\|\widehat{\mathbf{F}}\right\| \|\mathbf{s}\Delta\| \left\|\widehat{\mathbf{d}}\right\|, \tag{3.35b}$$

where we have used (3.34) and definition of matrix norm. Next, combining (3.35) and (3.33) ends the proof.

Note that for inequalities in (3.35) to be valid, it is sufficient to choose n, α, ε such that (3.34) is valid for m basis vectors spanning the column space of $\widehat{\mathbf{F}}$, and hence $n = \mathcal{O}\left(\varepsilon^{-2}\left(2+\alpha\right)\ln m\right)$ by the union bound. □

Remark 1. *The bound in (3.28) is not a unique estimation. One can first rewrite $J(\mathbf{u})$ and $J_n(\mathbf{u};\mathbf{r})$ as*

$$\begin{aligned} J(\mathbf{u}) &= \tfrac{1}{2}\left\| \begin{bmatrix} \widehat{\mathbf{d}} \\ \mathbf{C}^{-1/2}\mathbf{u}_0 \end{bmatrix} - \begin{bmatrix} \widehat{\mathbf{F}} \\ \mathbf{C}^{-1/2} \end{bmatrix} \mathbf{u} \right\|^2, \\ J_n(\mathbf{u};\mathbf{r}) &= \tfrac{1}{2}\left\| \begin{bmatrix} \mathbf{s}\Sigma^\top & 0 \\ 0 & \mathbf{I} \end{bmatrix} \left\{ \begin{bmatrix} \widehat{\mathbf{d}} \\ \mathbf{C}^{-1/2}\mathbf{u}_0 \end{bmatrix} - \begin{bmatrix} \widehat{\mathbf{F}} \\ \mathbf{C}^{-1/2} \end{bmatrix} \mathbf{u} \right\} \right\|^2. \end{aligned}$$

If $\boldsymbol{\Sigma}$ is a Johnson-Lindenstrauss transform, then $\mathcal{S} := \begin{bmatrix} \mathbf{s}\Sigma^\top & 0 \\ 0 & \mathbf{I} \end{bmatrix}$ is also a JLT with the same parameters:

$$\left\| \mathcal{S} \begin{bmatrix} \mathbf{v} \\ \mathbf{w} \end{bmatrix} \right\|^2 = \|\mathbf{s}\Sigma\mathbf{v}\|^2 + \|\mathbf{w}\|^2 \leq (1+\varepsilon)\|\mathbf{v}\|^2 + \|\mathbf{w}\|^2 \leq (1+\varepsilon)\left\| \begin{bmatrix} \mathbf{v} \\ \mathbf{w} \end{bmatrix} \right\|^2. \tag{3.36}$$

Applying [129, Theorem 12], we conclude that with probability at least $1/3$,

$$\left\|\mathbf{u}_n^{MAP} - \mathbf{u}^{MAP}\right\| \leq \frac{\varepsilon}{\lambda_{min}}\sqrt{J^\star}, \tag{3.37}$$

where λ_{min} is the minimum nonzero singular value of $\begin{bmatrix} \widehat{\mathbf{F}}^\top, \mathbf{C}^{-1/2} \end{bmatrix}^\top$.

3.6.3 Data-scalability and cost complexity estimate

This section presents a qualitative discussion of the computational complexity and scalability of the randomized misfit approach. Numerical evidence of scalability to large data dimensions is presented in subsection 3.7.3. For concreteness and ease of comparison, a Newton-type optimization method is assumed. The theory in subsections 3.6.1 and 3.6.2 is independent of the solver used.

The cost complexity of solving the randomized problem (3.3) is measured in number of PDE solves, i.e. solves of the forward or adjoint PDE and incremental variants. This characterization of complexity is agnostic to the specific governing forward PDE or PDE solver. For nontrivial forward problems, the total runtime of MAP point computation and uncertainty quantification is overwhelmingly dominated by the PDE solves; the cost of linear algebra is negligible in comparison [6, 25, 26, 65, 114].

In particular, with an inexact Newton-CG method, the cost of each Newton step is dominated by conjugate gradient (CG) iterations. Each CG iteration requires an application of the data misfit Hessian, which in turn requires a pair of incremental forward and adjoint PDE solves [6, 25, 26, 47, 65]. Thus the total work estimate is $\mathcal{O}(2rk_{\text{Newton}})$ PDE solves. Here, k_{Newton} is the total number of Newton iterations and r is the numerical rank of the prior-preconditioned data misfit Hessian (or equivalently, the dimension of the likelihood-informed subspace (LIS) of parameter space [41]). Current state-of-the-art implementations demonstrate that, for a wide class of inverse problems, the number of outer Newton iterations k_{Newton} and the numerical rank r are both independent of the mesh-size [26, 47, 65]. Mesh-independence is essential for ensuring scalability of a method to very high parameter dimensions.

The challenge is that even though r may be independent of the mesh, it still depends on the information content of the data. For many practical large-scale problems with high-dimensional data, r is on the order of hundreds or thousands (e.g. $r = 5000$ in [65] and $r =$

1500 for a linear 3D convection diffusion problem in [47]). Consequently, even with the best methods and modern supercomputers, solving the inverse problem is still computationally expensive.

Recall that for a given inverse problem, r is a fixed constant intrinsic to the misfit function, as it is the numerical rank of the prior-preconditioned Hessian of the misfit. A Newton-type method requires $2r$ PDE solves (i.e. r inner iterations) at each outer iteration to sufficiently capture the r dominant modes of the misfit Hessian. Arbitrarily taking a much smaller number of inner iterations than r would result in more Newton iterations and degradation of the overall convergence. This constraint necessitates the use of a *surrogate misfit function*, with a Hessian that has numerical rank smaller than r, in order to bypass the impact of r on the overall cost of solving the inverse problem.

Ideally, this surrogate would leverage a small loss in the "level of parameter information in data" to obtain a large reduction in the overall computational cost of computing the inverse solution. In fact, this is what the randomized misfit approach can offer. The RMA cost is a surrogate cost that reduces the factor of r in the work estimate to an $n \ll r$, while providing a guarantee of solution viability. Note that the reduced misfit vector dimension n is a hard upper bound on the numerical rank of the misfit Hessian for the RMA cost J_n (3.3). This is numerically demonstrated for an elliptic inverse problem in subsection 3.7.3.

Using the theory in subsection 3.6.1, we can explicitly quantify the substantial gains in computational efficiency that are achieved with a specified accuracy level and a specified *confidence* level. This occurs by reframing the deterministic solution as one that holds with a given high probability.

The overall work estimate for the randomized misfit approach therefore is $\mathcal{O}(2nk_{\text{Newton}})$. This cost reduction analysis is markedly different from the analysis in the stochastic simultaneous source methods described in subsection 1.1.1. By combining a large number of input sources s into a smaller number $\tilde{s}$, stochastic methods for multiple sources reduce the original

problem from $\mathcal{O}(2rk_{\text{Newton}}s)$ to $\mathcal{O}(2rk_{\text{Newton}}\tilde{s})$ where $\tilde{s} \ll s$. Note that the RMA can provide a reduced work estimate in the most general class of inverse problems where $s = 1$ *and* a guarantee of solution viability, whereas randomized simultaneous source methods cannot.

3.7 Numerical results

In this section we demonstrate the randomized misfit approach with different distributions for $\mathbf{r}$ in (3.3). We also verify that the convergence is indeed $\mathcal{O}(1/\sqrt{n})$ as guaranteed by Theorem 3. Lastly we verify Theorem 2, the statistical Morozov's discrepancy principle.

The distributions that tested in the randomized misfit approach results of this section are:

- Gaussian
- Rademacher
- Achlioptas
- 95%-sparse (s-sparse Definition 1 with $s = 20$)
- 99%-sparse (s-sparse Definition 1 with $s = 100$)
- Uniform $\mathcal{U}\left[-\sqrt{12}/2, \sqrt{12}/2\right]$

There are many other distributions suitable for RMA in the literature on Johnson-Lindenstrauss transforms that are not considered here, particularly the Subsampled Randomized Hadamard Transform of [3, 140] and its subsequent fast and sparse variants. These will be tested in future work.

Note that subsampling (random subset) matrices, *are* geometry preserving transformations[30, 43] and with modifications on the signs of the diagonal entries can be understood as random

projections [49]. However, random subset transformations possess slower large deviation decay rates than the distributions used to justify the RMA validity in Theorem 2, such as (3.3), and thus do not preserve the same level of information for a given reduced dimension n. They require more data to achieve the same level of geometry preservation.[1]

Random source encoding methods often test subsampling matrices to reduce the dimension of the misfit [120, 121, 142]. For many inverse problems with identifiable structure in the data (e.g. 3-D hydraulic tomography [31]), subsampling can be extremely effective for reducing the computational burden of large observational datasets. However, using the definition of a subset matrix in [120, 121], subsampling down to misfit dimension n is equivalent to choosing $\mathbf{r}_j$ from the canonical set $\{\mathbf{e}_1, \ldots, \mathbf{e}_N\}$ *without* replacement. Therefore the set $\{\mathbf{r}_j\}_{j=1}^n$ is not an i.i.d set, and does not satisfy the criteria for the distributions used to arrive at Theorem 2 and define the RMA. Similar to [120, 121, 142], numerical results (omitted here) are poorer with subsampling matrices compared to results the RMA random projections when compared with the same reduced misfit dimension n.

The standard $H^1(\Omega)$ finite element method is used to discretize the misfit and the regularization operator. The synthetic truths that we seek to recover are a 1-D sinusoidal curve, a 2-D Gaussian on a thermal fin, and a cube with nonzero log conductivity values on a sphere in the center and semispheres in the opposing corners. Figure 3.1 shows representations of $\mathbf{u}_{\text{truth}}$ on a mesh for these cases.

The synthetic noisy temperature observations are then generated at all mesh points through the forward model (2.4). The misfit vector generated from Figure 3.1(a) has data dimension $N = 1025$ (with 1% percent added noise), from Figure 3.1(b) has data dimension $N = 1333$ (with .1% percent added noise), and from Figure 3.1(c) has data dimension

[1]The author thanks Prof. Rachel Ward for this subtle insight. Note this section is updated from the published RMA research article to correct the previous suggestion that subset matrices are not geometry preserving transformations—they are. At the time of publication for the research article, the author was unaware of the random subset literature in compressed sensing.

$N = 2474$ (with .2% percent added noise), respectively.

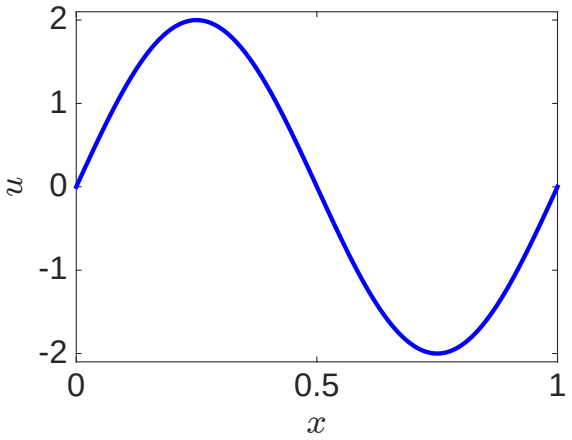

(a) truth **u** for 1D experiment

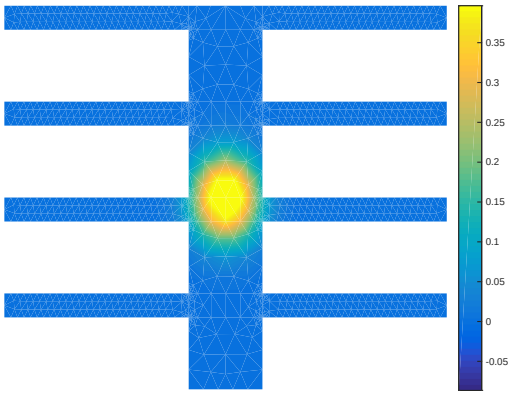

(b) truth **u** for 2D experiment

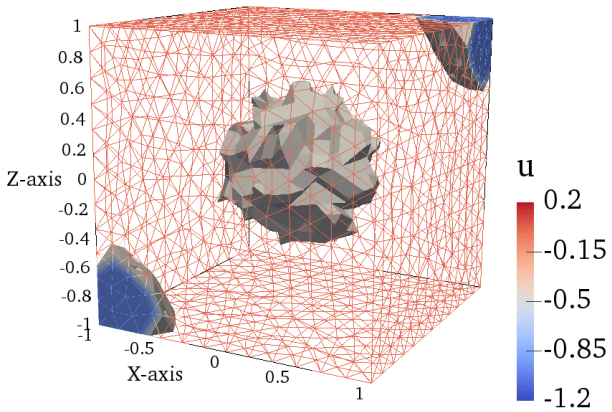

(c) truth **u** for 3D experiment

Figure 3.1: The distributed truth log conductivity parameters used in the experiments. The parameter fields are used to obtain noise-corrupted temperature data through the forward model (2.4).

For the inversion results we use an implementation of the trust region inexact Newton conjugate gradient method, for which some of the main ideas can be found in [15, 17, 36, 107]. Unless otherwise noted, the stopping criteria is when the Newton step size, cost function value, or norm of the gradient falls below 10^{-6}.

3.7.1 Convergence results

We first compare plots of the RMA cost $J_n(\mathbf{u}_0)$ to the original cost $J(\mathbf{u}_0)$ for a fixed distributed parameter $\mathbf{u}_0$, using the model heat problem (2.4). We choose a random $\mathbf{u}_0$ from the prior distribution and construct the RMA cost $J_n(\mathbf{u}_0)$ with the various random projections listed above. Since $\mathbf{u}_0$ lives in high-dimensional space $\mathbb{R}^m$, where m is the number of finite element nodal values, for the purpose of visualization Figure 3.2 shows plots of the RMA cost $\hat{J}_n(\kappa) := J_n(\mathbf{u}_0 + \kappa\mathbf{s})$ in a direction $\mathbf{s} := \nabla J(\mathbf{u}_0)$ for the 3D example. For each of the random projections tested we observe convergence of $\hat{J}_n(\kappa)$ to $\hat{J}(\kappa)$ as n increases. More importantly, for all distributions, the minimizer of $\hat{J}(\kappa)$ is well-approximated by $\hat{J}_n(\kappa)$, even for n small, as shown by Theorem 2. That is, although J_n for $n = \mathcal{O}(1)$ is far from J, the local minimizers align. This is consistent with observed fidelity of randomized MAP points despite the slow convergence of the randomized cost, and similar phenomena seen in related methods. Plots with distributions other than Achlioptas and for the 1D and 2D examples are omitted when results are similar to the 3D Achlioptas experiments (see `https://gitlab.com/ellenble/shared/blob/master/omittedplots.pdf`).

Theorem 4 states that $\mathbf{u}_n^{\text{MAP}}$, the minimizer of J_n, and the minimum objective function value $J_n^\star$ converge at the same rate, given by the distortion tolerance ε, but with different constants. Figure 3.2 illustrates how an RMA solution $\hat{\mathbf{u}}_n^\star$ may converge quickly to $\hat{\mathbf{u}}^\star$, although convergence of the minimum value $\hat{J}_n(\hat{\mathbf{u}_n})$ to $\hat{J}(\hat{\mathbf{u}})$ can be slow due to the different constant. To test this hypothesis at the actual minimizer $\mathbf{u}_n^{\text{MAP}}$, we plot the error of the RMA MAP point $\mathbf{u}_n^{\text{MAP}}$ and its corresponding optimal value $J_n^\star$ in Figure 3.3 for the 3D example and the Achlioptas random projection[2]. Data shown is the average of five runs. Both the absolute errors $|J_n^\star - J^\star|$ and $\left\|\mathbf{u}_n^{\text{MAP}} - \mathbf{u}^{\text{MAP}}\right\|$ and normalized errors $|J_n^\star - J^\star|/|J^\star|$ and $\left\|\mathbf{u}_n^{\text{MAP}} - \mathbf{u}^{\text{MAP}}\right\| / \left\|\mathbf{u}^{\text{MAP}}\right\|$ are shown, and an $\mathcal{O}(1/\sqrt{n})$ reference curve is plotted to

[2]Again, similar results are seen with the 1D and 2D examples and with different random projections. They are omitted here.

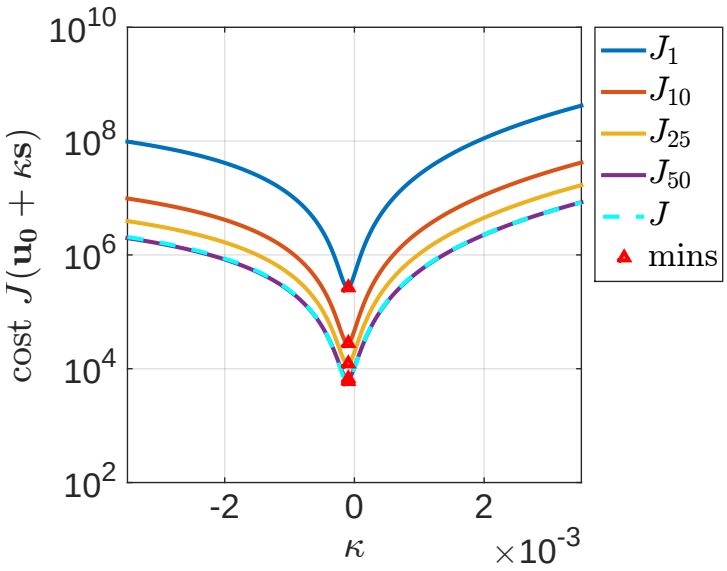

Figure 3.2: Contours of the RMA cost J_n with different n versus the original cost J, for the 3D example with the Achlioptas distribution. Contours are evaluated along a 1D direction $\mathbf{s}$ parameterized by κ and centered at a random parameter $\mathbf{u}_0$ in the prior distribution. Red triangles indicate the minimum values of each contour.

show the convergence rate is indeed $\mathcal{O}(1/\sqrt{n})$ for both $\mathbf{u}_n^{\text{MAP}}$ and $J_n^\star$. However, the absolute error of $\mathbf{u}_n^{\text{MAP}}$ is orders of magnitude smaller than $J_n^\star$ for all considered random projections. Also, the relative error in $\mathbf{u}_n^{\text{MAP}}$ decreases much faster than the relative error in $J_n^\star$ for $1 < n < 100$. Therefore a convergence analysis of the randomized cost J_n alone is not adequate for understanding the method efficacy in this range; the additional theory in subsection 3.6.1 is required to characterize solution accuracy for n in the range of interest.

Inversion results from minimizing the RMA cost with different n in the 1D, 2D, and 3D example are shown alongside the true MAP estimate $\mathbf{u}^{\text{MAP}}$ in Figures 3.4 to 3.6. The figures shown are results with $\mathbf{r}$ distributed by the Achlioptas distribution (66% sparse). We see that the original MAP point $\mathbf{u}^{\text{MAP}}$ is well-approximated by the RMA solution $\mathbf{u}_n^{\text{MAP}}$ in all cases with $50 \leq n \leq 100$.

In a different experiment, we consider a 3D example in which only surface observations are available. The parameters are the same as the problem represented by Figure 3.1(c) but

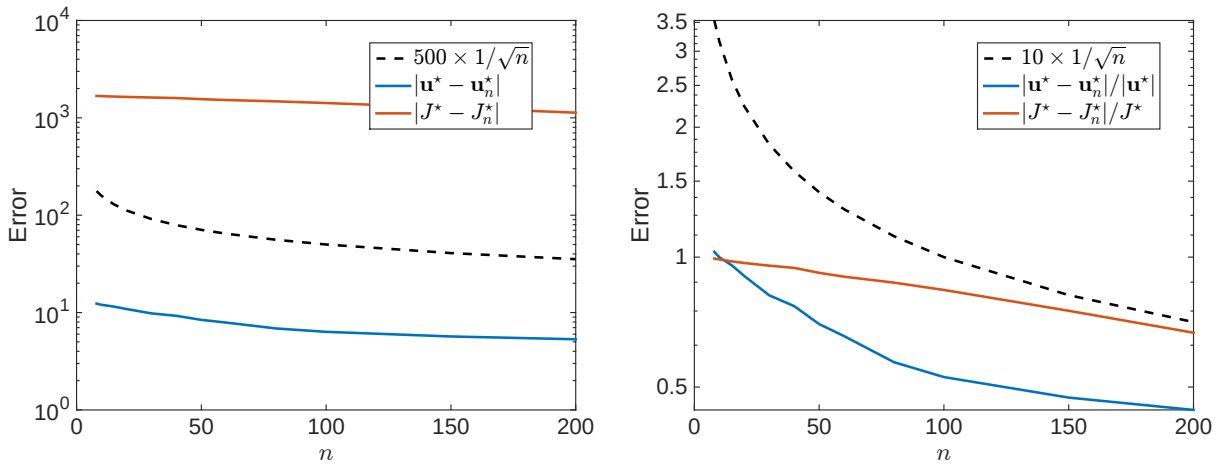

(a) absolute convergence

(b) relative convergence

Figure 3.3: Log-linear plots of absolute errors $|J_n^\star - J^\star|$ and $\left\|\mathbf{u}_n^{\text{MAP}} - \mathbf{u}^{\text{MAP}}\right\|$, relative errors $|J_n^\star - J^\star|/|J^\star|$ and $\left\|\mathbf{u}_n^{\text{MAP}} - \mathbf{u}^{\text{MAP}}\right\| / \left\|\mathbf{u}^{\text{MAP}}\right\|$, and $\mathcal{O}(1/\sqrt{n})$ reference curves show the $\mathcal{O}(1/\sqrt{n})$ convergence rate for both $\mathbf{u}_n^{\text{MAP}}$ and $J_n^\star$ as given by Theorem 4.

the data are now obtained from 901 observations on the surface of the cube (except the bottom surface), and the truth log conductivity is nonzero within the sphere of radius 0.5 centered at the origin as seen in Figure 3.7. Figure 3.8(d) shows the original MAP estimate $\mathbf{u}^{\text{MAP}}$. Compared to the above example the recovery is poorer, but this is expected due to having less observational data. Our interest however is in reducing the computational burden caused by the large data dimension while recovering a reasonable MAP estimation. Subsequently, we compare the RMA MAP point $\mathbf{u}_n^{\text{MAP}}$ to the true MAP point $\mathbf{u}^{\text{MAP}}$ (a minimizer of J). The results in Figure 3.8 show the RMA solutions $\mathbf{u}_n^{\text{MAP}}$ as n increases. As can be seen, with $n = 150$, i.e. a 6-fold reduction in the data misfit dimension, the RMA approximation $\mathbf{u}_{150}^{\text{MAP}}$ is still a good approximation to the original MAP solution $\mathbf{u}^{\text{MAP}}$.

3.7.2 Verification of Theorem 2

Table 3.1 presents results for solving the model problem for the 1D, 2D, and 3D examples with Morozov's criterion, again using the Achlioptas random projection in the randomized misfit approach. We perform several numerical experiments and choose an n

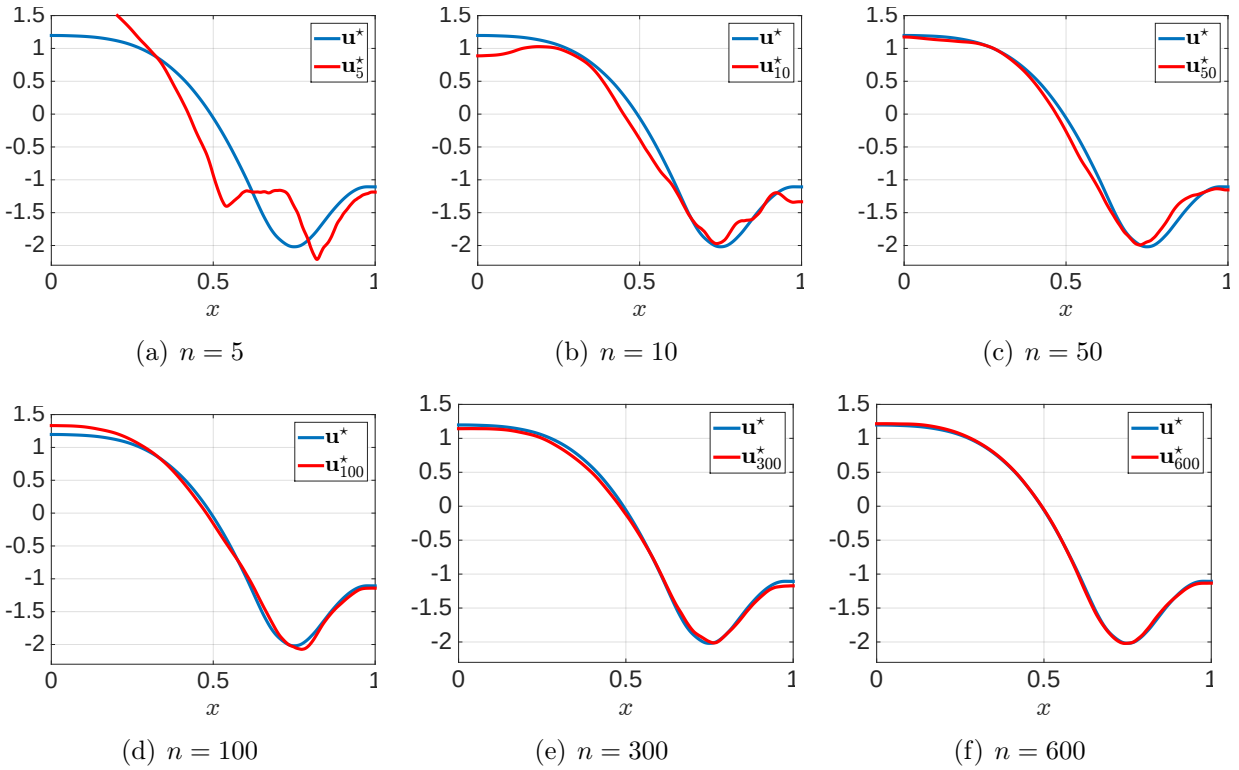

(a) $n = 5$ (b) $n = 10$ (c) $n = 50$

(d) $n = 100$ (e) $n = 300$ (f) $n = 600$

Figure 3.4: 1D elliptic PDE example: Convergence of $\mathbf{u}_n^{\text{MAP}}$ to $\mathbf{u}^{\text{MAP}}$ as n increases. The Achlioptas random projection (66% sparse) is used for $\boldsymbol{\Sigma}$ and the original data dimension is $N = 1025$.

for each example such that Morozov's principle is met for $J_n\left(\mathbf{u}_n^{\text{MAP}}\right)$ with $\tau' \approx 1$. We then compute the corresponding ranges for τ that are guaranteed with probability at least $p \geq 1 - e^{-\beta}$, after choosing an acceptable cost distortion tolerance of $\varepsilon = 0.5$ and β as large as possible from (3.17). As can be seen, evaluating $\mathcal{J}\left(\mathbf{u}_n^{\text{MAP}}\right)$ gives a τ within the specified range, which satisfies Morozov's criterion. That is, even for moderately small values of n, if the discrepancy principle is satisfied for $J_n\left(\mathbf{u}_n^{\text{MAP}}\right)$, then the discrepancy principle is also satisfied for $J\left(\mathbf{u}_n^{\text{MAP}}\right)$. Thus $\mathbf{u}_n^{\text{MAP}}$ is a discrepancy principle-satisfying solution for both the randomized reduced misfit dimension problem (3.3) and the original problem (2.8).

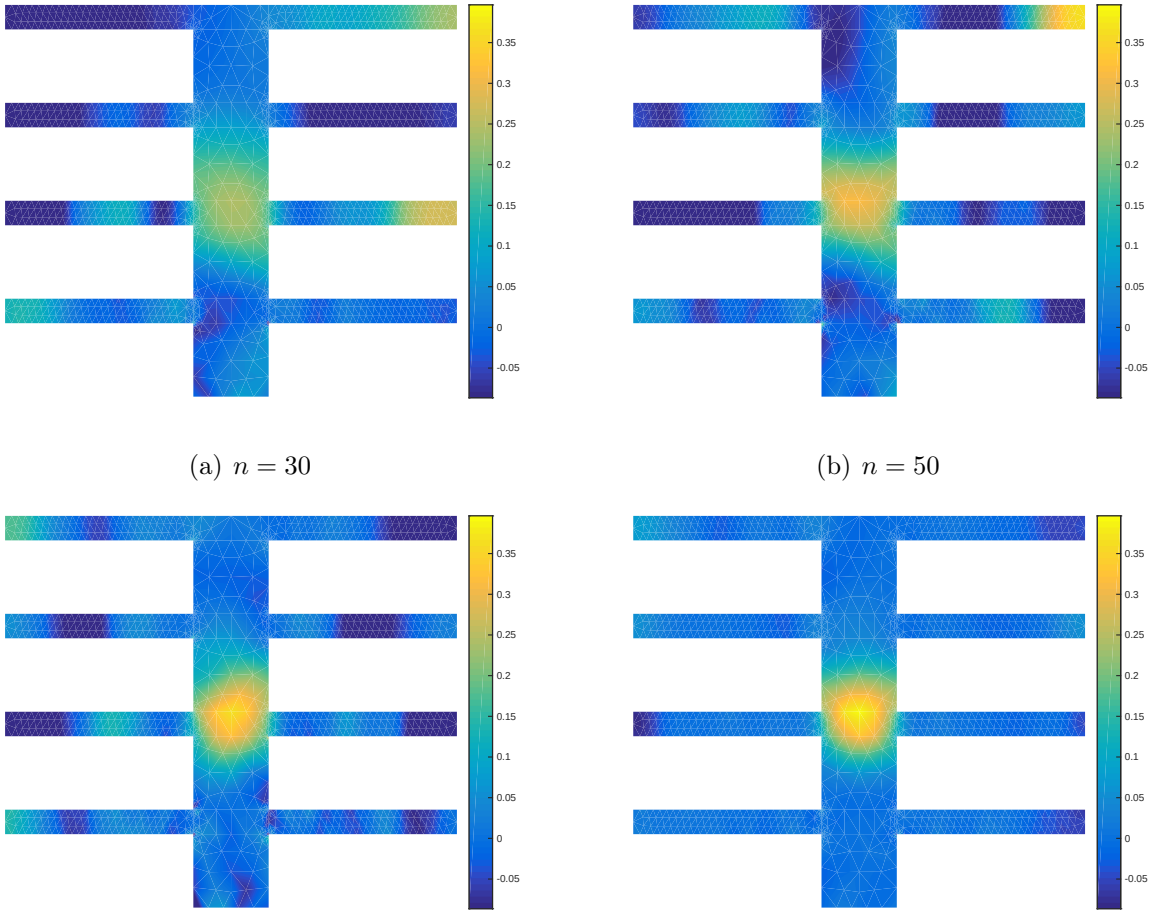

(a) $n = 30$ (b) $n = 50$

(c) $n = 100$ (d) $\mathbf{u}^{\text{MAP}}$

Figure 3.5: 2D elliptic PDE example: Convergence of $\mathbf{u}_n^{\text{MAP}}$ to $\mathbf{u}^{\text{MAP}}$ as n increases. The Achlioptas random projection (66% sparse) is used for $\boldsymbol{\Sigma}$ and the original data dimension is $N = 1333$.

Table 3.1: Verification of Morozov's discrepancy principle for the RMA solution with $\varepsilon = 0.5$.

	N	n	$\mathcal{J}_n\left(\mathbf{u}_n^{\text{MAP}}\right)$	τ'	$\left[\frac{\tau'}{1+\varepsilon}, \frac{\tau'}{1-\varepsilon}\right]$	p	$\mathcal{J}\left(\mathbf{u}_n^{\text{MAP}}\right)$	τ
1D	1025	100	1220	1.190	$[0.793, 2.380]$	95.6%	1074	1.048
2D	1333	50	1240	0.930	$[0.620, 1.860]$	79.0%	1406	1.055
3D	2474	75	2646	1.070	$[0.713, 2.139]$	90.4%	3928	1.588

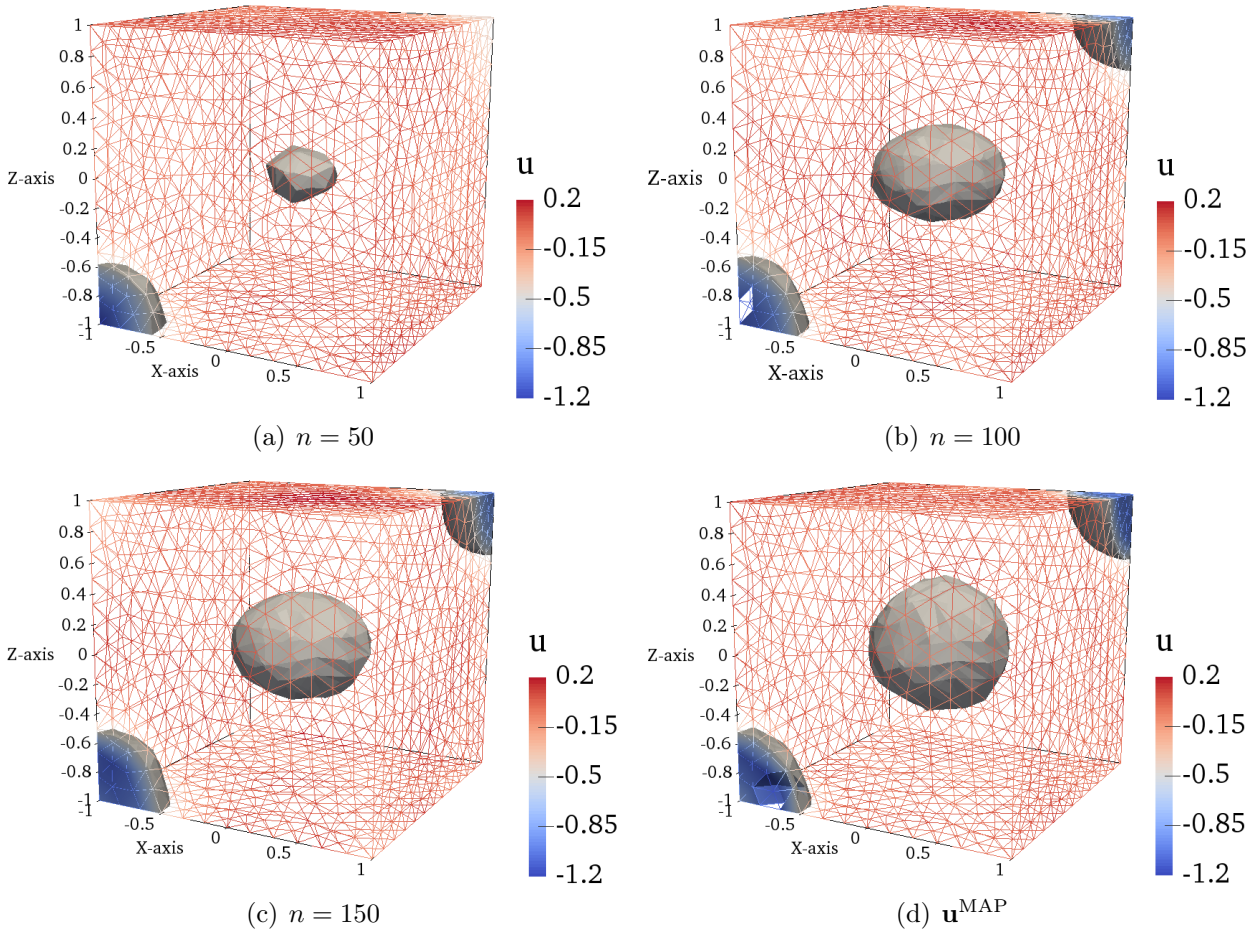

(a) $n = 50$ (b) $n = 100$

(c) $n = 150$ (d) $\mathbf{u}^{\text{MAP}}$

Figure 3.6: 3D elliptic PDE example: Convergence of $\mathbf{u}_n^{\text{MAP}}$ to $\mathbf{u}^{\text{MAP}}$ as n increases. The Achlioptas random projection (66% sparse) is used for $\boldsymbol{\Sigma}$ and the original data dimension is $N = 2474$.

3.7.3 Scalability and performance

We study the effect of the RMA reduced misfit dimension n on the overall algorithmic scalability of solving large-scale PDE-constrained inverse problems with high observational data dimensions. Specifically, we wish to show that RMA convergence is independent of r, the level of parameter information from the data (see subsection 3.6.3). Figure 3.9 compares singular values of the prior-preconditioned misfit Hessian $\mathbf{H}$ corresponding to the original problem cost J to the singular values of the surrogate prior-preconditioned misfit Hessian $\tilde{\mathbf{H}}$ corresponding to the surrogate RMA cost J_n for $n = 30, 50$, and 100. The Hessians are each

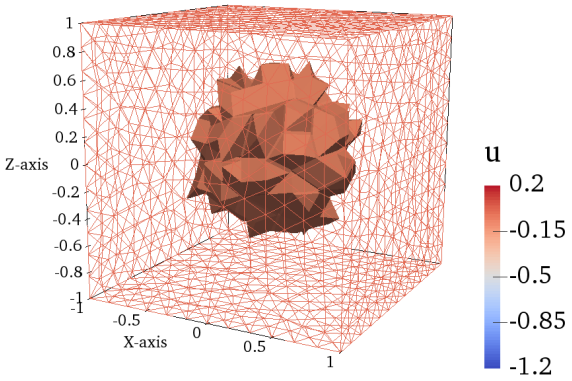

Figure 3.7: Truth $\mathbf{u}$ for 3D experiment with surface observations: The same number of mesh elements as in Figure 3.1(c) is used but now the synthetic parameter is a single sphere, and observational data is obtained from $N = 901$ mesh points on the top and side surfaces of the cube.

evaluated at the same random point chosen from the prior. Note that the RMA reduced misfit dimension n is a hard upper bound on the numerical rank of $\tilde{\mathbf{H}}$, where numerical rank is the number of singular values greater than some threshold $\epsilon \leq 1$. Note also the faster spectral decay of the singular values of $\tilde{\mathbf{H}}$ compared to $\mathbf{H}$. Faster decay demonstrates that the action of $\tilde{\mathbf{H}}$ on a vector can be captured with fewer modes than the action of $\mathbf{H}$, resulting in decreased overall work complexity as detailed in subsection 3.6.3. Similar behavior is observed when the Hessians are evaluated at zero, at another random point, and at the full MAP point $\mathbf{u}^{\text{MAP}}$, thus the plots are omitted.

Tables 3.2 and 3.3 respectively present algorithmic performance of the original 2D and 3D elliptic problem compared to ten trials of the RMA with various distributions. To investigate the effect of choosing the randomized misfit dimension $n < r \leq N$ on work complexity, n is chosen to be 50 for the 2D example where $N = 1333$, and $n = 300$ for the 3D example where $N = 2474$. The Newton-CG solver is terminated when the gradient, cost, or step size falls below a tolerance of 10^{-6}, or after 200 Newton iterations for the 2D example and 15 Newton iterations for the 3D example. Each trial uses a different random number generator seed. We observe that on average, using the RMA *with any distribution* results in

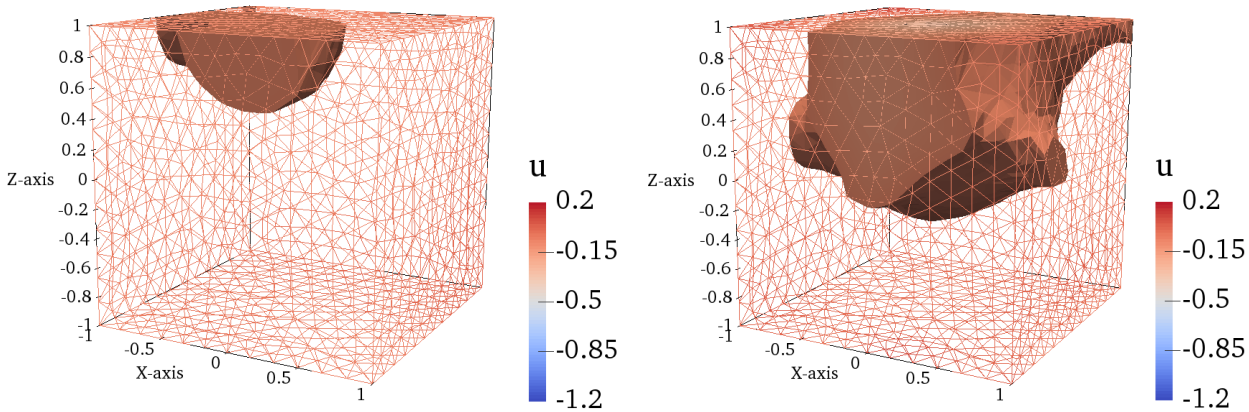

(a) $n = 10$ (b) $n = 50$

(c) $n = 150$ (d) $\mathbf{u}^\star$ (solution of the full cost)

Figure 3.8: 3D elliptic PDE example with surface observations: Convergence of $\mathbf{u}_n^{\text{MAP}}$ to $\mathbf{u}^{\text{MAP}}$ as n increases. The MAP solution is nearly approximated with an RMA reduced misfit dimension of $n = 150$ (a 6-fold reduction from the $N = 901$ observational data points on the surface). The Achlioptas random projection (66% sparse) is used for $\mathbf{\Sigma}$.

close to half as many PDE solves compared to solving the full deterministic problem in the 2D example, and 14 to 28 percent fewer PDE solves in the 3D example. There appears to be little demonstrable difference in the quality of the reconstruction as well; all experiments are successful in reconstructing the Gaussian blob of high conductivity. Further investigation on very large problems ($r = \mathcal{O}(1000)$ or larger) is needed.

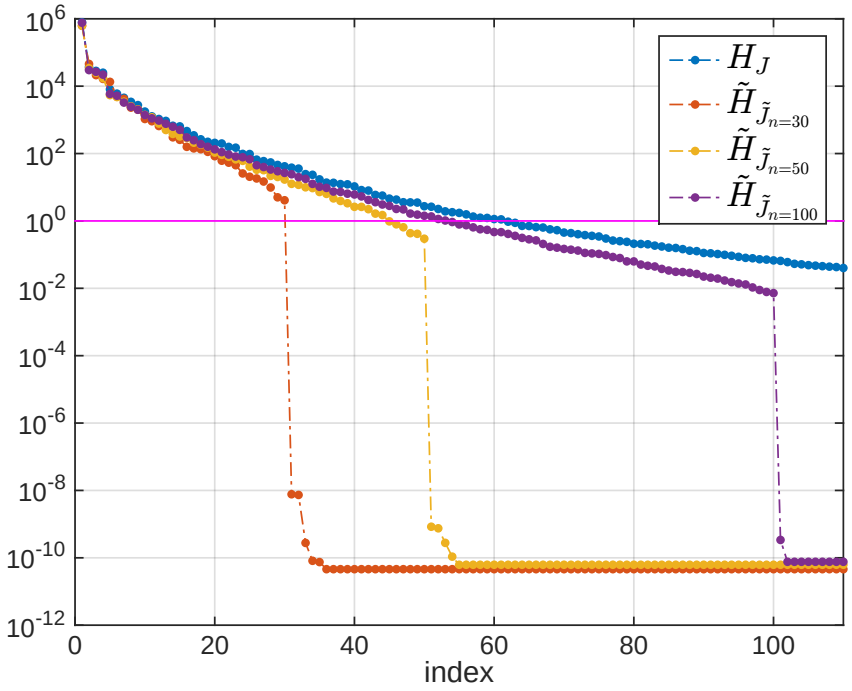

Figure 3.9: Log-linear spectra of the prior-preconditioned misfit Hessian for the 2D elliptic example. Each spectrum is evaluated at at the same random parameter $\mathbf{u}$ drawn the prior. Numerical rank is the number of singular values greater than some threshold $\epsilon \leq 1$. The misfit vector dimension (N in the original cost or n in the RMA cost) is a hard upper bound on the numerical rank of the prior-preconditioned misfit Hessian. The misfit dimension N for the original problem is 1333.

Table 3.2: Comparison of cost complexity measured in total number of PDE solves needed to resolve the 2D elliptic problem with a Gauss-Newton solver. AVG is average over ten trials. Convergence tolerances for the cost, gradient, and step size are set to 10^{-6} and the maximum number of Newton iterations allowed is 200.

#PDE SOLVES	Trial 1	Trial 2	Trial 3	Trial 4	Trial 5	Trial 6	Trial 7	Trial 8	Trial 9	Trial 10	**AVG**
Deterministic	2423	2423	2423	2423	2423	2423	2423	2423	2423	2423	**2423.0**
Rademacher	1303	1298	1273	1225	1279	1252	1270	1267	1252	1274	**1269.3**
Achlioptas	1149	1253	1293	1266	1253	1245	1267	1262	1231	1254	**1247.3**
95-percent sparse	1287	1272	1230	1273	1235	1217	1252	1248	1293	1238	**1254.5**
99-percent sparse	1212	1243	1245	1247	1250	1263	1268	1226	1218	1274	**1244.6**
Gaussian	1237	1258	1224	1226	1240	1273	1278	1255	1247	1234	**1247.2**
Uniform	1217	1244	1233	1242	1241	1264	1259	1262	1275	1248	**1248.5**

3.8 Discussion

The focus of this work is on the framework and resulting analysis of the method. Numerical results are presented for a medium size ($N = \mathcal{O}(10^3)$) synthetic steady-state

Table 3.3: Comparison of cost complexity measured in total number of PDE solves needed to resolve the 3D elliptic problem with a Gauss-Newton solver. AVG is average over ten trials. Convergence tolerances for the cost, gradient, and step size are set to 10^{-6} and the maximum number of Newton iterations allowed is 15.

#PDE SOLVES	Trial 1	Trial 2	Trial 3	Trial 4	Trial 5	Trial 6	Trial 7	Trial 8	Trial 9	Trial 10	**AVG**
Deterministic	331	331	331	331	331	331	331	331	331	331	**331.0**
Rademacher	249	307	383	219	263	285	303	235	217	253	**271.4**
Achlioptas	259	287	263	257	283	203	259	223	319	255	**260.8**
95-percent sparse	279	273	221	231	285	241	255	313	217	367	**268.2**
99-percent sparse	277	321	271	249	279	395	273	223	281	279	**284.8**
Gaussian	219	223	323	199	257	233	229	257	211	225	**237.6**
Uniform	247	285	317	285	221	271	251	241	201	249	**256.8**

thermal conductivity example in 1D, 2D, and 3D and different distributions for numerical justification of theoretical results and illustration of the method. The next chapter extends the method to a transient groundwater inverse problem and presents numerical results with larger scale data ($N = \mathcal{O}(10^7)$.

Results presented in the current chapter are valid for nonlinear inverse problems with the exception of part (ii) in Theorem 4 (which only applies to linear forward models). A result is expected to also be true for nonlinear inverse problems, and this is under investigation.

Chapter 4

The randomized geostatistical approach: Extension of RMA to big geostatistical data

This chapter is adapted from a reduced subset of material published as a research article in [88]. It is an application of the randomized misfit approach (RMA) introduced in the previous chapter to a geostatistical inversion method that is prevalent in geoscience applications, particularly in subsurface characterization for hydrogeology applications. The applied method is referred to as the randomized geostatistical approach (RGA). It is included in this dissertation because it demonstrates an extension of the RMA, as a strategy for reducing the impact of big data, to address a known computational limitation of the widely used geostatistical approach (GA) [74, 75, 127] and its subsequent extensions [73, 84] in solving geostatistical inverse problems with both high-dimensional parameter spaces *and* high-dimensional data. The contributions of the author to the multi-authored article included the development of the RGA method, the computational implementation of the RGA method and the reference method, generating some of the inversion results, and writing part of the manuscript. The method was developed during the author's internship in the Los Alamos National Laboratory Computational Earth Sciences Group, within the Subsurface Flow and Transport team.

Note that the motivation for constructing the RMA and its analysis in the previous chapter is based on an observation that state-of-the-art methods are not independent of the effective level of information in the data—the rank r of the prior-preconditioned Gauss-Newton misfit Hessian of the negative log-likelihood. State-of-the-art denotes methods that efficiently use second-order derivative information, possibly via a matrix-free construction of

the Hessian-action by solving the linearized forward and adjoint PDE models.

In practice, domain scientists who need to solve large-scale inverse problems often access the forward solver as a black box, and may not have access to the linearized PDE models. Or, they may not have the resources to do the time-consuming work of developing the linearized PDE solvers. Thus, the method in this chapter extends the RMA to the RGA, a new black-box method for geostatistical inversion problems with big data and high-dimensional parameter spaces.

A necessarily different complexity analysis is given in this chapter in order to fairly assess the efficiency of the RGA against existing geostatistical inversion methods. Computational costs of implementing the inversion methods in this chapter are given using the standard asymptotic number of numerical operations. Memory costs are also assessed, since geostatistical inversion methods can be memory bound due to their explicit construction of matrices. Note that *this chapter uses big $\mathcal{O}$ notation for denoting the computational complexity in floating point operations per second (FLOPS), and for denoting the memory complexity in bytes.* The RMA analysis in the previous chapter uses $\mathcal{O}$ for denoting the complexity in number of PDE solves, based on assumed use of the state-of-the-art methods described above.

4.1 Motivation for a data-driven randomized geostatistical approach (RGA)

Geostatistical inversion methods (often referred to methods for *inverse modeling* in the geosciences) are data-driven methods for the estimation of a spatially-varying field $\mathbf{u}(x)$ (the unknown parameter). The geostatistical approach is an empirical Bayesian algorithm that is commonly used for solving inverse problems in the geosciences [73, 84, 127].

It is widely used because it is seen as a practical method that also has the ability to quantify uncertainty [127]. Thus, use of the geostatistical approach is found in many various

applications, ranging from subsurface characterization [63, 144, 145, 152] to modeling land-atmosphere interactions in earth systems sciences [98].

The term *geostatistical* indicates that the unknown $\mathbf{u}$ is modeled as a random field with some unknown spatial correlation. Thus, the first step of inverse modeling involves elicitation of the prior model for the random parameter field $\mathbf{u}$, using the data (the stage of estimating *structural parameters* to specify the prior model). Then, the data is used with the forward model and the prior model to infer the unknown parameter and quantify the uncertainty (the stage of estimating the parameter $\mathbf{u}$, conditioned on the data) [75, 127].

4.2 Addressing complexity issues in geostatistical inversion with the RGA

Efficient state-of-the-art Bayesian inversion methods avoid complexity issues that arise from explicit construction of a dense prior covariance matrix, by considering priors for which the square-root is already known (such as the inverse of a discretized differential operator) [20, 25, 47, 127].

However, the matrix square root is not known for arbitrary covariance matrices, and this assumption is restrictive for solving geostatistical problems [127]. It is common in the geosciences to model the prior covariance matrix with entries arising from one of several candidate generalized covariance functions [127]. Therefore the RGA relies on a different, yet still computationally-efficient, prior covariance construction than one used in the RMA. This construction accommodates arbitrary generalized covariance functions and makes the RGA method practical for geosciences problems.

In particular, the permeability of a porous medium is of great importance for predicting flow and transport of fluids and contaminants in the subsurface [32, 33, 136]. A well-understood distribution of permeability heterogeneity can be crucial for many different subsurface applications such as (1) forecasting production performance of geothermal

reservoirs, (2) extracting oil and gas, (3) estimating pathways of subsurface contaminant transport, and many others.

Various hydraulic inversion methods have been proposed and developed to obtain subsurface permeability [32, 33, 72, 104, 105, 136, 155], of which geostatistical inversion is the most widely used [72, 74, 76, 145, 155]. The Bayesian geostatistical approach (GA) is used more other subsurface inverse modeling methods, as it provides uncertainty estimates, and is compatible with data assimilation approaches [63, 144, 145, 152]. However, as pointed out in [144] and [63], one drawback of the geostatistical approach is its high computational cost when the number of observations is large and the model is highly parameterized. In recent years, with the popularization of regularization techniques [45, 137], the number of model parameters (the dimension of the mesh for the estimated permeability) has increased [61]. These highly parameterized models have great potential for characterizing subsurface heterogeneity [61, 138]. Meanwhile, as the theory and computational tools related to characterization of geologic subsurface prepare for the new era of "big data", many existing methodologies are facing the challenges of handling large number of unknown model parameters and large number of observations. Therefore, it is important to address the theoretical and computational issues of the geostatistical inversion methods.

The costs related to application of the geostatistical inversion methods comes from two parts: the computational cost and the memory cost. A number of computational techniques have been proposed and developed to alleviate the expensive costs of both the computation [8, 84, 87, 92, 93, 126] and memory [73, 84, 110, 126, 130]. Among those references, some target for both computation and memory costs [73, 84, 126].

In particular, one major direction to reduce the computational cost is based on the subspace approximation, i.e., solving a small-size approximated problem residing in a lower-dimensional subspace to save the computational cost. Several types of subspaces have been utilized in the references including principle components subspace [73, 84, 138], Krylov sub-

space [87, 93, 126], subspace spanned by reduced-order model [93], hierarchical matrix decomposition [8, 126], and active subspace [37].

In geostatistical inversion methods, a majority of the memory is used in storing the matrices, such as Jacobian matrix and covariance matrix [73, 84]. In situations with a large number of measurements and model parameters, it is prohibitively expensive to store these matrices. To overcome the known memory issues, matrix-free or low-rank approximation methods have been developed. Specifically, in the work of [73] and [84], a matrix-free Jacobian is developed to approximate the multiplication of Jacobian matrix with a vector by finite-difference operations.

To further reduce the storage cost of the covariance matrices, other various computational methods have been developed. [110] developed a FFT-based geostatistical inversion method, which is restricted to intrinsic cases on regular equispaced grids, but it only needs to store the first line of a covariance matrix. Ensemble Kalman filters (EnKFs)-like methods for geostatistical parameter inference have also been developed to avoid the storage and handling of large covariance matrix [130]. Low-rank matrix approximation-based techniques have also been employed, such as hierarchical decomposition [8, 126] and principal component decomposition [73, 84]. In recent work a computationally efficient method to generate a preconditioner is developed by using Generalized Eigenvalue Decomposition and the Sherman-Morrison-Woodbury formula [85]. Another popular computational method to reduce he impact of big data on computational cost is based on extraction of temporal moments from redundant data [35, 109, 153, 156].

4.3 A big data geostatistical inverse problem: inferring log transmissivity from hydraulic head data

To demonstrate the applicability of the RGA method to geostatistical inverse problem, this chapter extends the forward elliptic PDE in (2.4) to the transient groundwater flow

model, where $\mathbf{w}$ is hydraulic head (the distributed state), bd is the high-dimensional ($\mathcal{O}(10^5)$ or larger) noisy data observations of the head, $\mathbf{u} = \mathbf{T}$ is the log transmissivity (the distributed parameter) and $\mathbf{F}(\mathbf{u})$ is the forward operator mapping from the log transmissivity to the hydraulic head and $\boldsymbol{\eta}$ is the Gaussian additive noise with the same model as in (2.2).and

4.4 Geostatistical approach for inverse modeling

4.4.1 Equations for the standard geostatistical approach (GA)

To further account for the errors in the observations and the model, we follow the work in [73] and [84], and employ the generalized least squares that weights the data misfit and regularization terms using covariance matrices

$$\begin{aligned}\hat{\mathbf{u}} &= \arg\min_{\mathbf{u}} \{g(\mathbf{u})\} \\ &= \arg\min_{\mathbf{u}} \left\{ \|\mathbf{d} - f(\mathbf{u})\|_R^2 + \lambda \mathcal{R}(\mathbf{u}) \right\}, \end{aligned} \tag{4.1}$$

The weighted data misfit and regularization terms are defined as

$$\|\mathbf{d} - f(\mathbf{u})\|_{\mathbf{R}}^2 = (\mathbf{d} - f(\mathbf{u}))^T \mathbf{R}^{-1} (\mathbf{d} - f(\mathbf{u})), \tag{4.2}$$

and

$$\mathcal{R}(\mathbf{u}) = (\mathbf{u} - (\mathbf{X}\boldsymbol{\beta}))^T \mathbf{Q}^{-1} (\mathbf{u} - (\mathbf{X}\boldsymbol{\beta})), \tag{4.3}$$

where $\mathbf{X}$ is a drift (trend) matrix, $\mathbf{Q}$ is the covariance matrix of the model parameters and $\mathbf{R}$ the prior covariance matrix with entries defined by a generalized covariance kernel [73, 127].

With the Jacobian matrix, $\mathbf{H}$, of the forward modeling operator f defined as

$$\mathbf{H} = \frac{\partial f}{\partial \mathbf{u}}\Big|_{\mathbf{u}=\bar{\mathbf{m}}}, \tag{4.4}$$

we will have the linearized function of the forward modeling operator f as

$$f(\hat{\mathbf{m}}) \approx f(\bar{\mathbf{m}}) + \mathbf{H}(\hat{\mathbf{m}} - \bar{\mathbf{m}}), \tag{4.5}$$

where $\hat{\mathbf{m}}$ is the current solution and $\bar{\mathbf{m}}$ is the previous solution.

According to [76] and [108], the current solution $\hat{\mathbf{m}}$ in (4.5) is given as

$$\hat{\mathbf{m}} = \mathbf{X}\boldsymbol{\beta} + \mathbf{Q}\mathbf{H}^T\boldsymbol{\xi}, \tag{4.6}$$

where the vectors of $\boldsymbol{\beta}$ and $\boldsymbol{\xi}$ are solutions to the linear system below

$$\begin{bmatrix} \mathbf{H}\mathbf{Q}\mathbf{H}^T + \mathbf{R} & \mathbf{H}\mathbf{X} \\ (\mathbf{H}\mathbf{X})^T & \mathbf{0} \end{bmatrix} \begin{bmatrix} \boldsymbol{\xi} \\ \boldsymbol{\beta} \end{bmatrix} = \begin{bmatrix} \mathbf{y} - f(\bar{\mathbf{m}}) + H\bar{\mathbf{m}} \\ \mathbf{0} \end{bmatrix}. \tag{4.7}$$

4.4.2 Existing approaches and current complexity challenges in geostatistical inversion

The most computational and memory intensive parts of solving the cokriging system (4.7) of the GA comes from both the construction of the Jacobian matrix of $\mathbf{H}$ and the matrix products of Jacobian, particularly $\mathbf{HQ}$ in (4.7). Various techniques are employed to address these issues. In [73] and [84], the principal component geostatistical approach (PCGA), a seminal computational method in solving the geostatistical method, is proposed and developed. To bypass the expensive explicit construction of the Jacobian matrix, a finite difference scheme is employed to approximate a generic Jacobian-vector multiplication of $H\mathbf{x}$, i.e.

$$\mathbf{H}\mathbf{x} \approx \frac{1}{\delta}\left[f(\mathbf{x} + \delta\mathbf{x}) - f(\mathbf{x})\right], \tag{4.8}$$

where $\mathbf{x}$ is a N-dimensional vector and δ is the finite difference interval.

Furthermore, a low-rank approximation of the covariance matrix $\mathbf{Q}$ is deployed

$$\mathbf{Q} \approx \mathbf{Q}_{\mathbf{n}_{\mathrm{PCGA}}} = \mathbf{Z}^T\,\mathbf{Z} = \sum_{i=1}^{n_{\mathrm{PCGA}}} \boldsymbol{\zeta}_i\,\boldsymbol{\zeta}_i^T, \tag{4.9}$$

where $\mathbf{Q}_{\mathbf{n}_{\mathrm{PCGA}}}$ is the rank-n_{PCGA} approximation of the covariance matrix $\mathbf{Q}$, $\mathbf{Z}$ is the square root of $\mathbf{Q}_{\mathbf{n}_{\mathrm{PCGA}}}$ using the eigendecomposition decomposition, and $\boldsymbol{\zeta}_i$ is the i^{th} column vector of $\mathbf{Z}$. Based on (4.8) and (4.9), the expensive matrix-matrix operations of $\mathbf{HQ}$ and $\mathbf{HQH}^T$

can be re-formulated as matrix-vector operations

$$\mathbf{HQ} \approx \mathbf{HQ}_{n_{\mathrm{PCGA}}} = \mathbf{H} \sum_{i=1}^{n_{\mathrm{PCGA}}} \boldsymbol{\zeta}_i \boldsymbol{\zeta}_i^T = \sum_{i=1}^{n_{\mathrm{PCGA}}} (\mathbf{H}\boldsymbol{\zeta}_i)\boldsymbol{\zeta}_i^T, \tag{4.10}$$

$$\mathbf{HQH}^T \approx \mathbf{HQ}_{\mathbf{n}_{\mathrm{PCGA}}}\mathbf{H}^T = \sum_{i=1}^{n_{\mathrm{PCGA}}} (\mathbf{H}\boldsymbol{\zeta}_i)(\mathbf{H}\boldsymbol{\zeta}_i)^T. \tag{4.11}$$

Another computational technique to reduce the expensive cost of matrix products of Jacobian matrix is to employ the hierarchical representation of the covariance matrix [126]. The hierarchical representation of a matrix is to split the given matrix into a hierarchy of rectangular blocks and approximate each of the blocks by a low-rank matrix [12, 14, 126].

With the Jacobian matrix obtained approximately, two main categories of numerical methods have been developed to solve the above linear system in (4.7). One is based on direct solvers [73, 84] and the other is based on the iterative solvers [93, 108, 126]. Direct solvers are mostly used in the situations when size of problems ranges from small to medium scale and the system matrix in (4.7) can be therefore explicitly constructed [73, 84]. As pointed out in [84], direct solvers can be used to solve dense linear systems of dimension up to $N \sim \mathcal{O}(10^4)$. On the other hand, for large-scale problems (dimension $N > \mathcal{O}(10^4)$), matrix-free representations can be used, and Krylov-subspace based iterative solvers such as GMRES [125] or MINRES [112] are favored over direct methods to solve (4.7) [93, 126].

Utilization of direct solvers or iterative solvers to solve the problem in (4.7) can be memory bound [73, 84]. Such a limitation can significantly reduce the computational efficiency when a large number of measurements are available. In particular, it can be observed from (4.7) that the number of the equations is on the same order as the number of the measurements. In many subsurface applications, it is increasingly common to calibrate models using a very large number of observations (e.g., $\mathcal{O}(10^7)$ or more). Employing the computational techniques mentioned above to solve linear systems of such a scale is beyond the computability and storage capacity of any methods regardless of the choice of direct or

iterative solvers. As pointed out in [73], the developed computational methodologies work best for problems with a modest number of observations. Therefore, there is a need to develop computational methods that would allow an efficient solution of (4.7) with a large number of measurements.

There have been some publications addressing this important need for data reduction to reduce computational and storage costs. In [85], where the PCGA was extended to handle data-intensive inverse problems by constructing a fast preconditioner of the cokriging matrix leading to accelerated iterative matrix inversion. Specifically, by employing similar notations to [85], $\mathbf{\Psi} = \mathbf{HQH}^T + \mathbf{R}$, $\mathbf{\Phi} = \mathbf{HX}$, and $\mathbf{\Sigma} = \mathbf{\Phi}^T\mathbf{\Psi}^{-1}\mathbf{\Phi}$, the exact inversion of the system matrix in (4.7) can be given as

$$\begin{bmatrix} \mathbf{HQH}^T + \mathbf{R} & \mathbf{HX} \\ (\mathbf{HX})^T & \mathbf{0} \end{bmatrix}^{-1} = \begin{bmatrix} \mathbf{\Psi} & \mathbf{\Phi} \\ \mathbf{\Phi}^T & \mathbf{0} \end{bmatrix}^{-1} = \begin{bmatrix} \mathbf{\Psi}^{-1} - \mathbf{\Psi}^{-1}\mathbf{\Phi}\mathbf{\Sigma}^{-1}\mathbf{\Phi}^T\mathbf{\Psi}^{-1} & \mathbf{\Psi}^{-1}\mathbf{\Phi}\mathbf{\Sigma}^{-1} \\ \mathbf{\Sigma}^{-1}\mathbf{\Phi}^T\mathbf{\Psi}^{-1} & -\mathbf{\Sigma} \end{bmatrix}. \quad (4.12)$$

By further employing Sherman-Morrison-Woodbury formula and Generalized Eigenvalue Decomposition (GED) [50], the dominant cost of solving $\mathbf{\Psi}^{-1}$ can be significantly reduced by low-rank approximation, while the resulting accuracy is well maintained. It has been pointed out in [85] that the GED can be efficiently implemented by using either sequential Lanczos-based method or parallelized randomized SVD method. Hence, [85] conclude that such a computational technique can be either used as a direct solver or as a preconditioner for iterative solvers in solving (4.7). In the numerical examples therein, the authors estimated the hydraulic conductivity field of a laboratory-scale sand box using 6 million MRI-scanned tracer concentration observations directly within a reasonable time.

Another popular computational method to reduce the data size and computational cost is based on extraction of temporal moments from large data. Researchers have deployed such a technique to various data sets such as transient pressure [153, 156] and concentration breakthrough curves [35, 109]. Temporal-moment based data reduction methods have been proved to be very efficient in reducing the data. Their major drawback, however, is that the

system response must be integrable (except when using truncated temporal moments), so they do not work for dynamic systems with fluctuating drivers.

The next section outlines the RGA. Similar to the RMA, the RGA method has no restrictions on what mathematical properties the time series or data must have.

4.5 The randomized geostatistical approach (RGA)

The misfit function of the randomized geostatistical inversion is given by

$$\hat{\mathbf{u}} = \arg\min_{\mathbf{u}} \left\{ \|\boldsymbol{\Sigma}\mathbf{d} - \boldsymbol{\Sigma} f(\mathbf{u})\|_2^2 + \lambda \mathcal{R}(\mathbf{u}) \right\}, \tag{4.13}$$

where $\boldsymbol{\Sigma} \in \mathbb{R}^{n \times N}$ is the random projection matrix and $n << N$ is the tunable reduced dimension.

With the new misfit function defined in (4.13) and following a similar derivation as in the previous section, the RGA cokriging system is the randomized linear system below

$$\begin{bmatrix} \boldsymbol{\Sigma}\mathbf{H}\mathbf{Q}\mathbf{H}^T\boldsymbol{\Sigma}^T + \mathbf{R} & \boldsymbol{\Sigma}\mathbf{H}\mathbf{X} \\ (\boldsymbol{\Sigma}\mathbf{H}\mathbf{X})^T & \mathbf{0} \end{bmatrix} \begin{bmatrix} \boldsymbol{\xi} \\ \boldsymbol{\beta} \end{bmatrix} = \begin{bmatrix} \boldsymbol{\Sigma}(\mathbf{y} - f(\bar{\mathbf{m}}) + \mathbf{H}\bar{\mathbf{m}}) \\ 0 \end{bmatrix}. \tag{4.14}$$

Note that we must specify $\mathbf{R}$. As discussed above, the forward modeling can be formulated as

$$\boldsymbol{\Sigma}\mathbf{h} = \boldsymbol{\Sigma} f(\mathbf{T}) + \boldsymbol{\Sigma}\boldsymbol{\varepsilon}, \tag{4.15}$$

we can therefore derivative the data covariance matrix $\mathbf{R}$ in (4.14) as

$$\mathbf{R} = \mathbb{E}[\boldsymbol{\Sigma}\boldsymbol{\varepsilon}(\boldsymbol{\Sigma}\boldsymbol{\varepsilon})^T] = \boldsymbol{\Sigma}\mathbb{E}[(\mathbf{h} - f(\mathbf{T}))(\mathbf{h} - f(\mathbf{T}))^T]\boldsymbol{\Sigma}^T = \boldsymbol{\Sigma}\mathbf{R}\boldsymbol{\Sigma}^T. \tag{4.16}$$

With the randomized linear system given in (4.14) and the covariance matrix in (4.16), we will have the corresponding solution iterate, which shares a similar expression to the one given in (4.6)

$$\hat{\mathbf{m}} = \mathbf{X}\boldsymbol{\beta} + \mathbf{Q}\mathbf{H}^T\boldsymbol{\Sigma}^T\boldsymbol{\xi}. \tag{4.17}$$

Correspondingly, the posterior covariance matrix can be derived similar to [73]

$$\mathbf{V} = \mathbf{Q} - \mathbf{F}, \tag{4.18}$$

where

$$\mathbf{F} = \mathbf{X}\boldsymbol{\beta} + \mathbf{Q}\mathbf{H}^T\boldsymbol{\Sigma}^T\boldsymbol{\xi}^T. \tag{4.19}$$

The results here use the Gaussian random projection matrix $\boldsymbol{\Sigma} \in \mathbb{R}^{n\times N}$ described in the previous chapter, which was shown numerically to be equally effective as other random projections, when applied to problems with dense data.

Both direct linear solvers and iterative solvers can be used to solve the RGA cokriging equations (4.14).

4.6 Computational complexity analysis

To better understand the cost of our new randomized geostatistical inversion algorithm, we provide both the computational and memory cost analysis of the RGA method. To set up the problem, we assume that the number of model parameters is $\tilde{m}$, the number of observations is $\tilde{N}$, hence the size of the Jacobian matrix $\mathbf{H} \in \mathbb{R}^{\tilde{N}\times\tilde{m}}$ and the covariance matrix $\mathbf{Q} \in \mathbb{R}^{\tilde{m}\times\tilde{m}}$. We also assume the rank of the sketching matrix is n according to random matrix theory. The drift matrix $\mathbf{X} \in \mathbb{R}^{\tilde{m}\times\tilde{p}}$. As a reference method, we select the method of the PCGA, which is developed in [73] and [84].

4.6.1 Computational cost

Considering most of the numerical operations the RGA method involve only matrix and vector operations, we use the floating point operations per second (FLOPS) and the big-$\mathcal{O}$ notation to quantify the computational cost [50]. In numerical linear algebra, BLAS operations are categorized into three levels. Level-1 operations involve an amount of data and arithmetic that is linear in the dimension of the operation. Those operations involving

a quadratic amount of data and a quadratic amount of work are Level-2 operations [50]. Following this notation and given a vector of length N and a matrix size of $N \times N$, vector dot-product, addition and subtraction are examples of BLAS Level-1 operations (BLAS 1). It involves $\mathcal{O}(N)$ amount of data and $\mathcal{O}(N)$ amount of arithmetic operations. Matrix-vector multiplication is a BLAS Level-2 operation (BLAS 2) and it involves $\mathcal{O}(N^2)$ amount of data and $\mathcal{O}(N^2)$ amount of arithmetic operations. Matrix-matrix multiplication is a BLAS Level-3 operation (BLAS 3) and it involves $\mathcal{O}(N^2)$ amount of data and $\mathcal{O}(N^3)$ amount of arithmetic operations.

First we provide the computational cost of the PCGA method. The PCGA employs a matrix-free iterative approach ((4.8) to (4.11)) for solving the cokriging system in (4.7). The total computational cost is [84]

$$\text{COMP}_{\text{PCGA}} \approx \mathcal{O}(\tau \tilde{N}\, n_{\text{PCGA}}), \tag{4.20}$$

where τ is the iteration number, n_{PCGA} is the rank of the approximated covariance matrix $Q_{n_{\text{PCGA}}}$ in (4.9).

We then further provide the computational cost of the RGA method. Because of the random projection, the size of the system matrix in (4.14) has been significantly reduced. Therefore, a direct linear solver such as QR factorization is tractable for solving the linear system in (4.14) [50]. Using a QR-factorization based linear solver to (4.14), the computational cost can be derived as

$$\text{COMP}_{\text{RGA\_Direct}} \approx \mathcal{O}((n+\tilde{p})^3) + \mathcal{O}((n+\tilde{p})^2), \tag{4.21}$$

where the first term corresponds to the cost of QR factorization, and the second term is the cost to form the right hand side and the cost to perform the back substitution. As an alternative, we can also employ the matrix-free iterative approach to solve (4.14) similar to the PCGA method. The resulting computational cost will be

$$\text{COMP}_{\text{RGA\_Iterative}} \approx \mathcal{O}(\tau\, kn), \tag{4.22}$$

where the variables yield the same meaning to the ones in (4.20).

Comparing the computational cost of the PCGA method in (4.20) to the cost of the RGA method in (4.21) and (4.22), one can observe that the RGA method should be more efficient in terms of solving the cokriging systems. However, it should be noted here that this analysis explores the computational cost of the linear algebra associated with performing an iteration of the inverse analysis. The overall computational cost should include another significant computational cost from solving the forward model repeatedly. However, when the PCGA is used and $\tilde{N}$ is sufficiently large, the computational cost associated with these linear algebra operations dominates the cost of running the forward model repeatedly. By reducing the cost of this linear algebra, the RGA results in a situation where the computational cost of repeatedly solving the forward model is the dominant cost in the inverse analysis. To summarize the overall computational costs of the RGA method and The PCGA method will be comparable when both inversion of the system and forward modeling are accounted, since both costs will likely be dominated by the cost of the forward modeling.

4.6.2 Memory cost

Both the RGA method and the reference method PCGA discussed in [73] and [84] rely on dense matrix storage. Hence, the major memory cost is used to store the matrices. Out of all these matrices, the matrices required to store are Z and HZ in (4.9) and (4.11) for the PCGA method or the matrix in (4.14) for the RGA method. Provided with the setup of the problem size, the dimension of system matrices of Z and HZ are $Z \in \mathcal{R}^{\tilde{m} \times n_{\text{PCGA}}}$ and $HZ \in \mathbb{R}^{\tilde{N} \times n_{\text{PCGA}}}$. Hence, the total memory cost of the PCGA method will be

$$\text{MEM}_{\text{PCGA}} \approx \mathcal{O}((\tilde{m} + \tilde{N}) \cdot n_{\text{PCGA}}). \tag{4.23}$$

Similarly, we can also calculate the dimension of the corresponding linear system in (4.14) for the RGA method. Provided with a rank n sketching matrix explicitly, the dimension

of the resulting linear system will be $\mathcal{R}^{(n+\tilde{p})\times(n+\tilde{p})}$. Hence, the total memory cost including both the sketching matrix and linear system is

$$\text{MEM}_{\text{RGA}} \approx \mathcal{O}\left((n+\tilde{p}) \times (n+\tilde{p}) + \tilde{N} \times k_{red}\right). \tag{4.24}$$

Comparing (4.24) to (4.23), we see that the memory cost of the RGA method is approximately $\kappa \approx n/n_{\text{PCGA}}$ of that of the PCGA method. Note the sketching matrix can be generated "on-the-fly". Instead of constructing the sketching matrix explicitly, we can generate the elements of the sketching matrix implicitly, therefore the storage of the random projection matrix can mostly be saved and resulted in cost of

$$\text{MEM}_{\text{RGA}} \approx \mathcal{O}\left((n+\tilde{p}) \times (n+\tilde{p})\right). \tag{4.25}$$

The efficient memory costs in (4.24) and (4.25) can be acheived with a straightforward the additional implementation of the RGA method on top of an existing PCGA implementation.

4.7 Numerical results

The reference problem is a transient groundwater equation.

We select Julia as our programming tool because of its efficiency and simplicity. Julia is a scalable scientific computing programming language designed for high-performance computing [13]. The Julia code for the RGA algorithm is available as a part of the open-source release of Julia version of MADS (Model Analysis and Decision Support) (see http://mads.lanl.gov/ [146]). The QR factorization and fundamental BLAS operations are all implemented using the system routines provided in the Julia packages. The first three sets of tests are run on a 40-core Intel Xeon E5-2650 running at 2.3 GHz, and 64 GB memory, and the final data scaling tests are run on a higher-memory machine with 64 AMD Opteron 6376 cores running at 2.3 GHz and 256 GB of memory.

Setting a stopping criterion is important for determining convergence of the iterative RGA method. The method thus uses two stopping criteria to determine convergence of the inverse solution for the GA cokriging system:

$$\|\mathbf{u}^{(k+1)} - \mathbf{u}^{(n_{\text{PCGA}})}\|_2^2 / \|\mathbf{u}^{(n_{\text{PCGA}})}\|_2^2 \leq \text{TOL}, \tag{4.26}$$

and

$$k \leq k_{MAX}, \tag{4.27}$$

where $\text{TOL} = 10^{-6}$ and $k_{MAX} = 50$.

4.7.1 Test for convergence

In our first numerical example, we first test the convergence of the RGA method. The reference model is solved on a grid containing 100×100, pressure nodes and a total of 20200 model parameters (100×101 log-transmissivities along x axis, 101×100 log-transmissivities along y axis). Table 4.1 describes the model set up in more detail. We generate a ground truth, which is shown in Figure 4.1(a). We utilize the variance ($\sigma_{\mathbf{u}}^2$) and an exponent ($\beta_{\mathbf{u}}$ – related to the fractal dimension of the field and the power-law of the field's spectrum) to characterize the heterogeneity of the considered fields [113]. In this example, we set the variance $\sigma_{\mathbf{u}}^2 = 0.5$ and power $\beta_{\mathbf{u}} = -3.5$. The total number of the measurements generated in this test is $16,000$, which come from running the transient simulation to simulate pumping tests at each well (a total of 4 tests) and acquiring data at all 4 locations (4 sets of data for each test). In each test, 1000 hydraulic head observations are recorded at each well.

Parameter	Value(s)	Notes
Observation noise	$N(\mu = 0, \sigma = 0.01)$	
Observations per well per pumping test	1000	
Number of observation/pumping wells	4-10	see Figures 4.1 and 4.5 for locations
Prior covariance for $\mathbf{T}$	$\sigma \approx 4.5$, $\lambda = 0.2$	exponential model
True heterogeneity of $\log_{10} \mathbf{T}$	$\mu = 0.5$, $\sigma = 1/2$	fractal model

Table 4.1: RGA calibration settings.

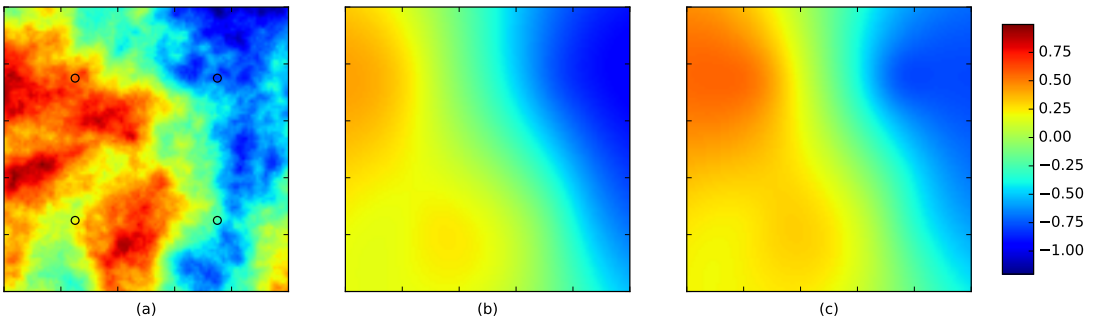

Figure 4.1: Synthetic log-transmissivity field (a) with variance $\sigma^2_{\mathbf{u}} = 0.5$ and power $\beta_{\mathbf{u}} = -3.5$. Hydraulic conductivity and hydraulic head observation locations are indicated with circles. The results of the inverse modeling solved by the PCGA (b) and the RGA algorithm (c) are shown. They are visually similar to each other. The RME values of the results in (b) and (c) are 0.28 and 0.33, respectively. The RGA method yields comparable results to results obtained using the PCGA method.

Figure 4.1(b) illustrates the result using the PCGA method. Our method yields the results in Figure 4.1(c). Comparing to the true model in Figure 4.1(a), the RGA method obtains a good result, representing both the high and low log-permeability regions. Visually, the RGA method yields a comparable result to the one obtained using the PCGA method in Figure 4.1(b).

To further quantify the inversion error of different inverse modeling methods, we calculate both the relative-model-error (RME) and relative-data-error (RDE) of the inversion results

$$\mathrm{RME}(\mathbf{u}) = \frac{\|\mathbf{u} - \mathbf{u}_{\mathrm{truth}}\|_2}{\sqrt{P} \times \mathrm{std}_{field}}, \tag{4.28}$$

where $\mathbf{u}$ is the inversion and $\mathbf{u}_{\mathrm{truth}}$ is the ground truth, P is the size of the model, and std_{field} is the standard deviation of the field.

$$\mathrm{RDE}(\mathbf{d}) = \frac{\|\mathbf{d} - \mathbf{d}_{\mathrm{rec}}\|_2}{\sqrt{N} \times \mathrm{std}_{noise}}, \tag{4.29}$$

where N is the size of the data, std_{noise} is the standard deviation of the additive noise, $\mathbf{d}$ is the simulated data based on the inversion and $\mathbf{d}_{\mathrm{rec}}$ are the recorded observations (which comes from solving the forward model for the reference transmissivity field and adding noise).

We provide the plot of the rates of convergence of the PCGA method and the RGA method in Figure 4.2. We observe that both the RGA method and the PCGA yield a very similar rate of the convergence as a function of the number of iterations steps. At each iteration, these methods yield similar relative data error and model error values. When both methods converged, the RME values of the RGA method and the PCGA method are 0.33 and 0.28, respectively. Therefore, together with the inversion result in Figure 4.1, we demonstrate that the RGA method yields a comparable accuracy to the PCGA method in this situation where both methods can be applied. We note, however, that one of the main benefits of the RGA method is that it can applied in situations with a very large number of observations and yield accurate results and efficient performance. Particularly in this example, it took the RGA only about $1,300$ seconds for the RGA to converge, where $1,210$ seconds on forward modeling and only 0.03 seconds on inversion.

The small reduced misfit dimension n can be critical to the accuracy and efficiency of the RGA method. In this section, we test the RGA method using randomization matrix with different rank values. The values of n used in the problem are 4, 8, 16, 32, 64, 128, 256, 512, 1024, 2048, 4096, and 8192.

In Figure 4.3, we further provide both the RME value defined in (4.28) in Figure 4.3(a) and RDE value defined in (4.29) in Figure 4.3(b). We notice that the larger n becomes, the smaller the error of the inversion. In the first few selections of n, there is significant decrease of the RME values, which means that the inversion results are improving. In particular, the inversion results are completely off when $n = 4$. At the selection of $n = 256$, the RME curve starts to level off while RDE curve still reduces.

Figure 4.4 shows the corresponding wall-clock time cost of different values of n. It can be observed that the time is quite stable around 500 seconds until $n = 2048$, where the CPU time increases to about 550 seconds. When $n = 8192$, the CPU time cost is 2902 seconds. This can be explained by the fact that when n is relatively small, the CPU time is mostly

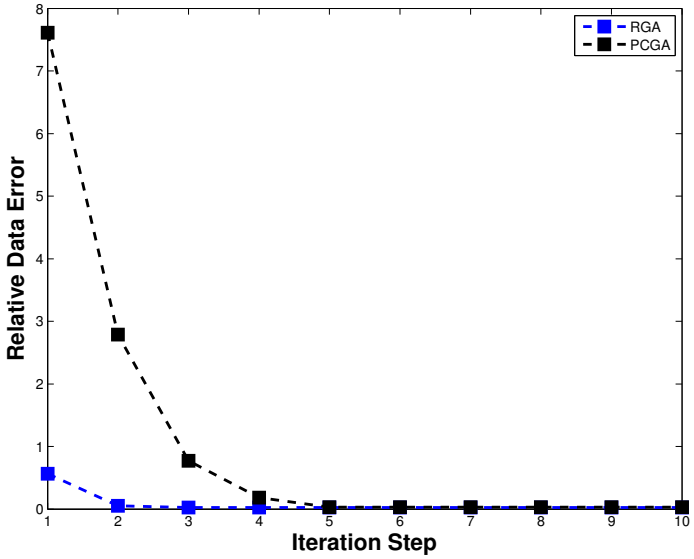

(a)

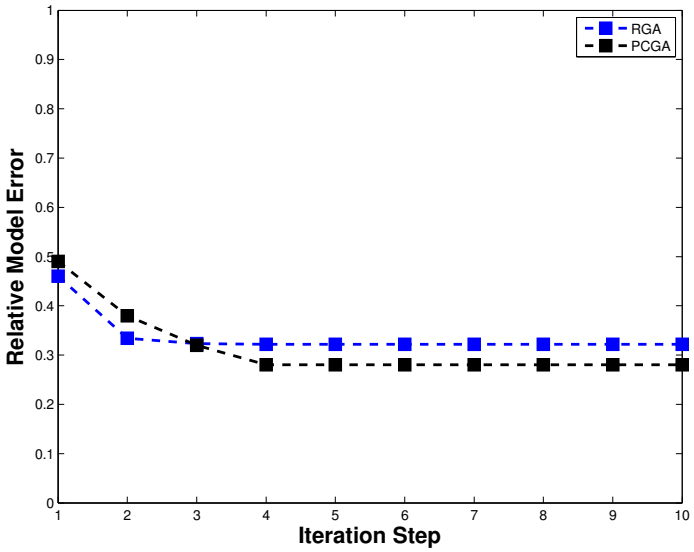

(b)

Figure 4.2: Convergence of the PCGA (in black) and the RGA (in blue) algorithms in terms of iteration steps. The rates of convergence for these two methods are very close to each other. However, the computational time of two methods to reach convergence are very different. In this case, the PCGA converged for about $32,000$ seconds, while the RGA convergence took only $1,020$ seconds. The the RGA speed-up is about 31 times.

dominated by the forward modeling operations, while as n increases, the linear solver for the solution of the system in (4.14) starts to dominate. Although the RDE decreases as n increases, observe that little information in the unknown parameter is gained.

From this test, it is suggested that the optimal n value for the target problem ranges 256 to 1024 by considering the relative model error, relative data error, and the wall-clock time. In general, when choosing the value of n, one would want to choose a value that is large enough to produce accurate results (i.e., large enough to be in the flat portion of Figure 4.3(a)) and small enough so that the method is computationally efficient (i.e., small enough to be in the flat portion of Figure 4.4).

4.7.2 Big data scaling test

To better understand the scalability of the RGA method for big geostatistical data, we test RGA on a set of log transmissivity estimation problems with an increasing number of noisy hydraulic head observations generated from a heterogeneous reference field. Specifically, we test the RGA method on inverse problems where the number of observations is equal to 2.56×10^5, 6.25×10^5, 1.296×10^6, 2.401×10^6, 4.096×10^6, 6.561×10^6, and 1.0×10^7. For each observation well, there are 1000 observations for each pumping test. The increasing number of observations come from increasing the number of pumping tests and the number of observation wells. For example, the case with 2.56×10^5 observations involves 16 pumping tests and 16 observations wells while the case with 1.0×10^7 involves 100 pumping tests and 100 observation wells. The reference transmissivity field is same as the one as in Figure 4.1(a). The value of n is again set to 256.

Through our analysis on memory cost in subsection 4.6.2, we observe that both the RGA method and the PCGA method can be comparable if we construct the random projection matrix explicitly. However, the RGA method can be more memory efficient than the PCGA method when we generate the random projection matrix "on-the-fly". Using the

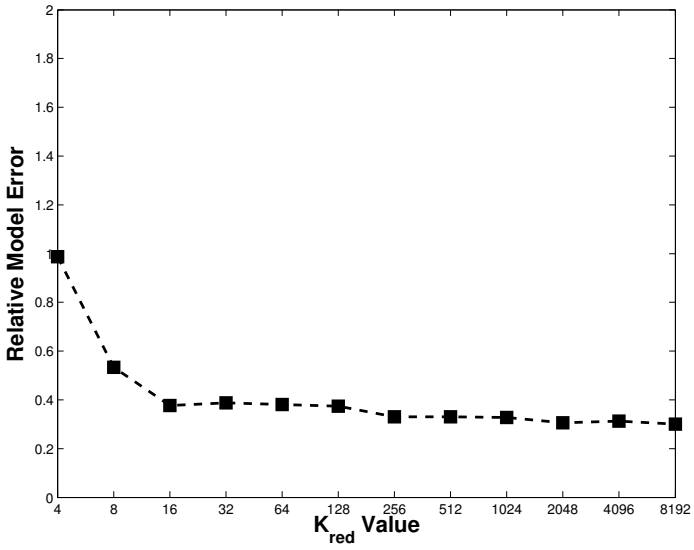

(a)

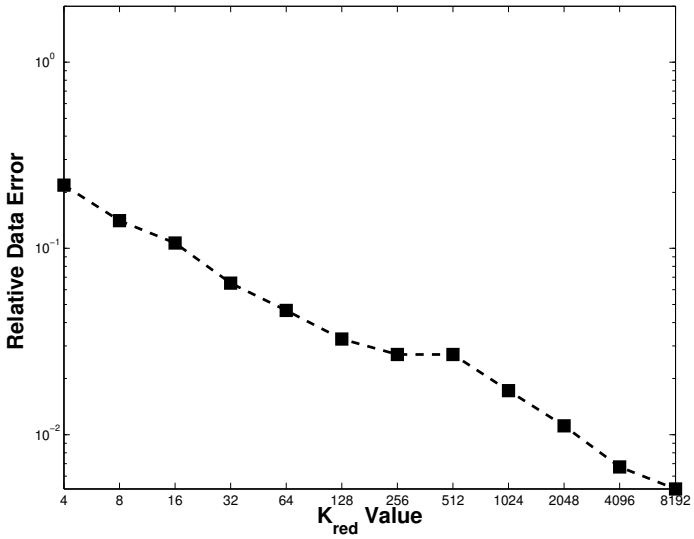

(b)

Figure 4.3: RME (a) and RDE (b) curves as defined in (4.28) and (4.29), respectively. For n increasing from 4 to 256, there is a significant decrease in RME. For $n \geq 256$, the RME curve starts to level off while RDE curve still reduces.

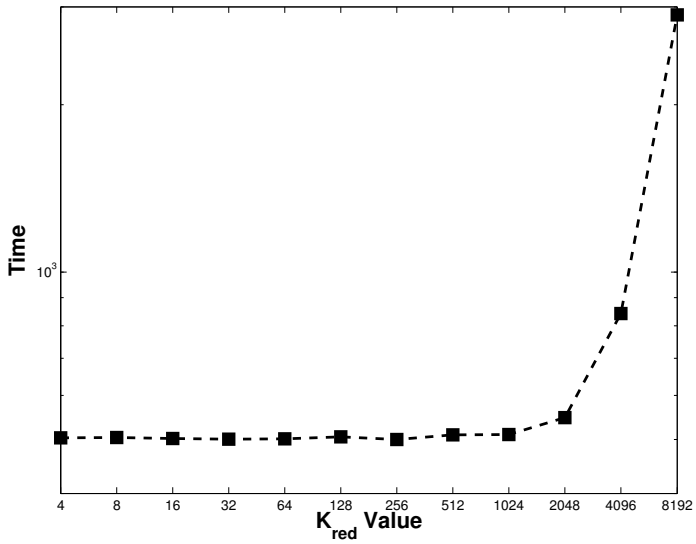

Figure 4.4: CPU time cost as a function of n. The CPU time is quite stable around 500 seconds for $n \leq 1024$. The time cost dependency on n can be explained by the fact that when n is relatively small, the CPU time is mostly dominated by the forward modeling operation, while as n increases, the linear solver for the solution of the system in (4.14) starts to dominate.

RGA, we are able to perform the inverse analysis with ten million observations. We tested the RGA method on all the problem sizes mentioned above and provide the corresponding results where the number of observations is 2.56×10^5, 4.096×10^6, and 1.0×10^7 in Figure 4.5. We notice that the RGA method yields reasonable inversion results when the size of the data sets becomes massive. The RME values of the inversion results in Figures 4.5(b), 4.5(c), and 4.5(d) are 0.26, 0.23 and 0.25, respectively. In each case, the PCGA method fails in all three cases of Figures 4.5(b), 4.5(c), and 4.5(d) due to insufficient memory.

We also provide the wall-clock time costs of the RGA method with different numbers of observations in Figure 4.6. Shown in Figure 4.6 is the wall-clock time to perform the model calibration with the RGA and the wall-clock time to perform a single model run. These times are shown for problems where the number of observations is 2.56×10^5, 6.25×10^5, 1.296×10^6, 2.401×10^6, 4.096×10^6, 6.561×10^6, and 1.0×10^7. For all these problems, which vary over two orders of magnitude, the time to perform the full model calibration takes 28 times as

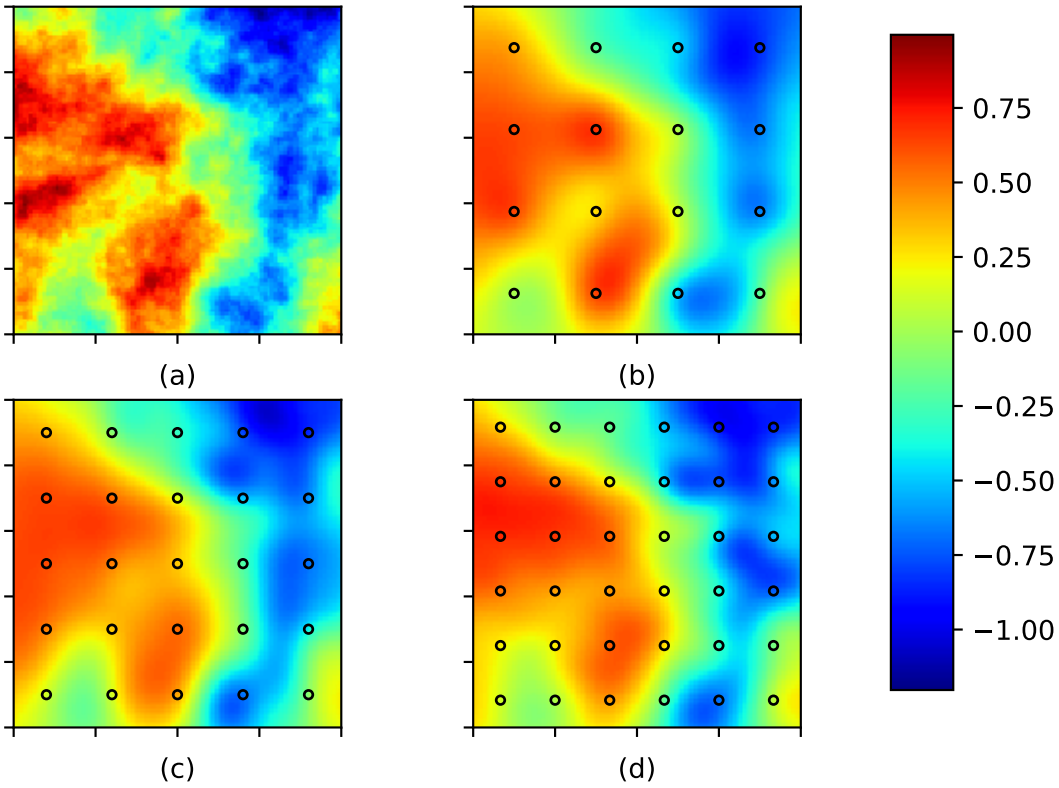

Figure 4.5: The "true" field (a) and inversion results of the RGA method with different numbers of observations including 2.56×10^5 (b), 4.096×10^6 (c) and 1.0×10^7 (d). Our the RGA method yields reasonable inversion results when the size of the data sets becomes massive. As a comparison, the PCGA method fails in all three cases of (b), (c), and (d) because of the insufficient memory.

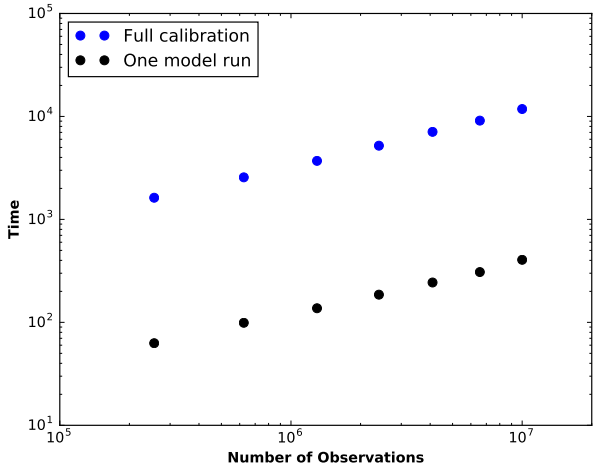

Figure 4.6: Wall-clock times to perform the model calibration with the RGA method and to perform a single model run. These times are shown for inverse analyses where the number of observations is 2.56×10^5, 6.25×10^5, 1.296×10^6, 2.401×10^6, 4.096×10^6, 6.561×10^6, and 1.0×10^7. For all these analyses, which vary over two orders of magnitude, the time to perform the full model calibration takes 28 times as long as performing a single model run and this could be reduced further with more CPU cores. The cost of each individual run increases due to increased foward simulation time when obtaining a larger number of pumping tests.

long as performing a single model run.

Chapter 5

Truncated domain inversion methods: For problems with spatially-concentrated data

This chapter is included in this dissertation because it proposes new data-driven reduction methods to overcome the computational challenge caused by high-dimensional parameter and state spaces in large-scale inverse and uncertainty quantification problems. The focus is on Bayesian inverse problems with spatially-concentrated observed data. These problems often have high parameter uncertainty in regions far from the subdomain of interest and the data. Using the domain decomposition-inspired methods developed in the chapter, the computational burden of solving the inverse problem can be mitigated by solving over the well-informed subdomain of interest only.

This chapter presents both model-constrained methods and non-model-constrained methods which require minimal offline computation. Numerical tests with a PDE-constrained inverse problem show online convergence is faster and requires fewer PDE solves than full domain inversion and an existing truncated domain inversion method. Furthermore, improved recovery fidelity of the truncated inversion parameter can be seen, compared to the full domain reconstruction.

5.1 Motivation: Data locality

Often, observational data and dynamics are spatially concentrated in large-scale inverse problems with high-dimensional parameter spaces. For example, observed data can be spatially confined to discrete well locations in reservoir parameter estimation. The dis-

tributed reservoir parameter, however, inherits the same dimensionality as the 2D or 3D model domain. Estimated parameter uncertainty is inevitably greater in regions far from the observational data locations and the domain of interest. To increase solution credibility, and simultaneously reduce the computational burden of solving the inverse problem, we wish to truncate a large inversion domain to a smaller, well-informed region.

This chapter details three new domain-decomposition based methods for improved efficiency and accuracy in inverting for a distributed parameter. In section 5.2, an efficient geometry for the truncated domain of interest is developed. In the methods introduced in sections 5.3 and 5.4, poorly-informed spatial regions are either discarded or approximated with a reduced order model (ROM). Then, an accurate boundary condition on the artificial boundary is estimated using an approximation of the unknown Dirichlet-to-Neumann (DtN) operator (also called the Steklov-Poincaré operator).

Numerical examples in section 5.5 illustrate the solution fidelity with the proposed methods. We also compare the computational cost, measured in number of PDE solves. Methods in section 5.4 use a goal-oriented, model-constrained approach to construct a robust DtN operator basis. Although the offline cost is greater than full-domain inversion with the model-constrained approaches, numerical results demonstrate improved recovery and faster convergence after the offline computation. Furthermore, the online savings is shown to more than offset the initial offline cost after computationally-intensive sampling for uncertainty quantification.

5.1.1 Domain truncation with Dirichlet-to-Neumann (DtN) operators

In subsurface transport modeling, a region of interest is often smaller than the full model domain. Artificial boundaries are used to make simulation computationally feasible by truncating the domain [11, 117, 149]. Along the artificial boundary, a constant concentration or a Neumann no-dispersive-flux condition is assumed. Modelers are advised to place the

artificial boundary sufficiently far away from the region of interest, as this naive boundary condition assumption leads to inaccuracies in the solution [11] (see also [79, 116, 117, 149]).

By calculating the DtN operator first, one can obtain boundary conditions that reduce inaccuracy near the artificial boundary. Artificial boundaries are frequently used in electric impedance tomography (EIT). In EIT, DtN operators have been used to to approximate the theoretically perfect boundary condition. This improves recovery and reduces spurious boundary effects, compared to a conventional homogeneous Neumann condition [27, 28, 29, 56, 67, 68, 70, 90, 97, 142]. *Theoretically perfect boundary condition* refers to theory from classical domain decomposition, which states that the forward solution over the truncated domain is the restriction of the full domain solution, if the exact DtN operator is used for the artificial boundary condition[27, 28, 67, 68].

The analytic form of the DtN operator is known for only some PDEs and canonical geometries (rectangles, ellipses, and annuli), but for any discretized PDE, a discrete, weakly-defined DtN operator on an arbitrary geometry can be constructed (see subsection 5.3.4 and [29]). However, this operator is dependent on the parameter in the discarded domain, *which is unknown in an inverse problem setting.* Hence the DtN operator must be approximated. Calvetti et al. [29] introduced a method for estimating the DtN operator simultaneously with the inversion parameter in a truncated EIT problem. An estimation approach is consistent with the philosophy of Bayesian inference, since the unknown DtN operator is estimated (compared to previous work where an approximated DtN operator is fixed using a constant discarded domain parameter [28]). The reconstructions over a truncated domain are shown to be similar to the restrictions of full-domain reconstructions, demonstrating the potential computational cost savings of inversion over a smaller domain.

The focus of this chapter is on the development of estimated DtN operator methods in order to decrease the computational burden of solving large-scale inverse and uncertainty quantification problems with high-dimensional parameter spaces. The heterogeneous dis-

tributed parameters that we wish to estimate in our problems of interest have a discretized dimension in the thousands or millions. Our domain-decomposition based approaches require specifying the geometry of the artificial boundary, near the region of interest. Since forward simulations are run multiple times over the domain in inverse problems and uncertainty quantification, we aim to make the truncated inversion domain as small as possible.

Secondly, although we also wish to speed up large-scale inversion, another goal in presenting the methodology here is to *improve reconstruction fidelity* beyond the full domain reconstruction. Important anomalies or physical features that cannot be recovered on a large domain can be recovered if the less-informed regions are discarded. This is demonstrated in the numerical examples in section 5.5. The intuition is that the truncated domain optimization and sampling runs are not led astray in an attempt to explore the less-informed region—truncating the domain can be thought of as a "warm-start".

We estimate the approximate DtN operator using methods based on domain decomposition for model reduction. The methods introduced here are inspired by the strategies used for the forward solution of PDEs in [10, 16, 39].

We detail a strategy in section 5.2 for truncating a large bounded inversion domain Ω for a PDE-constrained Bayesian inverse problem. To make our strategy concrete, we will the forward and inverse problem discussed in section 2.2, which is governed by an elliptic PDE.

In the following truncation strategy, we show that MAP point estimation can be the starting point for another method to reduce the computational cost of solving the Bayesian inverse problem.

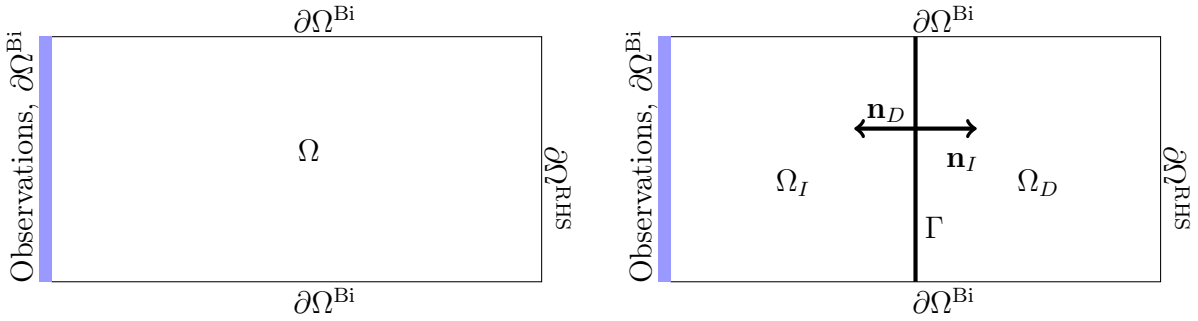

(a) (b)

Figure 5.1: (a) Full domain Ω and (b) truncated domain Ω_I (the domain of interest) and discarded domain Ω_D after introduction of the artificial boundary Γ.

5.2 Proposed truncation strategy

To mitigate the computational cost of solving the Bayesian inverse problem, we wish to partition Ω into two non-overlapping domains Ω_I and Ω_D, as shown in Figure 5.1(b). We call Ω_I the *domain of interest*, Ω_D the *discarded domain*, and $\Gamma := \Omega_I \cap \Omega_D$ the artificial boundary. Depending on the method used, we either discard the discarded domain Ω_D altogether or resolve it using a ROM, thus saving computational resources by no longer requiring full-order model (FOM) PDE solves over Ω_D.

We wish to make Ω_I as small as possible to gain the most in computational savings. Assuming that the nature of the problem does not *a priori* define an artificial boundary Γ and a domain of interest Ω_I, we have freedom to develop these geometries. We remark that the use of a finite element discretization and discrete DtN operator is invaluable here in permitting a non-canonical truncated domain geometry.

The following is our recommended truncation approach. First, estimate the MAP point $\mathbf{u}^{\text{MAP}}$ over the entire domain Ω by solving the deterministic inverse problem (2.8). Then, using the randomized SVD-based method in [25, 47], obtain an estimate of the distributed uncertainty, which is given by the Hessian of (2.8) $\mathcal{H}$ about $\mathbf{u}^{\text{MAP}}$. Find a threshold

level ℓ for $\mathcal{H}$ such that the noisy observations $\mathbf{d}$ are contained in Ω_I. That is, first find a small ℓ such that

$$\max_{x \in \mathbf{d}} \mathcal{H}(x) < \ell,$$

then

$$\Omega_I = \{x \in \Omega : \mathcal{H}(x) < \ell\}.$$

Then the final step is to patch any holes in Ω_I so that the final domain of interest is a simply connected domain.

This uncertainty-guided truncation strategy is useful for large-scale Bayesian inverse problems where accurate statistical estimation of large high or low regions is critical, such as inverse problems in reservoir exploration or medical imaging. Truncating to the well-informed region Ω_I prevents the optimization from exploring the poorly-informed parameter space on Ω_D, and thus computational resources can be diverted to get a better resolution estimate over Ω_I instead of attempting to resolve over the full domain Ω. The strategy can be adjusted depending on the estimation goals of the inverse problem. In the each of the truncated inversion methods detailed in the present work, FOM PDE solves are run only over the domain of interest Ω_I.

5.3 Inversion methods with minimal offline cost

5.3.1 Method: Full domain inversion

We refer to the conventional method of inverting for the spatially distributed parameter $\mathbf{u}$ over the entire model domain Ω as full domain inversion.

5.3.2 The truncated Bayesian inverse problem

After decomposing the domain Ω into Ω_I and Ω_D, either following the strategy discussed in section 5.2 or in another problem-dependent manner, there is an artificial boundary Γ on which boundary values must be prescribed.

Following a classical Dirichlet-Neumann method for domain decomposition, flux boundary conditions are prescribed on Γ for the forward problem domain of interest. The flux boundary values on the artificial boundary Γ are given by a boundary functional $\Lambda_{\mathbf{u}_D}$. The boundary value problem (BVP) on the domain of interest Ω_I is: find a solution $\mathbf{w}_I \in H^1(\Omega_I)$ satisfying

$$\begin{aligned} -\nabla \cdot (e^{\mathbf{u}_I} \nabla \mathbf{w}_I) &= f(\mathbf{u}_I) && \text{in } \Omega_I, \\ -e^{\mathbf{u}_I} \nabla \mathbf{w}_I \cdot \mathbf{n}_I &= textBi\, \mathbf{w}_I && texton\ \partial\Omega_I^{\mathrm{Bi}} \\ -e^{\mathbf{u}_I} \nabla \mathbf{w}_I \cdot \mathbf{n}_I &= \Lambda_{\mathbf{u}_D}(\mathbf{w}_I) && texton\ \Gamma, \end{aligned} \tag{5.1}$$

where $\mathbf{n}_j$ denotes the outward normal for the region $\Omega_j,\ j = I, D$.

The *truncated inverse problem* over the domain of interest Ω_I is: estimate $\mathbf{u}_I$ over Ω_I *and* the unknown boundary functional $\Lambda_{\mathbf{u}_D}$, given the data $\mathbf{d}$ from the full domain inverse problem (2.7). The truncated inverse problem MAP point is the solution to

$$\mathbf{u}_I^{textMAP} := \arg\min_{\mathbf{u}} J(\mathbf{u}, \Lambda_{\mathbf{u}_D}) = \frac{1}{2} \|\mathbf{F}_I(\mathbf{u}) - \mathbf{d}\|^2_{\mathbf{\Gamma}^{-1}_{textnoise}} + \frac{1}{2}\alpha \|\mathbf{R_I u}\|^2 + \frac{1}{2}\alpha_\Lambda \|\mathbf{R_\Lambda} \Lambda_{\mathbf{u}_D}\|^2, \tag{5.2}$$

where $\mathbf{F}_I(\mathbf{u})$ is the parameter-to-observable map on the truncated domain, $\frac{1}{2}\,\alpha_\Lambda \|\mathbf{R_\Lambda} \Lambda_{\mathbf{u}_D}\|^2$ is the prior for the unknown boundary functional $\Lambda_{\mathbf{u}_D}$, and $\mathbf{R_I}$ is the conditional prior computed from the prior regularization $\mathbf{R} = \mathbf{\Gamma}^{-\frac{1}{2}}_{\text{prior}}$ in the full-domain problem (2.8).

5.3.3 The discarded domain BVP and the associated DtN operator

Suppose Dirichlet values ϕ are prescribed on Γ in the following BVP over the discarded domain Ω_D:

$$\begin{aligned} -\nabla \cdot (e^{\mathbf{u}_D} \nabla \mathbf{w}_D) &= f(\mathbf{u}_D) && \text{in } \Omega_D, \\ -e^{\mathbf{u}_D} \nabla \mathbf{w}_D \cdot \mathbf{n}_D &= \mathrm{Bi}\, \mathbf{w}_D && \text{on } \partial\Omega_D^{\mathrm{Bi}} \\ -e^{\mathbf{u}_D} \nabla \mathbf{w}_D \cdot \mathbf{n}_D &= -1 && \text{on } \partial\Omega^{\mathrm{RHS}} \\ \mathbf{w}_D &= \phi \\ texton\Gamma. \end{aligned} \tag{5.3}$$

If $\mathbf{w}_D$ is the solution to the discarded domain BVP (5.3), then the DtN operator $\Lambda_{\mathbf{u}_D} : H^{\frac{1}{2}}(\Gamma) \to \left(H^{\frac{1}{2}}(\Gamma)\right)^*$ associated with (5.3) is defined as

$$\Lambda_{\mathbf{u}_D}(\phi) = e^{\mathbf{u}_D} \nabla \mathbf{w}_D \cdot \mathbf{n}_D \quad \text{on } \Gamma. \tag{5.4}$$

Note that the DtN operator $\Lambda_{\mathbf{u}_D}$ depends on the parameter $\mathbf{u}_D$ in the discarded domain Ω_D, which is unknown in the original inverse problem (2.8).

If (5.3) is already discretized in the finite element method, then a discrete approximation of the associated DtN operator $\Lambda_{\mathbf{u}_D}$ follows from the weak form of (5.3) and (5.4). This construction is detailed in subsection 5.3.4.

5.3.4 The discretized Dirichlet-to-Neumann (DtN) operator

This section contains the finite element discretization of the exact DtN operator (5.4) associated with the discarded domain BVP (5.3). Each of the truncated inversion methods discussed in the present work uses this discrete DtN operator.

Using a finite element formulation, the domains Ω_I and Ω_D are subdivided into triangles when $n = 2$ and tetrahedra when $n = 3$. We choose the meshes for Ω_I and Ω_D so that the N_Γ artificial boundary nodes on Γ align. That is, the last N_Γ nodes of the domain of interest Ω_I and the first N_Γ nodes of the discarded domain Ω_D are the same.

First we derive a weak definition of the DtN operator (5.4) from the weak form of the discarded domain BVP (5.3). Multiplying (5.3) by a test function $v \in H^1(\Omega_D)$ and using Green's theorem

$$\int_{\Omega_D} e^{\mathbf{u}_D} \nabla \mathbf{w}_D \cdot \nabla v + \int_{\partial\Omega^{\mathrm{Bi}}} \mathrm{Bi}\, \mathbf{w}_D v - \int_{\Gamma} v e^{\mathbf{u}_D} \nabla \mathbf{w}_D \cdot \mathbf{n}_D = \int_{\partial\Omega_D^{\mathrm{RHS}}} v. \tag{5.5}$$

Then substituting in the weak form of (5.4) and rearranging,

$$\langle v, \Lambda_{\mathbf{u}_D} \mathbf{w}_D \rangle_{\Gamma} = \langle \nabla v, e^{\mathbf{u}_D} \nabla \mathbf{w}_D \rangle_{\Omega_D} + \langle v, \mathrm{Bi}\, \mathbf{w}_D \rangle_{\partial\Omega^{\mathrm{Bi}}} - \langle 1, v \rangle_{\partial\Omega_D^{\mathrm{RHS}}}. \tag{5.6}$$

Equation (5.6) is then discretized by setting

$$K_{ij} = \langle \nabla \varphi_i, e^{\mathbf{u}_D} \nabla \varphi_j \rangle_{\Omega_D} + \langle \varphi_i, \mathrm{Bi}\, \varphi_j \rangle_{\partial\Omega^{\mathrm{Bi}}} \tag{5.7}$$

and

$$F_i = \langle 1, \varphi_i \rangle_{\partial\Omega_D^{\mathrm{RHS}}},$$

where $\varphi_i, n = 1, \ldots N_D$ are the basis functions corresponding to the N_D nodes on the discarded domain mesh.

We block partition the resulting stiffness matrix $\mathbf{K} \in \mathbb{R}^{N_D \times N_D}$ as

$$\mathbf{K} = \begin{bmatrix} \mathbf{K^{11}} & \mathbf{K^{12}} \\ \mathbf{K^{21}} & \mathbf{K^{22}} \end{bmatrix}, \quad \text{where } \mathbf{K^{11}} \in \mathbb{R}^{N_\Gamma \times N_\Gamma},$$

and the load vector $\mathbf{F} \in \mathbb{R}^{N_D}$ as

$$\mathbf{F} = \begin{bmatrix} \mathbf{F^1} \\ \mathbf{F^2} \end{bmatrix}, \quad \text{where } \mathbf{F^1} \in \mathbb{R}^{N_\Gamma}.$$

Given the Dirichlet boundary function $\mathbf{w}_D|_\Gamma = \phi$, let $\phi_n = \phi(x_n)$ for boundary nodes $x_n \in \Gamma$. Then the solution to the discarded domain BVP (5.3) $\mathbf{w}_D$ is expanded as

$$\mathbf{w}_D(x) \approx \sum_{n=1}^{N_\Gamma} \phi_n \varphi_n(x) + \sum_{n=N_\Gamma+1}^{N_D} \omega_n \varphi_n(x).$$

Letting $v = \varphi_i$ for $i = N_\Gamma + 1, \ldots, N_D$ in the discretized DtN weak definition (5.6),

$$\mathbf{K^{21}}\phi + \mathbf{K^{22}}\omega = \mathbf{F^2}, \quad \text{where } \phi = \begin{bmatrix} \phi_1 \\ \vdots \\ \phi_{N_\Gamma} \end{bmatrix} \text{ and } \omega = \begin{bmatrix} \omega_{N_\Gamma+1} \\ \vdots \\ \omega_{N_2} \end{bmatrix}.$$

Solving the above linear system for ω, which represents the nodes in the discarded domain Ω_D *not* on the artificial boundary Γ (this is possible due to the coercivity of the bilinear BVP operator (5.7)),

$$\omega = \left(\mathbf{K^{22}}\right)^{-1}\left(\mathbf{F_2} - \mathbf{K^{21}}\phi\right). \tag{5.8}$$

Then choosing $v = \varphi_i$, $i = 1, \ldots, N_\Gamma$ in the discretized DtN weak definition (5.6),

$$\langle \varphi_i, \Lambda_{\mathbf{u}_D}\phi\rangle = \underbrace{\mathbf{K^{12}}\left(\mathbf{K^{22}}\right)^{-1}\mathbf{F_2}}_{\mathbf{R}_i :=} + \underbrace{\left[\left(\mathbf{K^{11}} - \mathbf{K^{12}}\left(\mathbf{K^{22}}\right)^{-1}\mathbf{K^{21}}\right)\phi\right]_i}_{(\mathbf{L}\phi)_i :=}. \tag{5.9}$$

Thus the discretized DtN operator $\Lambda_{\mathbf{u}_D}$ is represented as an affine map on the Dirichlet boundary function ϕ,

$$\Lambda_{\mathbf{u}_D} : \phi \to \mathbf{L}\phi + \mathbf{R}. \tag{5.10}$$

5.3.5 Method: Truth DtN

We can observe from the weak DtN definition (5.6), that given a log conductivity distribution $\mathbf{u}_D$ in the discarded domain Ω_D, one can (weakly) define the operator

$$\Lambda : \mathbf{u}_D \to \Lambda_{\mathbf{u}_D}. \tag{5.11}$$

Note this is not the DtN operator (5.4) whose input is functions on Γ, but the map defined on Ω_D that takes a *parameter distribution in* Ω_D to the DtN operator $\Lambda_{\mathbf{u}_D}$ associated with the discarded domain BVP (5.3).

After defining the DtN operator with the truth $\mathbf{u}_D$, its (weak) action on the artificial boundary Dirichlet values, denoted by $\langle v, \Lambda_{\mathbf{u}_D}\mathbf{w}_I\rangle_\Gamma$, can be used to complete the weak form of the domain of interest BVP (5.1). Then, using the theory mentioned in the review of

related work in subsection 5.1.1, the forward BVP in the domain of interest (5.1) is well-posed and its solution is exactly the restriction of the forward solution to the full domain BVP (2.4).

Thus the first truncated domain inversion method we investigate is one that uses the truth DtN operator as a nonlocal boundary condition in the truncated BVP (5.1). That is,

$$\Lambda_{\mathbf{u}_D} = \Lambda(\mathbf{u}_D), \tag{5.12}$$

where Λ is the operator (5.11) that takes a parameter in the discarded domain Ω_D (here the underlying truth $\mathbf{u}_D$ which is unknown in the full domain inverse problem) to the corresponding DtN map on the artificial boundary Γ. This method is discussed only for the purpose of validating other methods, which use estimates of this truth DtN operator.

Recall that the primary goal in the truncated inverse problem (5.2) is to estimate the unknown truncated parameter $\mathbf{u}_I$ over the domain of interest Ω_I. Suppose we knew the truth parameter over the discarded domain, $\mathbf{u}_D \in \Omega_D$. Following the discretization of the DtN operator in subsection 5.3.4, we can construct the truth DtN operator $\Lambda_{\mathbf{u}_D}$ and therefore the perfect boundary condition for Γ. Then, to apply the nonlocal boundary condition and solve the truncated inverse problem governed by the BVP (5.1) in Ω_I, the discretized affine DtN map (5.10) is used to augment both the left and right hand sides of the finite element system over the domain of interest.

Although there may exist an application where this hypothetical situation, it is unlikely that $\mathbf{u}_D$ would be known exactly and $\mathbf{u}_I$ would need to be estimated. Again this method is presented here only to construct a possibly fairer, alternative metric for validation of our truncated domain inversion results, other than comparison to the distant synthetic truth parameter.

5.3.6 Method: Sampling DtN

In the likely case that $\mathbf{u}_D$ is unknown, inverting for $\mathbf{u}_D$ would defeat the purpose of truncating the domain to aid inverting for $\mathbf{u}_I$. Therefore the DtN map $\Lambda_{\mathbf{u}_D}$ (5.12) *must* be estimated with an efficient approximation, denoted by $\tilde{\Lambda}_{\mathbf{u}_D}$.

As mentioned in the review in subsection 5.1.1, existing work with the EIT problem uses a constant log conductivity in the discarded domain to generate an approximation of the perfect boundary condition (5.12). That is, a constant $\overline{\mathbf{u}_D}$ is input into the operator Λ (5.11) as a guess for the heterogeneous truth $\mathbf{u}_D$, and the result is an approximate DtN map $\tilde{\Lambda}_{\mathbf{u}_D} = \Lambda(\overline{\mathbf{u}_D})$. When used for the artificial boundary condition in (5.1), visible improvement in inversion results can be seen, compared to inversion results that use a conventionally enforced homogeneous Neumann condition [28, 67, 68].

In [29] this method is extended further to compute an approximate DtN map that is consistent with a statistical Bayesian framework. Prior samples $\{\widehat{\mathbf{u}}_i\}_{i=1}^N$ of the unknown discarded domain conductivity $\mathbf{u}_D$ are input into the operator Λ (5.11) to construct a snapshot matrix of (vectorized) discrete affine DtN maps (5.10)

$$\mathbf{S} = \left[\text{vec}(\Lambda(\widehat{\mathbf{u}}_1)) \quad | \quad \cdots \quad | \quad \text{vec}(\Lambda(\widehat{\mathbf{u}}_N))\right]. \tag{5.13}$$

The snapshot matrix $\mathbf{S}$ is then used to compute a low-rank basis for $\tilde{\Lambda}_{\mathbf{u}_D}$, using a proper orthogonal decomposition (POD). Then,

$$\tilde{\Lambda}_{\mathbf{u}_D} = \sum_{i=1}^{r} c_i \Phi_i, \tag{5.14}$$

for $r < N$, where the basis functions Φ_i are computed from the sampling-based snapshot matrix of DtN operators $\mathbf{S}$ (5.13). The low-rank basis coefficients c_i are then estimated as part of the inverse problem on Ω_I.

This estimation is important because it permits uncertainty quantification of the DtN map, which is an unknown in the truncated inverse problem. It is found that the

reconstructions with the low-rank $\tilde{\Lambda}_{\mathbf{u}_D}$ also improved upon the conventional homogeneous Neumann condition, and that results do not visually improve by using a basis with rank r larger than 5. We refer to this truncated inversion method of constructing a low-rank DtN basis from discarded domain prior samples as the sampling DtN method.

5.3.7 Method: Projection DtN

The following sections present three different methods for truncated domain inversion as alternatives to the sampling DtN method in subsection 5.3.6.

The first method is an iterative method based on classical Dirichlet-Neumann iterations for domain decomposition. The algorithm may be thought of as the inverse analog of the approach presented in [16, subsection 2.1] for the forward solution of PDEs. It consists of alternating stages of a FOM inversion for $\mathbf{u}_I$ over the domain of interest, and a ROM approximation of the discarded domain parameter $\mathbf{u}_D$. This method may be useful for when a low-fidelity estimate of the discarded domain is desired, since an approximation of $\mathbf{u}_D$ is automatically computed. The projection DtN method steps are the following:

(Offline) Collect prior samples $\{\widehat{\mathbf{u}}_i\}_{i=1}^N$ over the discarded domain Ω_D, similar to the sampling DtN method in subsection 5.3.6. Compute a basis for the *parameter* over Ω_D using POD. Using a random sample over Ω_D^0, compute the initial DtN operator $\Lambda_{\mathbf{u}_D^0} = \Lambda(\mathbf{u}_D^0)$.

(1) Complete the finite element system for the domain of interest BVP (5.1) using the current DtN operator $\Lambda_{\mathbf{u}_D^{k-1}}$.

(2) Invert for $\mathbf{u}_I^k$ over Ω_I using coarse tolerances or by setting low maximum iterations.

(3) Project $\mathbf{u}_I^k$ onto *the trace* of the POD parameter basis for Ω_D (the collection of the basis functions restricted to the artificial boundary Γ).

(4) Prolongate the projection to obtain an estimate $\mathbf{u}_D^k$ over Ω_D.

(5) Compute the new estimated DtN operator $\Lambda_{\mathbf{u}_D^k} = \Lambda(\mathbf{u}_D^k)$.

(6) Repeat (1)-(5) until convergence.

5.4 Model-constrained optimization methods for offline DtN basis construction

Similar to the sampling DtN method in subsection 5.3.6, the two remaining truncated inversion methods use a low-rank approximation of the DtN map. The methods are an alternating DtN method and an all-at-once DtN method. The major difference between these two methods is in their implementation and numerical performance, whereas their theoretical foundation is similar.

Unlike the sampling DtN method or the projection DtN method in subsection 5.3.7, these methods require offline optimization over the discarded domain to obtain a *model-constrained* low-rank basis [17] for the DtN map. Although this initially requires more computation than the non-model-constrained methods, there is potentially greater payoff in improved accuracy and reduced online computation for inversion and uncertainty quantification.

The model-constrained basis for a low-rank DtN map $\tilde{\Lambda}_{\mathbf{u}_D}$ (5.14) is motivated as follows. First consider the low-rank basis for $\tilde{\Lambda}_{\mathbf{u}_D}$ that is determined offline in the sampling DtN method. The coefficients for the basis are estimated online as part of solving the truncated inverse problem (5.1). This is in line with a Bayesian statistical inversion framework, since the truth $\mathbf{u}_D$ generally is unknown. The truth DtN $\Lambda_{\mathbf{u}_D}$ (5.12), which depends on $\mathbf{u}_D$, therefore is estimated along with $\mathbf{u}_I$ as an unknown in the inverse problem over Ω_I.

The online solution procedure over Ω_I estimates the coefficients for a low-rank approximation $\tilde{\Lambda}_{\mathbf{u}_D}$ (5.14), which in effect estimates the flux values normal to the artificial boundary Γ. For the solution method to perform well, the basis constructed offline for $\tilde{\Lambda}_{\mathbf{u}_D}(\phi)$ should be robust and goal-oriented. For the problem of interest, a robust, goal-oriented basis is one with an output space that spans the largest space of flux values possible.

Sampling from the prior for $\mathbf{u}_D$ to obtain a snapshot matrix $\mathbf{S}$ (5.13) for the low-rank basis does not necessarily produce a basis that spans the largest space of possible flux

values. Even with distinct or orthogonal samples $\widehat{\mathbf{u}}_i$, the collection of DtN maps $\Lambda(\widehat{\mathbf{u}}_i)$ in the snapshot matrix $\mathbf{S}$ could still have flux values $\Lambda_{\widehat{\mathbf{u}}_i}(\phi)$ that were collinear, due to the non-linearity of the DtN map construction (5.9).

5.4.1 Offline model-constrained optimization

In light of this ideal goal for a low-rank basis, that is, for its range to span the space of feasible flux values normal to the artificial boundary Γ, we propose a greedy approach to improve the snapshot matrix $\mathbf{S}$ (5.13). The snapshot matrix is subsequently orthogonalized using POD to obtain a rank-r (where $r < N$) low-rank basis

$$\{\Phi_i\}_{i=1}^{r} \tag{5.15}$$

for $\tilde{\Lambda}_{\mathbf{u}_D}$, which is referred to here as the DtN basis.

The greedy approach is most closely related to the model-constrained optimization in [17]. At each offline stage, a new sample $\widehat{\mathbf{u}}$ is found by maximizing the error with the current basis in the quantity we wish to approximate. The quantity to be approximated consists of the fluxes normal to Γ, given by the action of $\Lambda_{\mathbf{u}} = \Lambda(\mathbf{u})$ on the artificial boundary temperatures ϕ. Then, a new snapshot $\Lambda(\widehat{\mathbf{u}})$ is computed and appended to the existing snapshot matrix.

After each offline stage, a worst-case error approximation of the target quantity, the truth flux on Γ, is minimized. Specifically, the goal of each stage is to satisfy the constrained optimization problem

$$\begin{aligned} \widehat{\mathbf{u}} = \arg \max_{\mathbf{u}\in\Omega_D} J_D = & \frac{1}{2N_\Gamma} \sum_{j=1}^{N_\Gamma} \left\| \Lambda_{\mathbf{u}}\phi_j - \tilde{\Lambda}_{\mathbf{u}_D}(\mathbf{u})\phi_j \right\|^2 - \frac{\beta}{2}\|\mathbf{R_D u}\|^2 \\ & \text{s.t. (5.9)}. \end{aligned} \tag{5.16}$$

Here $\{\phi_j\}_{j=1}^{N_\Gamma}$ are basis functions in $H^{\frac{1}{2}}(\Gamma)$ (chosen to be the finite element basis functions on Γ). The regularization term with regularization parameter $\beta > 0$ is added to ensure that

physically realistic parameters are chosen, and $\mathbf{R_D}$ is the conditional prior computed from the full-domain prior (2.7). The DtN operator $\Lambda_{\mathbf{u}}$ here is the output of the operator Λ (5.4) with input $\mathbf{u}$, corresponding to the discarded domain BVP (5.3) with a known distribution $\mathbf{u}_D = \mathbf{u}$ over Ω_D. Note that the constraint is the affine map definition of $\Lambda_{\mathbf{u}}$ (5.9), which implicitly enforces the discarded domain BVP (5.3).

The DtN operator $\Lambda_{\mathbf{u}}$ is successively approximated by the current $\tilde{\Lambda}_{\mathbf{u}_D} = \tilde{\Lambda}^k_{\mathbf{u}_D}$. This is the low-rank DtN map at the current stage k in the model-constrained optimization (5.16)

$$\tilde{\Lambda}^k_{\mathbf{u}_D} = \sum_{i=1}^{B} c_i^k \Phi_i^k, \tag{5.17}$$

where $\left\{\Phi_i^k\right\}_{i=1}^B$ refers to the rank-B basis at the current stage k, for $B \leq r$. The basis coefficients c_i^k are ultimately optimized as part of solving the inverse problem over the truncated domain of interest Ω_I. However, the model-constrained optimization (5.16) is repeatedly solved as part of the offline construction for the final rank-r basis (5.15), *before* this basis is used in the truncated inverse problem.

Thus for the purpose of solving the model-constrained optimization (5.16), we define parameter-dependent coefficients $\{c_i(\mathbf{u})\}_{i=1}^B$ that results in an optimal low-rank approximation for $\Lambda_{\mathbf{u}}$ by

$$c_i(\mathbf{u}) = \frac{\langle \mathrm{vec}(\mathbf{\Lambda}(\mathbf{u})), \mathrm{vec}(\mathbf{\Phi}_i)\rangle}{\langle \mathrm{vec}(\mathbf{\Phi}_i), \mathrm{vec}(\mathbf{\Phi}_i)\rangle}$$

where $\mathbf{\Lambda}(\mathbf{u}) := \left[\begin{array}{c|c} \mathbf{L}(\mathbf{u}) & \mathbf{R}(\mathbf{u}) \end{array}\right]$ corresponds to the discretized affine operator (5.10). Then the c_i and subsequently the current low-rank $\tilde{\Lambda}_{\mathbf{u}_D}$ (5.17) are dependent on the input parameter $\mathbf{u}$ in the model-constrained optimization problem (5.16). The matrix $\mathbf{\Phi}_i := \left[\begin{array}{c|c} \mathbf{L}_i & \mathbf{R}_i \end{array}\right]$ is the augmented matrix representation of the DtN basis function Φ_i, which after discretization is an affine map

$$\Phi_i : \phi \to \mathbf{L}_i\phi + \mathbf{R}_i. \tag{5.18}$$

After the k-th stage, $\widehat{\mathbf{u}}_{N+1}$ is the greedy solution to the model-constrained optimization (5.16) for some $N \geq k$. The snapshot matrix is augmented to

$$\mathbf{S} = \left[\text{vec}(\boldsymbol{\Lambda}(\widehat{\mathbf{u}}_1)) \;\; | \;\; \cdots \;\; | \;\; \text{vec}(\boldsymbol{\Lambda}(\widehat{\mathbf{u}}_N)) \;\; | \;\; \text{vec}(\boldsymbol{\Lambda}(\widehat{\mathbf{u}}_{N+1}))\right].$$

The new rank-B DtN basis functions used in the $(k+1)$-th stage, $\left\{\Phi_i^{k+1}\right\}_{i=1}^{B}$, are computed by a POD of $\mathbf{S}$. Then B is (possibly) increased by one, and the process is repeated to obtain a given number of snapshots or until convergence. Convergence here could mean that the worst-case error in (5.16) decreases below a given tolerance.

5.4.2 Method: Alternating DtN

The alternating DtN method first computes the low-rank DtN basis $\{\Phi_i\}_{i=1}^{r}$ (5.15) following subsection 5.4.1. Then the truncated domain parameter $\mathbf{u}_I$ and the low-rank DtN operator coefficients c_i are estimated in an alternating manner.

Two different cost functions are solved coarsely in successive stages. In the parameter inversion stages, the DtN map is fixed. In the coefficient inversion stages, the parameter is fixed. The steps for the alternating DtN method are:

(Offline) Build a model-constrained basis for the DtN operator following subsection 5.4.1. Initialize the DtN coefficients with starting values c_i^0.

(1) Parameter inversion stage: Compute the low-rank DtN map $\tilde{\Lambda}_{\mathbf{u}_D}$ (5.17) with the current coefficients c_i^k. Complete the finite element system for the truncated BVP (5.1) using $\tilde{\Lambda}_{\mathbf{u}_D}$. Invert for $\mathbf{u}_I^k$ over Ω_I. Terminate early with low maximum iterations, if not yet converged.

(2) Coefficient inversion stage: Fix the parameter $\mathbf{u}_I^k$, and invert for the low-rank DtN coefficients c_i^{k+1}. Terminate early with low maximum iterations, if not yet converged.

(3) Repeat until convergence.

5.4.3 Method: All-at-once DtN

The all-at-once DtN method first computes the low-rank DtN basis $\{\Phi_i\}_{i=1}^r$ (5.15) following subsection 5.4.1. Then the coefficients c_i for the low-rank DtN operator $\tilde{\Lambda}_{\mathbf{u}_D}$ (5.17) are estimated *simultaneously* with the truncated parameter $\mathbf{u}_I$ as part of the inverse problem, similar to the sampling DtN method in subsection 5.3.6.

The simultaneous estimation allows the optimization on Ω_I to tune the DtN map $\tilde{\Lambda}_{\mathbf{u}_D}$ to one consistent with the data and the PDE, analogous to the method for forward solves in [16, section 3]. The steps for the all-at-once DtN method are as follows:

(Offline) Build a model-constrained basis for the DtN operator following subsection 5.4.1. Initialize the coefficients c_i with starting values. Complete the finite element system for the truncated problem with the current initial low-rank DtN map.

(1) Invert for the DtN coefficients and parameter simultaneously by augmenting the parameter vector. Solve until convergence.

5.5 Numerical results

5.5.1 Comparison of MAP estimation

Figure 5.5 shows MAP estimation results (deterministic inversion) for an elliptic test problem solved using the new methods presented in sections 5.3 and 5.4. Shown are the MAP points using the projection DtN, alternating DtN, and all-at-once DtN methods from subsections 5.3.7, 5.4.2 and 5.4.3, respectively. Each MAP estimate shown is the converged minimum of a cost functional with a level of parameter prior chosen to be $\alpha = 5$. For truncated methods that invert for the coefficients c_i of $\tilde{\Lambda}_{\mathbf{u}_D}$ in (5.14) as part of the inverse problem (the sampling, alternating, and all-at-once DtN methods, which use (5.2)), we use a coefficient prior of $\alpha_\Lambda = 5$.

Figure 5.2(a) shows the underlying truth log conductivity parameter superimposed

with 159 noisy observational temperature data locations for our test problem. The truth is a log conductivity based on the Internet celebrity cat Benye[1]. We use this underlying truth log conductivity to generate our observational temperature data because, similar to the unknown spatially-distributed parameters found in the inverse problem applications that we target, it is moderately heterogeneous, and has easily identifiable high and low regions.

To generate the data for the MAP estimation problems in this section, a tiny amount of noise at a level of .01% is added to the observational data. Our original full domain mesh contains 937 elements and 513 nodes. The truncated domain mesh for all truncated methods contains 673 elements and 378 nodes (25 shared nodes on the artificial boundary Γ and 353 nodes that are distinct from nodes in the discarded mesh). The discarded domain contains 264 elements and 160 nodes (25 shared nodes on the artificial boundary Γ and 135 nodes that are distinct from nodes in the discarded mesh). The number of basis vectors for $\tilde{\Lambda}_{\mathbf{u}_D}$ in (5.14), where applicable, is $r = 5$.

Figure 5.2(b) shows the full domain method MAP estimate for the full domain inverse problem (2.8). The reconstruction is able to recover parameter features close the observations (the magenta dots on the top and sides in Figure 5.2(a)) but is unable to recover the features in the center of the domain. In particular, the yellow area of highest conductivity above the nose is not recovered.

Figure 5.3(a) is the Hessian at the full domain MAP estimate in Figure 5.2(b). The areas of lowest uncertainty are clearly located near the observations. Following the strategy in section 5.2, this Hessian plot is used to guide truncation to a simply-connected domain of interest that is restricted to an informed region.

Figure 5.3(b) is the inversion result of the sampling DtN method in subsection 5.3.6 over the new truncated domain. The reconstruction does not recover the area of highest

[1]http://www.boredpanda.com/omg-cat-benye/

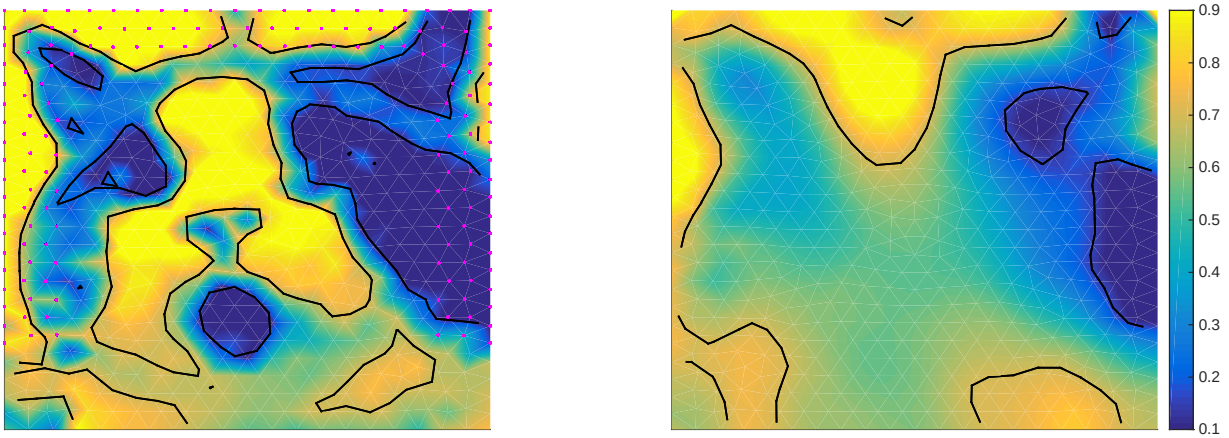

(a) Truth and Observations

(b) Full Domain MAP

Figure 5.2: In inverse problems with large domains and spatially-concentrated observations or dynamics, MAP estimates are often more informative near the observations. Recovery of large areas of high log conductivity can be poor if the areas are far from the observations. In the above example, the observations (magenta dots) are concentrated on top and sides of the domain. The full domain MAP point is unable to recover the center area of high log conductivity. Contour lines at 0.15 and 0.7 are plotted in black.

conductivity around the nose, and is similar to the MAP estimate over the full domain in Figure 5.2(b).

Table 5.1 compares converged MAP estimation results of all inversion methods in sections 5.3 and 5.4 for the elliptic test problem. Error values given are the error compared to the truncated truth and the error compared to the MAP estimate with the truth DtN method of subsection 5.3.5. The history of the alternating DtN method at each inversion stage prior to convergence is shown in Table 5.2 and Figure 5.6.

The offline-computed model-constrained basis (if applicable) and all MAP estimates were obtained using a subspace trust-region inexact Newton-CG method developed in [15, 17, 24, 36, 57]. The convergence tolerance for all methods was 10^{-8} for the norm of the gradient and 10^{-12} for the step and cost function tolerance. Each stage of both the projection and alternating DtN methods is limited to 10 maximum Newton iterations.

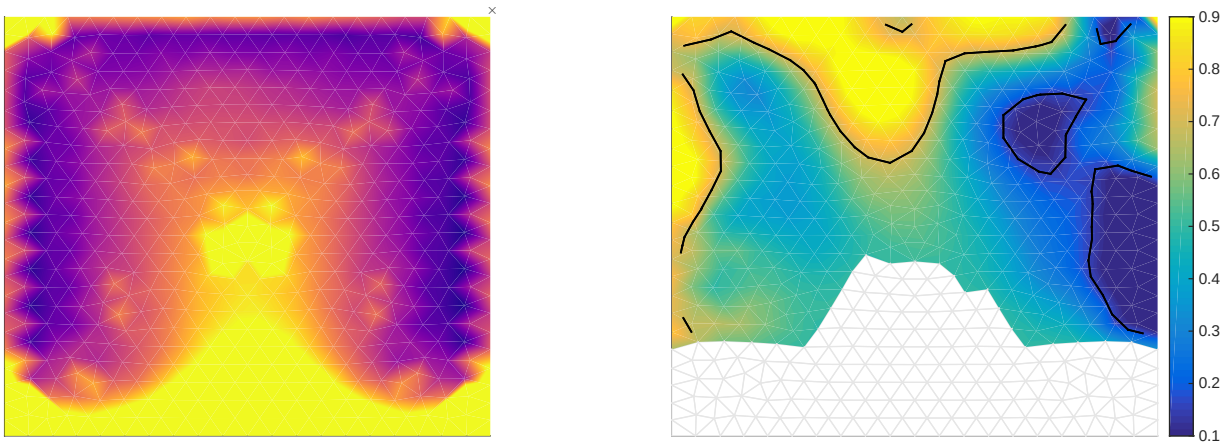

(a) Hessian

(b) Sampling DtN

Figure 5.3: In some inverse problem applications, the truncated domain geometry is decided by the nature of the problem. In others, there is some flexibility in designing the artificial boundary geometry. An uncertainty-guided truncation can create a simply-connected truncated domain that is restricted to more informed regions. On the left is the Hessian at the MAP point (Figure 5.2(b)) for the elliptic test problem. On the right is the MAP point using the sampling DtN method. Contour lines at 0.15 and 0.7 are plotted in black. The resulting estimate is similar to Figure 5.2(b), except that it is obtained on a smaller, more informed domain.

	Full	Samp	Proj	Alt	All	Truth
Offline solves/samples	0	50	50	5365	5365	1
Newton solves	73	93	40	51	25	48
PDE solves	14235	8643	3200	2820	4738	3041
Truth parameter H^1-error	6.191	5.753	5.742	5.714	5.709	5.641
Truth parameter L^2-error	0.378	0.347	0.313	0.298	0.298	0.303
Truth DtN MAP L^2-error	-	0.131	0.146	0.079	0.065	0
CPU time	430.7	322.8	125.7	97.1	184.7	108.6
Time per PDE solve	0.030	0.037	0.039	0.034	0.039	0.036

Table 5.1: Comparison of methods, MAP estimation with the elliptic test problem. A detailed history of the alternating method is in Table 5.2. Full is the full domain method in subsection 5.3.1, Samp is the sampling DtN method in subsection 5.3.6, Proj is the projection DtN method in subsection 5.3.7, Alt is the alternating DtN method in subsection 5.4.2, All is the all-at-once DtN method in subsection 5.4.3, and Truth is the truth DtN method in subsection 5.3.5.

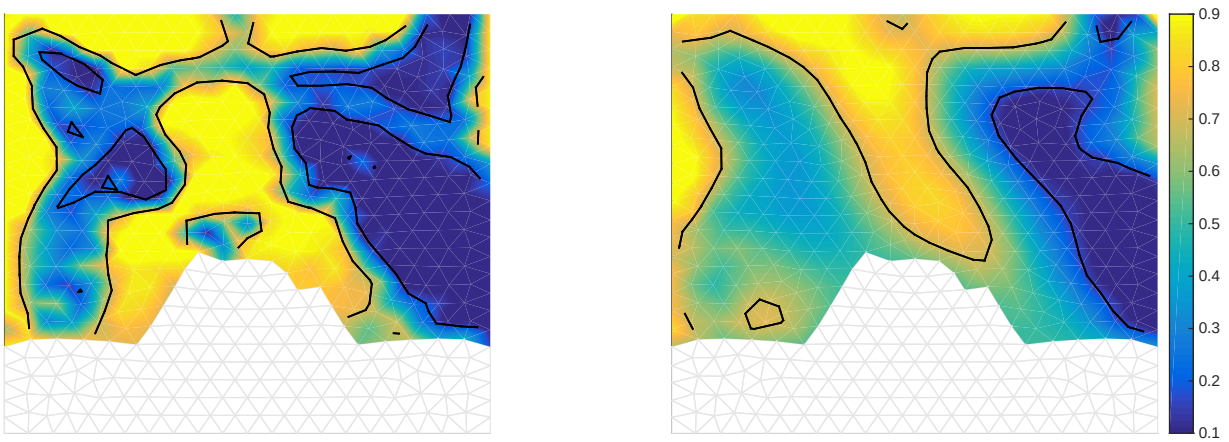

(a) Truncated Truth (b) Truth DtN

Figure 5.4: L^2 errors in Table 5.1 are measured from both the underlying truth log conductivity (left) and from the MAP point using the truth DtN method (right), induced by the truth log conductivity on the discarded domain. Contour lines at 0.15 and 0.7 are plotted in black. The artificial boundary flux defined by the truth DtN function is referred to as the perfect artificial boundary condition. It can be shown that the truncated forward problem solution with this boundary condition is the restriction of the full domain forward solution.

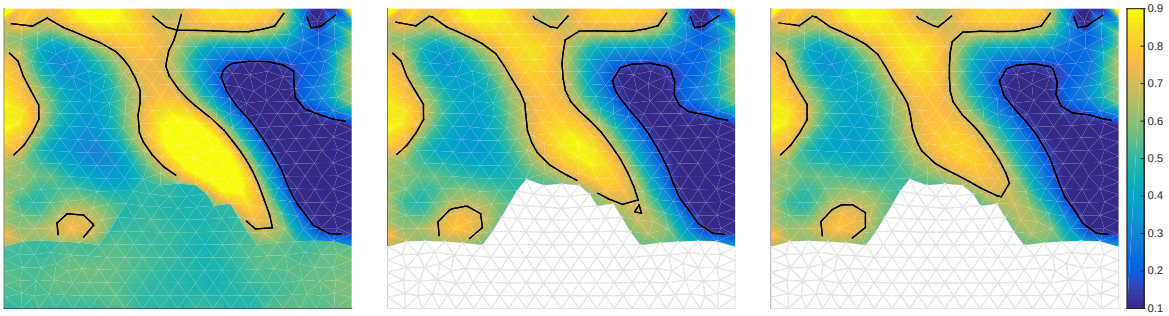

(a) Projection DtN (b) Alternating DtN (c) All-at-once DtN

Figure 5.5: Shown above are MAP estimates using the methods of the present work. The left shows the estimate from using the projection DtN method in subsection 5.3.7 which also computes a low-rank projection estimate of the discarded domain. The center is the estimate from the alternating DtN method in subsection 5.4.2. The right is the estimate using the all-at-once DtN method in subsection 5.4.3.

Stage	1	2	3	4
Newton solves	10	25	39	51
PDE solves	272	892	1769	2820
Truth parameter H^1-error	7.655	7.012	6.527	5.714
Truth parameter L^2-error	0.462	0.353	0.325	0.298
CPU time	11.45	30.20	59.97	97.14

Table 5.2: History for alternating DtN Method. Counts are collected after the parameter inversion stage. Quantities given are cumulative, where applicable.

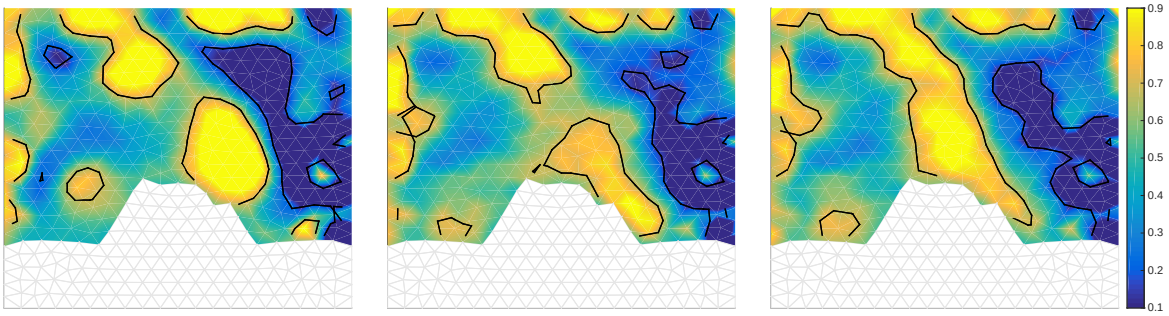

(a) After 1 stage (b) After 2 stages (c) After 3 stages

Figure 5.6: Above are intermediate results from each parameter inversion stage of the alternating DtN method in subsection 5.4.2.

5.5.2 DRAM MCMC

We use the DRAM (delayed rejection, adaptive Metropolis) algorithm [51] to obtain uncertainty quantification results and solve the Bayesian statistical inverse problem. DRAM is a popular state-of-the-art blackbox algorithm for efficient MCMC, and requires only pointwise posterior evaluations.

Due to the difficulty of MCMC with the test problem (requiring many millions of samples for convergence), the numerical results presented in this section solve a slightly "easier" problem than the previous section. That is, we choose the level of parameter prior to be $\alpha = 20$. In the truncated methods that invert for the coefficients c_i of $\tilde{\Lambda}_{\mathbf{u}_D}$ in (5.14) as part of the inverse problem (the sampling, alternating, and all-at-once DtN methods, which use (5.2)), we use a coefficient prior of $\alpha_\Lambda = 0.01$. Each chain is initialized at its respective MAP estimate, which is calculated similarly to the results in subsection 5.5.1.

The converged parameter sample variances $\boldsymbol{\sigma}^2$ are plotted for each method in Figure 5.7. The parameter sample means and credibility envelopes ($\pm\, 2\boldsymbol{\sigma}$) are plotted for each method in Figure 5.8. We do not include the projection DtN method for truncated MAP estimation in our UQ investigation. The projection DtN is a method to iteratively approximate the theoretical truth DtN MAP along with a low-rank estimate of the discarded domain, and it relies on a sequence of previous parameter estimates. Therefore, it only makes sense as a method for deterministic MAP estimation. The extension of the projection DtN to a method for Bayesian inversion is the subject of future work.

The results of solving our elliptic PDE Bayesian inverse problem via converged DRAM sampling are summarized for each method in table 5.3. The computational cost is given in both PDE solves and wall-clock time. UQ results via DRAM were obtained on Stampede2 Intel Xeon Platinum 8160 ("Skylake") nodes at 3.7GHz from the Texas Advanced Computing Center (TACC) at The University of Texas at Austin. Additional DRAM results (comparisons across 1e6, 2e6, 2.5e6 and 3e6 samples) can be found in Appendix B.

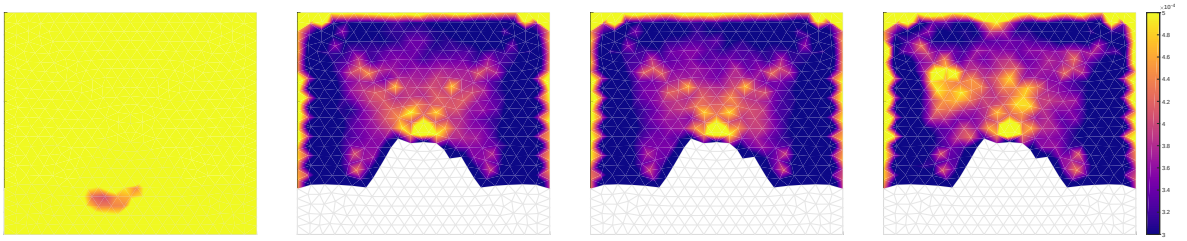

(a) Full, variance (b) Samp, variance (c) All, variance (d) Alt, variance

Figure 5.7: Parameter pointwise variance estimates $\boldsymbol{\sigma}^2$ after DRAM convergence.

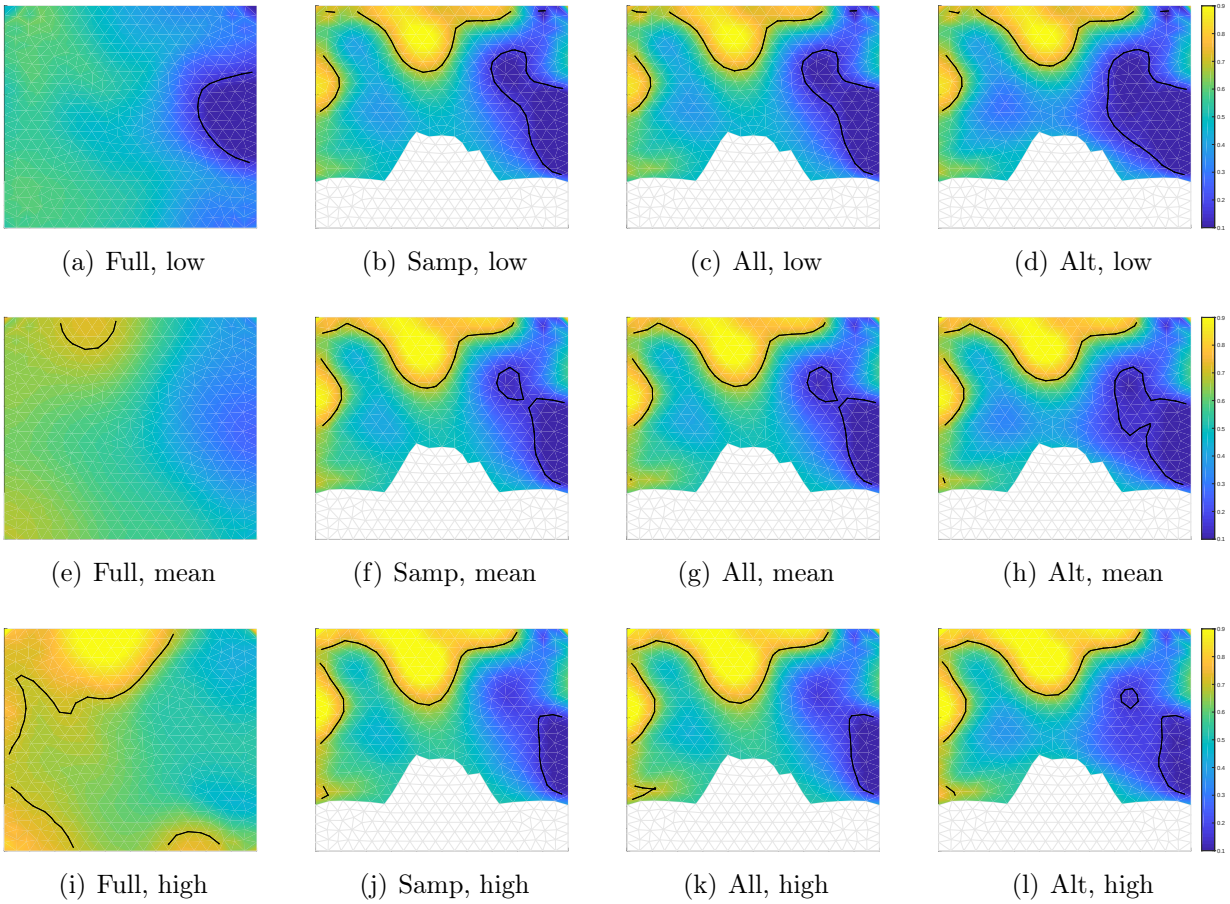

(a) Full, low (b) Samp, low (c) All, low (d) Alt, low

(e) Full, mean (f) Samp, mean (g) All, mean (h) Alt, mean

(i) Full, high (j) Samp, high (k) All, high (l) Alt, high

Figure 5.8: (top row) Low credibility envelope (mean $- 2\boldsymbol{\sigma}$), (middle row) sample mean, and (bottom row) high credibility envelope (mean $+ 2\boldsymbol{\sigma}$) estimates after DRAM convergence. Black contour lines are drawn at 0.15 and 0.7.

Table 5.3: Comparison of converged DRAM sampling results. $\tau(\mathbf{x})$ = estimate of integrated autocorrelation time. ESS = effective sample size = number of samples / $\tau(\mathbf{x})$. Time per IS = Total time/ESS. For fairness of comparison, mean, min, and max here refer to the respective quantities over all 378 nodes in the truncated parameter domain.

Method	Full	Sampling	All-At-Once	Alternating
Offline time (s)	-	-	1,986	1,986
Online time (s)	153,532	91,817	77,424	100,423
Total time (s)	153,532	91,817	79,410	102,409
Samples	3,000,000	2,000,000	2,000,000	2,000,000
PDE solves	5,082,416	3,347,569	3,350,240	7,370,410
$\bar{\tau}$	1,261.8	917.0	896.3	962.2
Min τ	274.6	296.2	258.6	355.6
Max τ	2,598.2	2,405.8	2,332.4	2,490.6
ESS, min	1,154.7	831.3	857.5	803.0
ESS, max	10,923.6	6,753.2	7,735.0	5,623.6
Time per IS, min	14.1	13.6	10.0	17.9
Time per IS, max	133.0	110.4	90.3	125.1

5.6 Discussion of inversion methods

As seen in Table 5.1, using the sampling DtN method for MAP point estimation (to solve the deterministic truncated inverse problem (5.2)) requires fewer PDE solves, results in smaller error values, and takes less time overall than computing the MAP point of the full domain Bayesian inverse problem (2.8). However, for MAP point estimation, the projection DtN, alternating DtN, and all-at-once DtN methods require about half as many PDE solves, result in generally lower error values, and take about half the CPU time as the sampling DtN method.

Furthermore, each of the new methods as seen in Figure 5.5 is able to recover the center area of high conductivity in their converged MAP point estimates. Figure 5.4 shows that this area is also recovered by deterministic inversion with the truth DtN method.

The MAP point method with the fewest PDE solves and fastest CPU time is the alternating DtN method, which takes $2,820$ PDE solves and 97.1 seconds, compared to

$14,235$ PDE solves and 430.7 seconds for the full domain method. The method that takes the fewest Newton solves and has smallest error metrics is the all-at-once DtN method, which takes only 25 Newton solves and has an H^1 error to the underlying truth parameter of 5.709, compared to the full domain method which requires 73 Newton solves and has an H^1 error to the underlying truth parameter of 6.191. Note that both of these methods require 5365 offline solves using the model-constrained optimization described in subsection 5.4.1.

If the offline solve count is tolerable as a one-time cost, and the accuracy or speed of solving the online inverse problem is of paramount importance, then our recommendation is to use the alternating or all-at-once DtN method for MAP point estimation. In particular, the alternating DtN method is a good balance of accuracy and speed, and is the fastest of all the methods tested in Table 5.1. If offline solves are to be avoided, or if a rough estimate of the discarded domain is desired, then we recommend the projection DtN method.

In the solution of the model Bayesian inverse problem with DRAM, the truncated methods clearly show faster convergence, reduced computational cost. Furthermore, we observe improved fidelity and interpretability of results, which we believe is primarily due to removing the uncertain parameter subspace from the posterior space.

By carefully removing only 130 unknown degrees of freedom, from a problem with originally 513 degrees of freedom (about a 25 percent reduction), we reduce our MCMC computation from $153,532/60^2 \approx 43$ supercomputing wall-clock hours to $79,410/60^2 \approx 22$ wall-clock hours—a reduction of about 48 percent. We expect the computational efficiency to improve when the truncated methods here are used to make larger reductions in higher-dimensional model domains. This would be a promising step towards solving intractable yet critical large-scale uncertainty quantification problems.

Chapter 6

Conclusions

This dissertation presents new, mathematically-justified, data-driven reduction strategies towards the tractable solution of large-scale Bayesian inverse and uncertainty quantification problems with heterogeneous spatially-distributed parameters.

Chapter 3 presents a randomized misfit approach for reducing computational complexity induced by big data in general large-scale PDE-constrained inverse problems. The method permits a novel analysis of the stochastic cost function and its minimizer via probabilistic bounds from random projection theory. It is shown that a subgaussian distribution guarantees the solution obtained from the randomized misfit approach will satisfy Morozov's discrepancy principle with a low failure rate (that decays exponentially with respect to the reduced dimension n).

The key to the randomized misfit approach is the identification of the discretized data misfit functional in the formal inverse problem (assuming a standard nonlinear least squares formulation) as a Euclidean distance in high dimensions, and connecting the theory of random projections, which are quasi-orthogonal dimension-reducing transformations that approximately preserve geometric relationships in big data. Using large deviation theory, impact of big data on the overall computational cost estimate is probabilistically quantified. The main contribution is a rigorous mathematical justification for a well-known but heretofore not yet proven observation about simultaneous source methods, which are now used in many seismic data applications such as offshore oil discovery.

It is shown that the stochastically derived method is equivalent to applying a random

projection to the data misfit vector. This results in a stochastic programming-based proof (up to a constant) of a Johnson-Lindenstrauss lemma variant proved previously (see, e.g. [7, 66] for proofs based on combinatorics and communication theory, respectively). Our connection provides two main theoretical insights. The first is intuition into the surprising numerical accuracy with small reduced misfit dimension n. This phenomenon has been noted in related stochastic methods, particularly in random source encoding methods, without theoretical explanation. The second is an intuition into the ubiquitous $\mathcal{O}(1/\sqrt{n})$ factor in Johnson-Lindenstrauss transforms (a rate shown to be tight by [7]) using a Monte Carlo framework.

Chapter 4 presents the randomized geostatistical approach (RGA), a computationally efficient, scalable, and implementation-friendly randomized geostatistical inversion method. The RGA extends the widely used geostatistical approach (GA) and its extensions [73, 74, 75, 84, 127] to geostatistical inverse problems with both high-dimensional parameter dimension P and high-dimensional observed data dimensions N, i.e. $N = \mathcal{O}(10^5 - 10^7)$. To overcome known issues of excessive memory and computational cost that can arise in the geostatistical approaches when dealing with a large number of observations, the RMA is in incorporated into the PCGA, which is a recent randomized blackbox extension of the GA meant to make the GA tractable for problems with high-dimensional parameter spaces and medium dimensional data ($P = \mathcal{O}(10^4 - 10^7)$, $N < \mathcal{O}(10^4)$.

The RGA is a practical data-driven reduction method for big geostatistical data and large-scale geostatistical inversion with a blackbox forward solver. It uses the idea from the RMA that the misfit is a vector in high-dimensional parameter space, and that one can make a justified approximation of the inverse problem, by seeking to approximately minimize the norm of the misfit (and subsequently the cost functional or negative log posterior) using random projections, which can approximately transform a Euclidean norm of a high-dimensional vector in R^N to a low-dimensional space R^n with high probability.

Both the RGA and PCGA generate a surrogate GA cokriging system with a smaller dimension than the original problem. However, a computational cost analysis is given that shows the RGA method yields a smaller problem than the PCGA, when computing the next step in the iterative optimization process. This reduces both the memory and computational costs compared to the PCGA. It is theoretically and numerically demonstrated that RGA can solve a geostatistical inverse problem with $\mathcal{O}(10^7)$ observations using modest computational resources. Therefore, it has potential for practical subsurface heterogeneity characterization in problems with a large number of observations.

The developed truncated inversion methods in Chapter 5 are shown to be potentially more efficient and effective than solving over the full model domain. Motivated by existing domain decomposition strategies for model order reduction, three new domain decomposition-based methods for parameter and state space reduction in large-scale Bayesian inverse problems are proposed. A non-canonical domain truncation strategy is also developed for the goal-oriented reduction. The strategy for truncation is driven by the data locality, and the inversion methods are the projection DtN method, the alternating DtN method, and the all-at-once DtN method.

Existing theory in forward simulation shows that the truncated domain PDE solution using the truth DtN map is exactly the restriction of the full domain PDE solution. Numerical results show that solving an *inverse* problem on the truncated domain can lead to higher fidelity recovery of large high and low areas compared to the original full domain problem, with regards to MAP estimation. Recovery quality varies, depending on the method of DtN MAP estimation. Significantly reduced computation is observed in solving the Bayesian inverse problem with DRAM MCMC sampling. This is due to both the reduced parameter and state dimension and the reduced uncertainty in the posterior. In the truncated problems, the posterior resides in a data- (and model-)informed subspace of the original unknown parameter space.

It is shown that using a greedy, goal-oriented, model-constrained optimization to construct the low-rank DtN basis offline improves reconstruction fidelity and reduces the online computational burden, compared to methods with minimal offline cost. For large-scale inverse problems where detection of high and low regions is critical, and uncertainty quantification where the model is run numerous times over the inversion domain, this offline cost is negligible. If one wishes to avoid offline computation, the projection DtN method is a efficient alternative for MAP point estimation.

A partial answer (pun intended) is given to the larger question of how should inversion results, especially for a spatially-distributed unknown parameter, be interpreted and validated. Against which comparative standard should a reduced model or efficient method validate its uncertainty results? Against the synthetic parameter in the elliptic test problem, the full domain MAP estimate is inaccurate in regions far from the observed data locations.

Therefore, should a truncated or reduced method with a result similar to the full MAP claim success? The full MAP is far from the physical underlying truth! Yet many methods including the presented RMA method are guilty of validating success against the MAP. This is because the inverse problem is ill-posed: the data is limited and noisy, and combined with the level of parameter heterogeneity, it becomes impossible to recover the truth. The MAP is, by definition, the most probable guess of the parameter distribution that we can infer. Yet, it should be understood that it still has room for improvement, especially if the problem is one of national or global importance, such as locating contaminants or a large reservoir of residual oil in the subsurface.

It is shown that that useful information—here, visible high and low regions that correspond to the truth—*and* a decrease in computational expense can result *if* one is willing to make problem-dependent, goal-oriented trade-offs.

Here, the trade-off is forgoing estimation of the non-data-informed spatial regions, and doing the comparatively negligible offline work of truncating the solution mesh and

building a mathematically justified, model-informed artificial boundary condition.

6.1 Coverage of CSEM Areas A, B, and C and their integration

- **Area A**: (*Applicable Mathematics*) This dissertation presents theoretical analysis in the form of probabilistic guarantees for the randomized misfit approach (RMA) for abstract PDE-constrained inverse problems with high-dimensional data. Furthermore, asymptotic computational complexity analysis was carried out for the RMA to demonstrate the efficiency.

- **Area B**: (*Scientific Computation*) This dissertation presents data-driven numerical methods for more efficient MAP point computation and uncertainty quantification in large-scale Bayesian inverse problems, using techniques from machine learning and domain decomposition. Numerical inversion results with an elliptic distributed coefficient nonlinear inverse problem are shown to justify the theoretical claims.

- **Area C**: (*Mathematical Modeling and Application*) This dissertation extends the RMA to a geostatistical inversion method prevalent in subsurface hydrology. The resulting randomized geostatistical approach (RGA) is applied to a transient groundwater flow inverse problem for estimating heterogeneous permeability with observed data dimensions up to $\mathcal{O}(10^7)$. Comparisons to a reference method demonstrate comparable solution quality, computed with a 31x reduction in wall-clock time. Efficiency and scalability is thus shown for practical inverse problems.

The dissertation thus presents an integrated synthesis of theory, algorithms, and applications toward the goal of making the solution of large-scale Bayesian inverse problems tractable in the context of high-dimensional data and high-dimensional parameters.

6.2 Future work

Many new random projections have appeared since the seminal work in [1]. A promising extension of the RMA is to investigate using the positive-definiteness-preserving single-pass sketching matrices, which are elucidated for practical use by the recent paper [141].

Combining dimension reduction and uncertainty quantification is the broader focus of ongoing work towards developing scalable methods for large-scale Bayesian inverse problems in high-dimensional parameter space with big data.

Future tangential work will link and compare different randomization techniques for solving inverse problems in a unified abstract framework.

A future hope is that the RGA method and results will lead to other extensions of the RMA and other domains of application beyond geostatistical inverse problems, as the need continues to grow for practical inversion methods that can extract heterogeneous parameter knowledge from increasingly complex models and big data.

A promising future direction with the truncated inversion methods that should be investigated is an application to large-scale distributed parameter reservoir characterization problems with localized partitioning interwell tracer test data.

Appendices

Appendix A

Infinite-dimensional gradient and Hessian-action for truncated domain inversion

The infinite-dimensional analog to the finite-dimensional truncated MAP estimation problem (2.8) is given by

$$\min_{\mathbf{u},c_j} \mathcal{J}\left(u\left(\mathbf{u},c_j\right)\right) = \frac{1}{2\sigma^2}\sum_{i=1}^{D}\left(u(x_i)-\mathbf{d}\right)^2 + \frac{1}{2}\left(\mathbf{u}-\mathbf{u}_0\right)\mathcal{C}\left(\mathbf{u}-\mathbf{u}_0\right) \tag{A.1}$$

s.t.

$$\int_{\widehat{\Omega}} e^{\mathbf{u}}\nabla u\cdot\nabla\widetilde{v} + \int_{\widehat{\Omega}_{\mathrm{Bi}}} \mathrm{Bi}u\widetilde{v} + \int_{\Gamma}\Lambda u\widetilde{v} = \int_{\Gamma} vf \tag{A.2}$$

where $\int_\Gamma \Lambda u \approx \left(\sum_{j=1}^{N_{\mathrm{ens}}} c_j\Lambda_j u_\Gamma\right)^\top \widetilde{v}_\Gamma$ and the $\{\Lambda_j\}$ are chosen by the model-constrained offline cycle as detailed in subsection 5.4.1. Note that $\int_\Gamma vf \approx \begin{bmatrix}\mathbf{F_1}\\ \mathbf{F_2}\end{bmatrix}$, where $\mathbf{F_2} = -\left(\sum_{j=1}^{N_{\mathrm{ens}}} c_jF_j\right)^\top \widetilde{v}_\Gamma$.

The Lagrangian is given by

$$\begin{aligned}\mathcal{L}\left(u,p,\mathbf{u},c_j\right) =& \frac{1}{2\sigma^2}\left(\sum_{i=1}^{D}u(x_i)-\mathbf{d}\right)^2 + \frac{1}{2}\left(\mathbf{u}-\mathbf{u}_0\right)\mathcal{C}\left(\mathbf{u}-\mathbf{u}_0\right) + \int_{\widehat{\Omega}} e^{\mathbf{u}}\nabla u\cdot\nabla p \\ &+ \int_{\widehat{\Omega}_{\mathrm{Bi}}}\mathrm{Bi}\,u\,p + \left(\sum_{j=1}^{N_{\mathrm{ens}}} c_j\Lambda_j u_\Gamma\right)p|_\Gamma + \left(\sum_{j=1}^{N_{\mathrm{ens}}} c_jF_j\right)^\top p|_\Gamma\end{aligned} \tag{A.3}$$

The forward equation is

$$\int_{\widehat{\Omega}} e^{\mathbf{u}}\nabla u\cdot\nabla\widetilde{p} + \int_{\widehat{\Omega}_{\mathrm{Bi}}}\mathrm{Bi}\,u\,\widetilde{p} + \left(\sum_{j=1}^{N_{\mathrm{ens}}} c_j\Lambda_j u_\Gamma\right)\widetilde{p}|_\Gamma + \left(\sum_{j=1}^{N_{\mathrm{ens}}} c_jF_j\right)^\top \widetilde{p}|_\Gamma = 0. \tag{A.4}$$

The adjoint problem is

$$\int_{\widehat{\Omega}} e^{\mathbf{u}} \nabla \widetilde{u} \cdot \nabla p + \int_{\widehat{\Omega}_{\mathrm{Bi}}} \mathrm{Bi}\, \widetilde{u}\, p + \left(\sum_{j=1}^{N_{\mathrm{ens}}} c_j \Lambda_j p|_{\Gamma} \right) \mathbf{u}|_{\Gamma} + \left(\sum_{j=1}^{N_{\mathrm{ens}}} c_j F_j \right)^{\top} p|_{\Gamma} = \frac{1}{2\sigma^2} \left(\sum_{i=1}^{D} u(x_i) - \mathbf{d} \right)^2 \widetilde{u}(x_i). \tag{A.5}$$

Then, using the standard reduced space approach ([106, 148]) we can show that the gradient $\mathcal{G} := \nabla \mathcal{J}(u)$ (the Fréchet derivative of the cost functional $\mathcal{J}$) acting in any direction $\tilde{u}$ is given by $\begin{bmatrix} \langle \mathcal{G}, \widetilde{\mathbf{u}} \rangle \\ \langle \mathcal{G}, \widetilde{\mathbf{c}} \rangle \end{bmatrix}$, where

$$\langle \mathcal{G}, \widetilde{\mathbf{u}} \rangle = \int_{\widehat{\Omega}} \widetilde{\mathbf{u}} e^{\mathbf{u}} \nabla u \cdot \nabla p + \mathcal{C}(\mathbf{u} - \mathbf{u}_0), \tag{A.6}$$

the k-th component of $\langle \mathcal{G}, \widetilde{\mathbf{c}} \rangle$ is

$$\langle \mathcal{G}, \widetilde{c_k} \rangle = (\Lambda_k u|_{\mathbf{u}})^{\top} p|_{\Gamma} + F_k^{\top} p|_{\Gamma}. \tag{A.7}$$

The Hessian-action is denoted by $\langle \mathcal{H}, \widetilde{\lambda}, \widehat{\lambda} \rangle := \begin{bmatrix} \langle \langle \mathcal{G}, \widetilde{\mathbf{u}} \rangle, \widehat{\lambda} \rangle \\ \langle \langle \mathcal{G}, \widetilde{\mathbf{c}} \rangle, \widehat{\lambda} \rangle \end{bmatrix}$, where $\lambda = \begin{bmatrix} \mathbf{u} \\ \mathbf{c} \end{bmatrix}$ and $\widehat{\lambda} = \begin{bmatrix} \widehat{\mathbf{u}} \\ \widehat{\mathbf{c}} \end{bmatrix}$. Its derivation is similar to the derivation of the gradient and follows from taking the Fréchet derivative of $\langle \mathcal{G}, \widetilde{\mathbf{u}} \rangle$ and $\langle \mathcal{G}, \widetilde{\mathbf{c}} \rangle$ in direction $\widehat{\lambda}$. Then the remaining necessary expressions for the incremental adjoint and forward variables are found by taking the the Fréchet derivative of the adjoint and forward equations in the direction $\widehat{\lambda}$, and solving the resulting systems.

Appendix B

Additional UQ results for truncated domain inversion

Table B.1: DRAM sampling for uncertainty quantification, 1e6 samples.

Method	Full	Sampling	All-At-Once	Alternating
Offline time (s)	-	-	1,986	1,986
Online time (s)	49,710	39,634	36,616	40,676
Total time (s)	49,710	39,634	38,602	42,663
Samples	1,000,000	1,000,000	1,000,000	1,000,000
PDE solves	1,644,982	1,628,904	1,631,553	3,643,884
$\bar{\tau}$	1,128.5	960.2	996.9	942.7
Min τ	376.5	347.0	331.7	348.6
Max τ	2,491.3	2,392.9	2,439.3	2,368.4
ESS, min	401.4	417.9	410.0	422.2
ESS, max	2,655.7	2,882.1	3,014.7	2,868.3
Time per IS, min	18.7	13.8	12.1	14.2
Time per IS, max	123.8	94.8	89.3	96.3

The DRAM sampling UQ results were obtained on Stampede2 Intel Xeon Platinum 8160 ("Skylake") nodes at 3.7GHz. The authors acknowledge the Texas Advanced Computing Center (TACC) at The University of Texas at Austin for providing computing resources that have contributed to the research results reported within this paper. URL: http://www.tacc.utexas.edu.

Table B.2: DRAM sampling for uncertainty quantification, 2e6 samples.

Method	Full	Sampling	All-At-Once	Alternating
Offline time (s)	-	-	1,986	1,986
Online time (s)	115,885	91,817	77,424	100,423
Total time (s)	115,885	91,817	79,410	102,409
Samples	2,000,000	2,000,000	2,000,000	2,000,000
PDE solves	3,351,262	3,347,569	3,350,240	7,370,410
$\bar{\tau}$	1,279.4	917.0	896.3	962.2
Min τ	292.7	296.2	258.6	355.6
Max τ	2,626.1	2,405.8	2,332.4	2,490.6
ESS, min	761.6	831.3	857.5	803.0
ESS, max	6,833.8	6,753.2	7,735.0	5,623.6
Time per IS, min	17.0	13.6	10.0	17.9
Time per IS, max	152.2	110.4	90.3	125.1

Table B.3: DRAM sampling for uncertainty quantification, 2.5e6 samples.

Method	Full	Sampling	All-At-Once	Alternating
Offline time (s)	-	-	1,986	1,986
Online time (s)	127,347	94,682	95,430	102,786
Total time (s)	127,347	94,682	97,416	104,773
Samples	2,500,000	2,500,000	2,500,000	2,500,000
PDE solves	4,214,893	4,216,137	4,218,612	9,241,362
$\bar{\tau}$	1,259.2	983.2	947.7	909.9
Min τ	343.6	285.3	317.6	297.0
Max τ	2,683.7	2,524.6	2,445.2	2,400.8
ESS, min	931.5	990.2	1,022.4	1,041.3
ESS, max	7,276.1	8,762.7	7,871.8	8,418.0
Time per IS, min	17.5	10.8	12.1	12.2
Time per IS, max	136.7	95.6	93.3	98.7

Table B.4: DRAM sampling for uncertainty quantification, 3e6 samples.

Method	Full	Sampling	All-At-Once	Alternating
Offline time (s)	-	-	1,986	1,986
Online time (s)	153,532	115,283	114,544	124,230
Total time (s)	153,532	115,283	116,530	126,216
Samples	3,000,000	3,000,000	3,000,000	3,000,000
PDE solves	5,082,416	5,087,980	5,091,146	11,115,386
$\bar{\tau}$	1,261.8	923.9	1,100.2	931.8
Min τ	274.6	337.8	317.1	305.0
Max τ	2,598.2	2,196.4	2,669.3	2,475.6
ESS, min	1,154.7	1,365.9	1,123.9	1,211.8
ESS, max	10,923.6	8,880.4	9,460.7	9,835.5
Time per IS, min	14.1	13.0	12.1	12.6
Time per IS, max	133.0	84.4	101.9	102.5

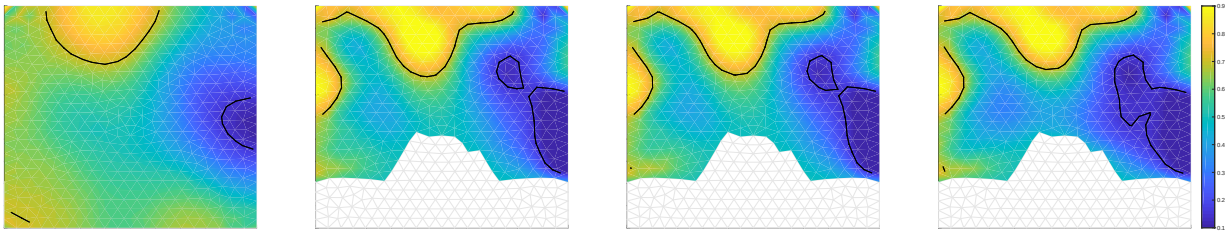

(a) Full, 1e6 (b) Samp, 1e6 (c) All, 1e6 (d) Alt, 1e6

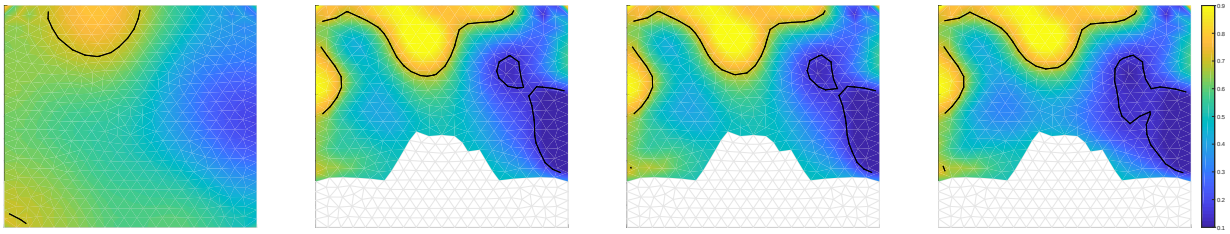

(e) Full, 2e6 (f) Samp, 2e6 (g) All, 2e6 (h) Alt, 2e6

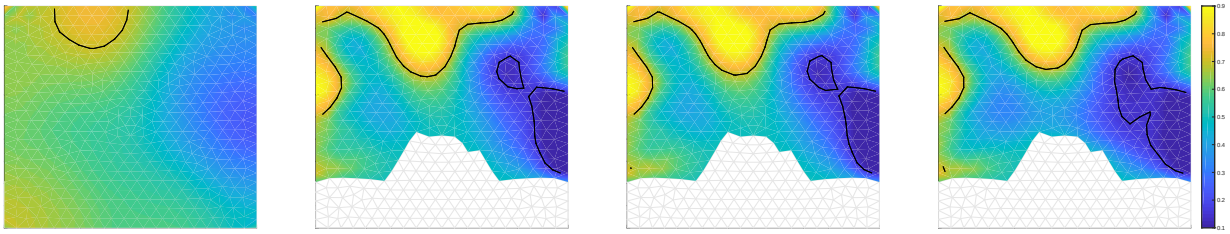

(i) Full, 2.5e6 (j) Samp, 2.5e6 (k) All, 2.5e6 (l) Alt, 2.5e6

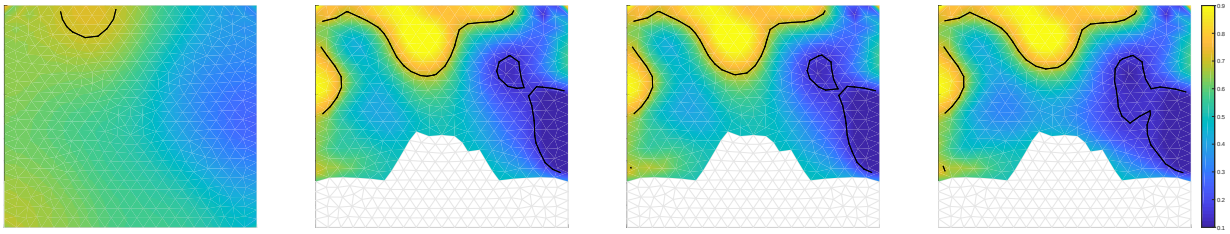

(m) Full, 3e6 (n) Samp, 3e6 (o) All, 3e6 (p) Alt, 3e6

Figure B.1: Posterior mean estimates after 1e6, 3e6, 2.5e6, 3e6 DRAM samples.

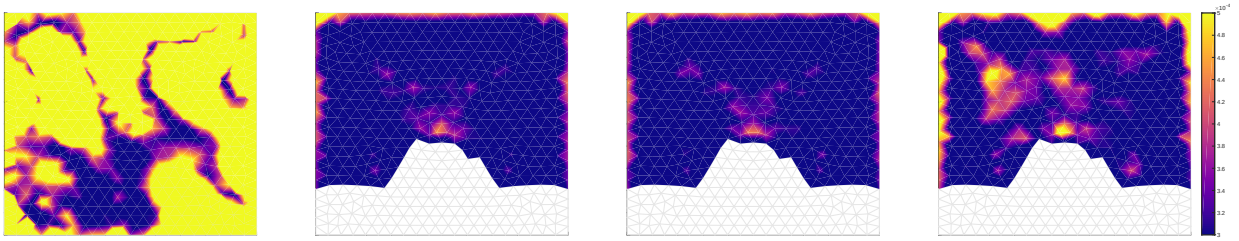

(a) Full, 1e6 (b) Samp, 1e6 (c) All, 1e6 (d) Alt, 1e6

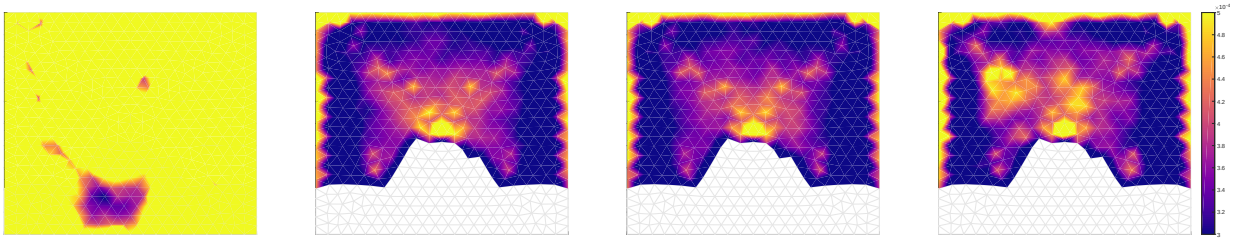

(e) Full, 2e6 (f) Samp, 2e6 (g) All, 2e6 (h) Alt, 2e6

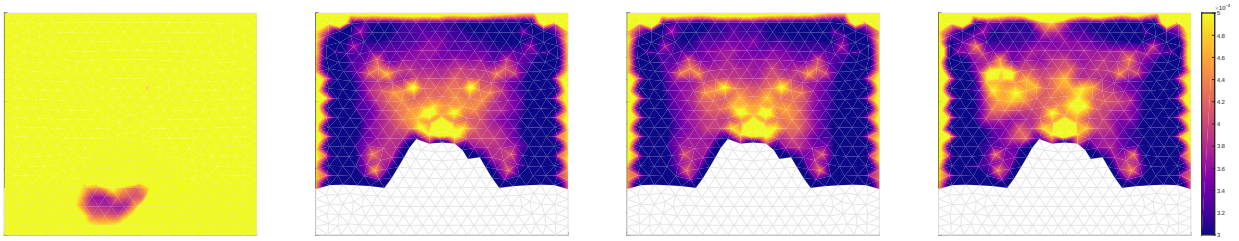

(i) Full, 2.5e6 (j) Samp, 2.5e6 (k) All, 2.5e6 (l) Alt, 2.5e6

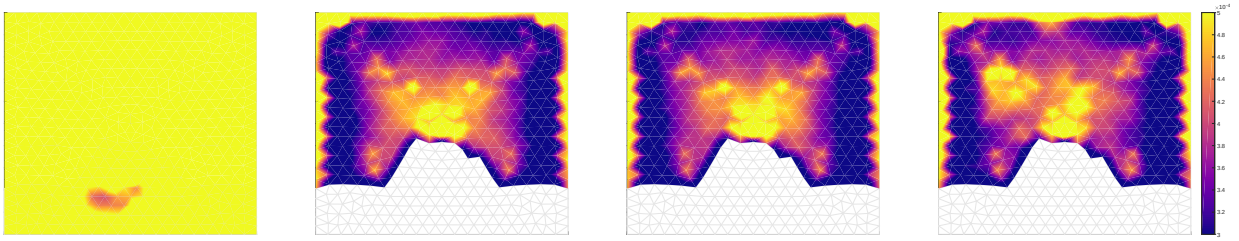

(m) Full, 3e6 (n) Samp, 3e6 (o) All, 3e6 (p) Alt, 3e6

Figure B.2: Posterior pointwise variance estimates after 1e6, 2e6, 2.5e6, 3e6 DRAM samples.

Bibliography

[1] D. Achlioptas. Database-friendly random projections: Johnson-Lindenstrauss with binary coins. *Journal of Computer and System Sciences*, 66:671–687, 2003.

[2] M. Adams, J. Berger, D. Bingham, W. Chen, R. Ghanem, O. Ghattas, D. Higdon, J. Meza, E. Michielssen, V. Nair, C. Nakhleh, D. Nychka, S. Pollock, H. Stone, A. Wilson, and M. Zika. Assessing the reliability of complex models: Mathematical and statistical foundations of verification, validation, and uncertainty quantification. Report of the National Academies Committee on mathematical foundations of verification, validation, and uncertainty quantification. National Academies Press, March 2012.

[3] N. Ailon and B. Chazelle. The fast Johnson-Lindenstrauss transform and approximate nearest neighbors. *SIAM Journal on Computing*, 39(1):302–322, 2009.

[4] F. Alexander, M. Anitescu, J. Bell, D. Brown, M. Ferris, M. Luskin, S. Mehrotra, B. Moser, A. Pinar, A. Tartakovsky, K. Willcox, S. Wright, and V. Zavala. A multifaceted mathematical approach for complex systems: Report of the DOE workshop on mathematics for the analysis, simulation, and optimization of complex systems. Workshop Report, Department of Energy, September 2011.

[5] A. Alexanderian, N. Petra, G. Stadler, and O. Ghattas. A-optimal design of experiments for infinite-dimensional Bayesian linear inverse problems with regularized ℓ_0-sparsification. *SIAM Journal on Scientific Computing*, 36(5):A2122–A2148, 2014.

[6] A. Alexanderian, N. Petra, G. Stadler, and O. Ghattas. A fast and scalable method for A-optimal design of experiments for infinite-dimensional Bayesian nonlinear inverse problems. *SIAM Journal on Scientific Computing*, 38(1):A243–A272, 2016.

[7] N. Alon. Problems and results in extremal combinatorics. *Discrete Mathematics*, 273 (1):31–53, 2003.

[8] S. Ambikasaran, J. Y. Li, P. K. Kitanidis, and E. Darve. Large-scale stochastic linear inversion using hierarchical matrices. *Computational Geosciences*, 17(6):913–927, 2013.

[9] A. Aravkin, M. P. Friedlander, F. J. Herrmann, and T. Van Leeuwen. Robust inversion, dimensionality reduction, and randomized sampling. *Mathematical Programming*, 134 (1):101–125, 2012.

[10] J. Baiges, R. Codina, and S. Idelsohn. A domain decomposition strategy for reduced order models. Application to the incompressible Navier-Stokes equations. *Computer Methods in Applied Mechanics and Engineering*, 267:23–42, 2013.

[11] J. Bear and A. H. Cheng. *Modeling Groundwater Flow and Contaminant Transport*, volume 23. Springer Science & Business Media, 2010.

[12] M. Bebendorf. *Hierarchical Matrices: A Means to Efficiently Solve Elliptic Boundary Value Problems*, volume 63. Springer, New York, 2008.

[13] J. Bezanson, A. Edelman, S. Karpinski, and V. B. Shah. Julia: A fresh approach to numerical computing., 2014.

[14] S. Borm, L. Grasedyck, and W. Hackbusch. Introduction to hierarchical matrices with applications. *Engineering Analysis with Boundary Elements*, 5(27):405–422, 2003.

[15] M. A. Branch, T. F. Coleman, and Y. Li. A subspace, interior, and conjugate gradient method for large-scale bound-constrained minimization problems. *SIAM Journal on Scientific Computing*, 21(1):1–23 (electronic), 1999.

[16] M. Buffoni, H. Telib, and A. Iollo. Iterative methods for model reduction by domain decomposition. *Computers & Fluids*, 38(6):1160–1167, 2009.

[17] T. Bui-Thanh. *Model-constrained optimization methods for reduction of parameterized large-scale systems*. PhD thesis, Department of Aeronautics and Astronautics, MIT, 2007.

[18] T. Bui-Thanh and O. Ghattas. Analysis of the Hessian for inverse scattering problems. Part II: Inverse medium scattering of acoustic waves. *Inverse Problems*, 28(5):055002, 2012.

[19] T. Bui-Thanh and O. Ghattas. Analysis of the Hessian for inverse scattering problems. Part I: Inverse shape scattering of acoustic waves. *Inverse Problems*, 28(5):055001, 2012.

[20] T. Bui-Thanh and O. Ghattas. A scaled stochastic Newton algorithm for Markov chain Monte Carlo simulations. *Submitted to SIAM Journal of Uncertainty Quantification*, 2012.

[21] T. Bui-Thanh and O. Ghattas. Analysis of the Hessian for inverse scattering problems. Part III: Inverse medium scattering of electromagnetic waves in three dimensions. *Inverse Problems and Imaging*, 7(4):1139–1155, 2013.

[22] T. Bui-Thanh and M. A. Girolami. Solving large-scale PDE-constrained Bayesian inverse problems with Riemann manifold Hamiltonian Monte Carlo. *Inverse Problems*, 30(11):114014, 2014.

[23] T. Bui-Thanh and Q. P. Nguyen. Fem-based discretization-invariant mcmc methods for pde-constrained bayesian inverse problems. *Inverse Problems and Imaging*, 10(4): 943–975, 2016.

[24] T. Bui-Thanh, K. Willcox, and O. Ghattas. Model reduction for large-scale systems with high-dimensional parametric input space. *SIAM Journal on Scientific Computing*, 30:3270–3288, 2008.

[25] T. Bui-Thanh, C. Burstedde, O. Ghattas, J. Martin, G. Stadler, and L. C. Wilcox. Extreme-scale UQ for Bayesian inverse problems governed by PDEs. In *Proceedings of the International Conference on High Performance Computing, Networking, Storage and Analysis*, SC '12, pages 3:1–3:11, Los Alamitos, CA, USA, 2012. IEEE Computer Society Press.

[26] T. Bui-Thanh, O. Ghattas, J. Martin, and G. Stadler. A computational framework for infinite-dimensional Bayesian inverse problems Part I: The linearized case, with application to global seismic inversion. *SIAM Journal on Scientific Computing*, 35(6): A2494–A2523, 2013.

[27] D. Calvetti, D. McGivney, and E. Somersalo. Left and right preconditioning for electrical impedance tomography with structural information. *Inverse Problems*, 28(5): 055015, 2012.

[28] D. Calvetti, P. J. Hadwin, J. M. Huttunen, D. Isaacson, J. P. Kaipio, D. McGivney, E. Somersalo, and J. Volzer. Artificial boundary conditions and domain truncation in electrical impedance tomography. Part I: Theory and preliminary results. *Inverse Problems and Imaging*, 9(3):749–766, 2015.

[29] D. Calvetti, P. J. Hadwin, J. M. Huttunen, J. P. Kaipio, and E. Somersalo. Artificial boundary conditions and domain truncation in electrical impedance tomography. Part II: Stochastic extension of the boundary map. *Inverse Problems and Imaging*, 9(3): 767–789, 2015.

[30] E. Candés and J. Romberg. Sparsity and incoherence in compressive sampling. *Inverse problems*, 23(3):969, 2007.

[31] M. Cardiff, W. Barrash, and P. K. Kitanidis. Hydraulic conductivity imaging from

3-D transient hydraulic tomography at several pumping/observation densities. *Water Resources Research*, 49(11):7311–7326, 2013.

[32] J. Carrera and S. P. Neuman. Estimation of aquifer parameters under transient and steady state conditions: 1. Maximum likelihood method incorporating prior information. *Water Resources Research*, 22(2):199–210, 1986.

[33] J. Carrera, A. Alcolea, A. Medina, J. Hidalgo, and L. J. Slooten. Inverse problem in hydrogeology. *Hydrogeology Journal*, 13(1):206–222, 2005.

[34] S. Chaillat and G. Biros. FaIMS: A fast algorithm for the inverse medium problem with multiple frequencies and multiple sources for the scalar Helmholtz equation. *Journal of Computational Physics*, 231(20):4403–4421, 2012.

[35] O. A. Cirpka and P. K. Kitanidis. Sensitivity of temporal moments calculated by the adjoint-state method and joint inversing of head and tracer data. *Advances in Water Resources*, 24(1):89 – 103, 2000.

[36] T. F. Coleman and Y. Li. An interior trust region approach for nonlinear minimization subject to bounds. *SIAM Journal on Optimization*, 6:418–445, 1996.

[37] P. G. Constantine, E. Dow, and Q. Wang. Active subspace methods in theory and practice: Applications to kriging surfaces. *SIAM Journal on Scientific Computing*, 36 (4):A1500–A1524, 2014.

[38] P. G. Constantine, C. Kent, and T. Bui-Thanh. Accelerating markov chain monte carlo with active subspaces. *SIAM Journal on Scientific Computing*, 38(5):A2779–A2805, 2016.

[39] A. Corigliano, M. Dossi, and S. Mariani. Model order reduction and domain decomposition strategies for the solution of the dynamic elastic–plastic structural problem. *Computer Methods in Applied Mechanics and Engineering*, 290:127–155, 2015.

[40] B. Crestel. *Advanced techniques for multi-source, multi-parameter, and multi-physics inverse problems*. PhD thesis, The University of Texas at Austin, 2017.

[41] T. Cui, J. Martin, Y. M. Marzouk, A. Solonen, and A. Spantini. Likelihood-informed dimension reduction for nonlinear inverse problems. *Inverse Problems*, 30(11):114015, 2014.

[42] S. Dirksen. Dimensionality reduction with subgaussian matrices: A unified theory. *Foundations of Computational Mathematics*, 16(5):1367–1396, 2016.

[43] T. T. Do, L. Gan, N. H. Nguyen, and T. D. Tran. Fast and efficient compressive sensing using structurally random matrices. *IEEE Transactions on Signal Processing*, 60(1):139–154, 2012.

[44] R. Duraiswami, K. Sarkar, and G. L. Chahine. Efficient 2D and 3D electrical impedance tomography using dual reciprocity boundary element techniques. *Engineering Analysis with Boundary Elements*, 22(1):13–31, 1998.

[45] H. W. Engl, M. Hanke, and A. Neubauer. *Regularization of Inverse Problems*. Kluwer Academic Publishers, 1996.

[46] J. R. Finkel, A. Kleeman, and C. D. Manning. Efficient, feature-based, conditional random field parsing. In *Proceedings of ACL-08: HLT*, volume 46, pages 959–967, 2008.

[47] H. P. Flath, L. C. Wilcox, V. Akçelik, J. Hill, B. van Bloemen Waanders, and O. Ghattas. Fast algorithms for Bayesian uncertainty quantification in large-scale linear inverse problems based on low-rank partial Hessian approximations. *SIAM Journal on Scientific Computing*, 33(1):407–432, 2011.

[48] J. E. Fowler and Q. Du. Anomaly detection and reconstruction from random projections. *IEEE Transactions on Image Processing*, 21(1):184–195, 2012.

[49] G. M. Fung and O. L. Mangasarian. Multicategory proximal support vector machine classifiers. *Machine learning*, 59(1-2):77–97, 2005.

[50] G. H. Golub and C. F. Van Loan. *Matrix Computations*. The Johns Hopkins University Press, third edition, 1996.

[51] H. Haario, M. Laine, A. Miravete, and E. Saksman. DRAM: Efficient adaptive MCMC. *Statistics and Computing*, 16:339–354, 2006.

[52] E. Haber, U. M. Ascher, and D. W. Oldenburg. Inversion of 3D electromagnetic data in frequency and time domain using an inexact all-at-once approach. *Geophysics*, 69 (5):1216–1228, 2004.

[53] E. Haber, S. Heldmann, and U. Ascher. Adaptive finite volume method for distributed non-smooth parameter identification. *Inverse Problems*, 23(4):1659–1676, 2007.

[54] E. Haber, M. Chung, and F. Herrmann. An effective method for parameter estimation with PDE constraints with multiple right-hand sides. *SIAM Journal on Optimization*, 22(3):739–757, 2012.

[55] N. Halko, P.-G. Martinsson, and J. A. Tropp. Finding structure with randomness: Probabilistic algorithms for constructing approximate matrix decompositions. *SIAM Review*, 53(2):217–288, 2011.

[56] A. Hauptmann, M. Santacesaria, and S. Siltanen. Direct inversion from partial-boundary data in electrical impedance tomography. *arXiv preprint arXiv:1605.01309*, 2016.

[57] M. Heinkenschloss, M. Ulbrich, and S. Ulbrich. Superlinear and quadratic convergence of affine-scaling interior-point Newton methods for problems with simple bounds without strict complementarity assumption. *Mathematical Programming*, 86:615–635, 1999.

[58] F. J. Herrmann, Y. A. Erlangga, and T. T. Lin. Compressive simultaneous full-waveform simulation. *Geophysics*, 74(4):A35–A40, 2009.

[59] D. Higdon, R. Klein, M. Anderson, M. Berliner, C. Covey, O. Ghattas, C. Graziani, S. Habib, M. Seager, J. Sefcik, P. Stark, and J. Stewart. Uncertainty quantification and error analysis. DOE Extreme Scale Computing Reports, December 2009.

[60] V. Holub and J. Fridrich. Random projections of residuals for digital image steganalysis. *Information Forensics and Security, IEEE Transactions on*, 8(12):1996–2006, 2013.

[61] R. J. Hunt, J. Doherty, and M. J. Tonkin. Are models too simple? Arguments for increased parameterization. *Groundwater*, 45:254–262, 2007.

[62] M. F. Hutchinson. A stochastic estimator of the trace of the influence matrix for Laplacian smoothing splines. *Communications in Statistics-Simulation and Computation*, 19(2):433–450, 1990.

[63] W. A. Illman, S. J. Berg, and Z. Zhao. Should hydraulic tomography data be interpreted using geostatistical inverse modeling? A laboratory sandbox investigation. *Water Resources Research*, 51(5):3219–3237, 2015.

[64] P. Indyk and A. Naor. Nearest-neighbor-preserving embeddings. *ACM Transactions on Algorithms*, 3(3):31, 2007.

[65] T. Isaac, N. Petra, G. Stadler, and O. Ghattas. Scalable and efficient algorithms for the propagation of uncertainty from data through inference to prediction for large-scale

problems, with application to flow of the Antarctic ice sheet. *Journal of Computational Physics*, 296:348–368, 2015.

[66] T. Jayram and D. P. Woodruff. Optimal bounds for Johnson-Lindenstrauss transforms and streaming problems with subconstant error. *ACM Transactions on Algorithms*, 9 (3):26, 2013.

[67] E. Jonsson. *Partial Dirichlet to Neumann maps in the approximate reconstruction of conductivity distributions*. PhD thesis, Rensselaer Polytechnic Institute, Troy, NY, 1997.

[68] E. Jonsson. Electrical conductivity reconstruction using nonlocal boundary conditions. *SIAM Journal on Applied Mathematics*, 59(5):1582–1598, 1999.

[69] J. Kaipio and E. Somersalo. *Statistical and Computational Inverse Problems*, volume 160 of *Applied Mathematical Sciences*. Springer-Verlag, New York, 2005.

[70] J. P. Kaipio, V. Kolehmainen, E. Somersalo, and M. Vauhkonen. Statistical inversion and Monte Carlo sampling methods in electrical impedance tomography. *Inverse Problems*, 16(5):1487, 2000.

[71] F. P. Kelly. Effective bandwidths at multi-class queues. *Queueing systems*, 9(1-2): 5–15, 1991.

[72] P. Kitanidis. *Introduction to Geostatistics: Applications to Hydrogeology*. Stanford-Cambridge program. Cambridge University Press, 1997.

[73] P. Kitanidis and J. Lee. Principal Component Geostatistical Approach for large-dimensional inverse problems. *Water Resources Research*, 50(7):5428–5443, 2014.

[74] P. K. Kitanidis. Quasi-linear geostatistical theory for inversing. *Water Resources Research*, 31(10):2411–2419, 1995.

[75] P. K. Kitanidis. On the geostatistical approach to the inverse problem. *Advances in Water Resources*, 19(6):333–342, 1996.

[76] P. K. Kitanidis. The minimum structure solution to the inverse problem. *Water Resources Research*, 33(10):2263–2272, 1997.

[77] P. K. Kitanidis. Generalized priors in Bayesian inversion problems. *Advances in Water Resources*, 36:3–10, 2012.

[78] A. J. Kleywegt, A. Shapiro, and T. Homem-de Mello. The sample average approximation method for stochastic discrete optimization. *SIAM Journal on Optimization*, 12 (2):479–502, 2002.

[79] T. J. Kneafsey, K. Pruess, M. J. O'Sullivan, and G. S. Bodvarsson. Geothermal reservoir simulation to enhance confidence in predictions for nuclear waste disposal. *Lawrence Berkeley National Laboratory*, 2002.

[80] D. Komatitsch, S. Tsuboi, C. Ji, and J. Tromp. A 14.6 billion degrees of freedom, 5 teraflops, 2.5 terabyte earthquake simulation on the Earth Simulator. In *Supercomputing, 2003 ACM/IEEE Conference*, pages 4–4, Nov 2003.

[81] J. R. Krebs, J. E. Anderson, D. Hinkley, R. Neelamani, S. Lee, A. Baumstein, and M.-D. Lacasse. Fast full-wavefield seismic inversion using encoded sources. *Geophysics*, 74(6):WCC177–WCC188, 2009.

[82] J. R. Krebs, J. E. Anderson, R. Neelamani, C. Jing, D. Hinkley, T. A. Dickens, C. E. Krohn, and P. Traynin. Iterative inversion of data from simultaneous geophysical sources, Feb. 21 2012. US Patent 8,121,823.

[83] E. B. Le, A. Myers, T. Bui-Thanh, and Q. P. Nguyen. A data-scalable randomized misfit approach for solving large-scale PDE-constrained inverse problems. *Inverse Problems*, 33(6):065003, 2017.

[84] J. Lee and P. K. Kitanidis. Large-scale hydraulic tomography and joint inversion of head and tracer data using the Principal Component Geostatistical Approach (PCGA). *Water Resources Research*, 50:5410–5427, 2014.

[85] J. Lee, H. Yoon, P. K. Kitanidis, C. J. Werth, and A. J. Valocchi. Scalable subsurface inverse modeling of huge data sets with an application to tracer concentration breakthrough data from magnetic resonance imaging. *Water Resources Research*, 2016.

[86] P. Li, T. J. Hastie, and K. W. Church. Very sparse random projections. In *Proceedings of the 12th ACM SIGKDD International Conference on Knowledge Discovery and Data Mining*, KDD '06, pages 287–296, New York, NY, USA, 2006. ACM.

[87] Y. Lin, D. O'Malley, and V. V. Vesselinov. A computationally efficient parallel Levenberg-Marquardt algorithm for highly parameterized inverse model analyses. *Water Resources Research*, 52:6948–6977, 2016.

[88] Y. Lin, E. B. Le, D. O'Malley, V. V. Vesselinov, and T. Bui-Thanh. Large-scale inverse model analyses employing fast randomized data reduction. *Water Resources Research*, 53(8):6784–6801, 2017.

[89] F. Lindgren, H. Rue, and J. Lindström. An explicit link between Gaussian fields and Gaussian Markov random fields: the stochastic partial differential equation approach. *Journal of the Royal Statistical Society: Series B (Statistical Methodology)*, 73(4):423–498, 2011.

[90] A. Lipponen, A. Seppänen, and J. Kaipio. Electrical impedance tomography imaging with reduced-order model based on proper orthogonal decomposition. *Journal of Electronic Imaging*, 22(2):023008–023008, 2013.

[91] L. Liu, P. Fieguth, D. Clausi, and G. Kuang. Sorted random projections for robust rotation-invariant texture classification. *Pattern Recognition*, 45(6):2405–2418, 2012.

[92] X. Liu, Q. Zhou, J. T. Birkholzer, and W. A. Illman. Geostatistical reduced-order models in underdetermined inverse problems. *Water Resources Research*, 59:6587–6600, 2013.

[93] X. Liu, Q. Zhou, P. K. Kitanidis, and J. T. Birkholzer. Fast iterative implementation of large-scale nonlinear geostatistical inverse modeling. *Water Resources Research*, 50: 198–207, 2014.

[94] J. R. Martin. *A computational framework for the solution of infinite-dimensional Bayesian statistical inverse problems with application to global seismic inversion*. PhD thesis, The University of Texas at Austin, 2015.

[95] P. G. Martinsson, V. Rokhlin, and M. Tygert. A randomized algorithm for the decomposition of matrices. *Applied and Computational Harmonic Analysis*, 30(1):47–68, 2011.

[96] J. Matousek. On variants of the Johnson-Lindenstrauss lemma. *Random Struct. Algorithms*, 33(2):142–156, 2008.

[97] D. McGivney. *Statistical preconditioning and quantitative imaging for electrical impedance tomography*. PhD thesis, Case Western Reserve University, 2013.

[98] A. M. Michalak, L. Bruhwiler, and P. P. Tans. A geostatistical approach to surface flux estimation of atmospheric trace gases. *Journal of Geophysical Research*, 109, 07 2004.

[99] P. P. Moghaddam and F. J. Herrmann. Randomized full-waveform inversion: A dimensionality-reduction approach. In *2010 SEG Annual Meeting*. Society of Exploration Geophysicists, 2010.

[100] A. Mondal. *Bayesian Uncertainty Quantification for Large Scale Spatial Inverse Problems*. PhD thesis, Texas A & M University, 2012.

[101] V. A. Morozov. On the solution of functional equations by the method of regularization. *Soviet Mathematics - Doklady*, 7(1):414–417, 1966.

[102] R. Neelamani, C. E. Krohn, J. R. Krebs, J. K. Romberg, M. Deffenbaugh, and J. E. Anderson. Efficient seismic forward modeling using simultaneous random sources and sparsity. *Geophysics*, 75(6):WB15–WB27, 2010.

[103] A. Nemirovski, A. Juditsky, G. Lan, and A. Shapiro. Robust stochastic approximation approach to stochastic programming. *SIAM Journal on Optimization*, 19(4):1574–1609, 2009.

[104] S. P. Neuman and S. Yakowitz. A statistical approach to the inverse problem of aquifer hydrology: 1. Theory. *Water Resources Research*, 15(4):845–860, 1979.

[105] S. P. Neuman, G. E. Fogg, and E. A. Jacobson. A statistical approach to the inverse problem of aquifer hydrology: 2. Case study. *Water Resources Research*, 16(1):33–58, 1980.

[106] J. Nocedal and S. J. Wright. *Numerical Optimization*. Springer Verlag, Berlin, Heidelberg, New York, 1999.

[107] J. Nocedal and S. J. Wright. *Numerical Optimization*. Springer-Verlag New York, second edition, 2006.

[108] W. Nowak and O. A. Cirpka. A modified Levenberg-Marquardt algorithm for quasi-linear geostatistical inversing. *Advances in Water Resources*, 27:737–750, 2004.

[109] W. Nowak and O. A. Cirpka. Geostatistical inference of hydraulic conductivity and dispersivities from hydraulic heads and tracer data. *Water Resources Research*, 42(8): W08416, 2006.

[110] W. Nowak, S. Tenkleve, and O. A. Cirpka. Efficient computation of linearized cross-covariance and auto-covariance matrices of interdependent quantities. *Mathematical Geology*, 35(1):53–66, 2003.

[111] D. W. Oldenburg, E. Haber, and R. Shekhtman. Three dimensional inversion of multisource time domain electromagnetic data. *Geophysics*, 78(1):E47–E57, 2012.

[112] C. C. Paige and M. A. Saunders. Solution of sparse indefinite systems of linear equations. *SIAM Journal on Numerical Analysis*, 12(4):617–629, 1975.

[113] H. O. Peitgen and D. Saupe. *The Science of Fractal Images*. Springer-Verlag New York, 1988.

[114] N. Petra, J. Martin, G. Stadler, and O. Ghattas. A computational framework for infinite-dimensional Bayesian inverse problems: Part II. Stochastic Newton MCMC with application to ice sheet inverse problems. *SIAM Journal on Scientific Computing*, 36(4):A1525–A1555, 2014.

[115] R. G. Pratt. Seismic waveform inversion in the frequency domain, Part 1: Theory and verification in a physical scale model. *Geophysics*, 64(3):888–901, 1999.

[116] K. Pruess. *Mathematical Modeling of Fluid Flow and Heat Transfer in Geothermal Systems: An Introduction in Five Lectures*. United Nations University, Geothermal Training Programme, 2002.

[117] T. E. Reilly. *System and boundary conceptualization in ground-water flow simulation*, volume 3. US Geological Survey, 2001.

[118] F. Roosta-Khorasani. *Randomized algorithms for solving large scale nonlinear least squares problems*. PhD thesis, University of British Columbia, 2015.

[119] F. Roosta-Khorasani and U. Ascher. Improved bounds on sample size for implicit matrix trace estimators. *Foundations of Computational Mathematics*, 15(5):1187–1212, 2015.

[120] F. Roosta-Khorasani, K. van den Doel, and U. Ascher. Stochastic algorithms for inverse problems involving PDEs and many measurements. *SIAM Journal on Scientific Computing*, 36(5):S3–S22, 2014.

[121] F. Roosta-Khorasani, K. Van Den Doel, and U. Ascher. Data completion and stochastic algorithms for PDE inversion problems with many measurements. *Electron. Trans. Numer. Anal*, 42:177–196, 2014.

[122] F. Roosta-Khorasani, G. J. Székely, and U. M. Ascher. Assessing stochastic algorithms for large scale nonlinear least squares problems using extremal probabilities of linear combinations of gamma random variables. *SIAM/ASA Journal on Uncertainty Quantification*, 3(1):61–90, 2015.

[123] P. S. Routh, S. Lee, R. Neelamani, J. R. Krebs, S. Lazaratos, and C. Marcinkovich. Simultaneous source encoding and source separation as a practical solution for full wavefield inversion, July 8 2014. US Patent 8,775,143.

[124] U. Rude, K. Willcox, L. C. McInnes, H. D. Sterck, G. Biros, H. Bungartz, J. Corones, E. Cramer, J. Crowley, O. Ghattas, M. Gunzburger, M. Hanke, R. J. Harrison, M. A. Heroux, J. Hesthaven, P. K. Jimack, C. Johnson, K. E. Jordan, D. E. Keyes, R. H. Krause, V. Kumar, S. Mayer, J. Meza, K. M. Morken, J. T. Oden, L. R. Petzold, P. Raghavan, S. M. Shontz, A. E. Trefethen, P. R. Turner, V. V. Voevodin, B. I. Wohlmuth, and C. S. Woodward. Research and education in computational science

and engineering: Report from a workshop sponsored by the Society for Industrial and Applied Mathematics (SIAM) and the European Exascale Software Initiative (EESI-2), August 4-6, 2014, Breckenridge, Colorado. *To appear, SIAM Review*, 2018.

[125] Y. Saad and M. H. Schultz. GMRES: A generalized minimal residual method for solving nonsymmetric linear systems. *SIAM Journal on Scientific Computing*, 3(7): 856–869, 1986.

[126] A. K. Saibaba and P. K. Kitanidis. Efficient methods for large-scale linear inversion using a geostatistical approach. *Water Resources Research*, 48(5):W05522, 2012.

[127] A. K. Saibaba and P. K. Kitanidis. Fast computation of uncertainty quantification measures in the geostatistical approach to solve inverse problems. *Advances in Water Resources*, 82:124–138, 2015.

[128] A. K. Saibaba, J. Lee, and P. K. Kitanidis. Randomized algorithms for generalized Hermitian eigenvalue problems with application to computing Karhunen-Loève expansion. *Numerical Linear Algebra with Applications*, 23(2):314–339, 2016. nla.2026.

[129] T. Sarlos. Improved approximation algorithms for large matrices via random projections. *2006 47th Annual IEEE Symposium on Foundations of Computer Science (FOCS'06)*, pages 143–152, 2006.

[130] A. Schoniger, W. Nowak, and H.-J. Hendricks Franssen. Parameter estimation by ensemble kalman filters with transformed data: Approach and application to hydraulic tomography. *Water Resources Research*, 48(4):W04502, 2012.

[131] N. N. Schraudolph and T. Graepel. Combining conjugate direction methods with stochastic approximation of gradients. In C. Bishop and B. Frey, editors, *Proceedings of the Ninth International Workshop on Artificial Intelligence and Statistics*, page 6, 2003.

[132] A. Shapiro, D. Dentcheva, and A. Ruszczynski. *Lectures on Stochastic Programming: Modeling and Theory*. Society for Industrial and Applied Mathematics, 2009.

[133] J. Sheng. *Enhanced oil recovery field case studies*. Gulf Professional Publishing, 2013.

[134] D. W. Stroock. *Probability Theory: An Analytic View*. Cambridge University Press, second edition, 2011.

[135] A. M. Stuart. Inverse problems: A Bayesian perspective. *Acta Numerica*, 19:451–559, 2010.

[136] N. Sun. *Inverse Problems in Groundwater Modeling*. Kluwer Academic Publishers, 1994.

[137] A. Tarantola. *Inverse Problem Theory and Methods for Model Parameter Estimation*. Society for Industrial and Applied Mathematics, Philadelphia, PA, 2005.

[138] M. J. Tonkin and J. Doherty. A hybrid regularized inversion methodology for highly parameterized environmental models. *Water Resources Research*, 41:W10412, 2005.

[139] H. Touchette. The large deviation approach to statistical mechanics. *Physics Reports*, 478(1):1–69, 2009.

[140] J. A. Tropp. Improved analysis of the subsampled randomized hadamard transform. *Advances in Adaptive Data Analysis*, 03(01n02):115–126, 2011.

[141] J. A. Tropp, A. Yurtsever, M. Udell, and V. Cevher. Practical sketching algorithms for low-rank matrix approximation. *SIAM Journal on Matrix Analysis and Applications*, 38(4):1454–1485, 2017.

[142] K. van den Doel and U. M. Ascher. Adaptive and stochastic algorithms for electrical impedance tomography and DC resistivity problems with piecewise constant solutions

and many measurements. *SIAM Journal on Scientific Computing*, 34(1):A185–A205, 2012.

[143] T. van Leeuwen, A. Y. Aravkin, and F. J. Herrmann. Seismic waveform inversion by stochastic optimization. *International Journal of Geophysics*, 2011:18, 2011.

[144] V. Vesselinov, S. Neuman, and W. Illman. Three-dimensional numerical inversion of pneumatic cross-hole tests in unsaturated fractured tuff: 2. Equivalent parameters, high-resolution stochastic imaging and scale effects. *Water Resources Research*, 37 (12), 2001.

[145] V. Vesselinov, S. Neuman, and W. Illman. Three-dimensional numerical inversion of pneumatic cross-hole tests in unsaturated fractured tuff: 1. Methodology and borehole effects. *Water Resources Research*, 37(12), 2001.

[146] V. Vesselinov, D. O'Malley, Y. Lin, et al. MADS.jl: (Model Analyses and Decision Support) in Julia, 2018.

[147] J. Virieux and S. Operto. An overview of full-waveform inversion in exploration geophysics. *Geophysics*, 74(6):WCC1–WCC26, 2009.

[148] K. Wang, T. Bui-Thanh, and O. Ghattas. A randomized maximum a posteriori method for posterior sampling of high dimensional nonlinear Bayesian inverse problems. *SIAM Journal on Scientific Computing*, 40(1):A142–A171, 2018.

[149] M. F. Wheeler and M. Peszyńska. Computational engineering and science methodologies for modeling and simulation of subsurface applications. *Advances in Water Resources*, 25(8):1147–1173, 2002.

[150] H. Xiang and J. Zou. Regularization with randomized SVD for large-scale discrete inverse problems. *Inverse Problems*, 29(8):085008, 2013.

[151] H. Xiang and J. Zou. Randomized algorithms for large-scale inverse problems with general Tikhonov regularizations. *Inverse Problems*, 31(8):085008, 2015.

[152] T. Yeh and J. Simunek. Stochastic fusion of information for characterizing and monitoring the vadose zone. *Vadose Zone Journal*, 1(2):207–221, 2002.

[153] D. Yin and W. A. Illman. Hydraulic tomography using temporal moments of drawdown recovery data: A laboratory sandbox study. *Water Resources Research*, 45(1):W01502, 2009.

[154] J. Young and D. Ridzal. An application of random projection to parameter estimation in partial differential equations. *SIAM Journal on Scientific Computing*, 34(4):A2344–A2365, 2012.

[155] J. Zhang and T.-C. J. Yeh. An iterative geostatistical inverse method for steady flow in the vadose zone. *Water Resources Research*, 33(1):63–71, 1997.

[156] J. Zhu and J. Yeh. Analysis of hydraulic tomography using temporal moments of drawdown recovery data. *Water Resources Research*, 42(2):W02403, 2006.

Vita

Ellen Le graduated from Bedford High School, in Bedford, Massachusetts in 2006. In 2010 she received a State Department David L. Boren scholarship for six months of Vietnamese language study in Ho Chi Minh City, Vietnam. She graduated from Pomona College in Claremont, California in December 2010. She attended the University of Iowa in Iowa City, Iowa as a GAANN Fellow and graduated with a Master of Science in Mathematics in May 2013. In August 2013, she began the Computational Sciences, Engineering, and Mathematics Ph.D. program at the Institute for Computational Engineering and Sciences, at the University of Texas at Austin, as a CSEM Fellow.

Permanent email: eble@utexas.edu